MICROGRAVITY AND HYPOGRAVITY COMPATIBLE METHODS FOR THE DESTRUCTION OF SOLID WASTES BY MAGNETICALLY ASSISTED GASIFICATION

James E. Atwater, James R. Akse, and Richard R. Wheeler, Jr.
UMPQUA Research Company

Goran N. Jovanovic, Joaquin Pinto-Espinoza, Brian Reed, and Thana Sornchamni
Chemical Engineering Department, Oregon State University

FINAL REPORT

GRANT NAG 9 - 1181

August 2003

UMPQUA Research Company
P.O. Box 609 - 125 Volunteer Way
Myrtle Creek, Oregon 97457
(541) 863-7770 Facsimile: (541) 863-7775
Email: jatwater@urcmail.net http://urc.cc/mag

URC 81036

TABLE OF CONTENTS

TABLE OF CONTENTS i

EXECUTIVE SUMMARY ii

1. INTRODUCTION 1

2. MAGNETIC MATERIALS DEVELOPMENT 4

2.1 Porous Cobalt 6

2.2 Ferrite Impregnated Calcium Alginate 19

3. MAGNET DESIGN 28

4. MATHEMATICAL MODELING AND NUMERICAL SIMULATION 43

4.1 Voidage Distribution Model 43

4.2 Computational Fluid Dynamics 47

4.3 Magnetically Assisted Filtration Model 53

5. MAGNETICALLY ASSISTED FILTRATION 56

6. MAGNETICALLY ASSISTED FLUIDIZATION 62

6.1 Laboratory GMAFB Fluidization Experiments 66

6.2 Microgravity GMAFB Fluidization Experiments 69

7. SOLID WASTE GASIFICATION 79

8. HARDWARE DESIGN, ASSEMBLY, AND COMMISSIONING 88

8.1 Magnetically Assisted Gasification Hardware Design and Assembly 88

8.2 Magnetically Assisted Gasification Hardware Operations 117

8.3 Magnetically Assisted Gasification Hardware Commissioning Tests 120

9. CONCLUSIONS 128

10. REFERENCES 130

EXECUTIVE SUMMARY

This report summarizes a three-year collaborative effort between researchers at UMPQUA Research Company (URC) and the Chemical Engineering Department at Oregon State University (OSU). The Magnetically Assisted Gasification (MAG) concept was originally conceived as a microgravity and hypogravity compatible means for the decomposition of solid waste materials generated aboard spacecraft, lunar and planetary habitations, and for the recovery of potentially valuable resources. While a number of methods such as supercritical water oxidation (SCWO)[1-7], fluidized bed incineration[8-12], pyrolysis[13-24], composting and related biological processes[25-33] have been demonstrated for the decomposition of solid wastes, none of these methods are particularly well-suited for employment under microgravity or hypogravity conditions.

For example, fluidized bed incineration relies upon a balance between drag forces which the flowing gas stream exerts upon the fluidization particles and the opposing force of gravity[34]. In the absence of gravity, conventional fluidization cannot take place. Hypogravity operation can also be problematic for conventional fluidized bed reactors, because the various factors which govern fluidization phenomena do not all scale linearly with gravity. For this reason it may be difficult to design and test fluidized bed reactors in 1g, which are intended to operate under different gravitational conditions. However, fluidization can be achieved in microgravity (and hypogravity) if a suitable replacement force to counteract the forces between fluid and particles can be found. Possible alternatives include: centripetal force, electric fields, or magnetic fields. Of these, magnetic forces created by the action of magnetic fields and magnetic field gradients upon ferromagnetic media offer the most practical approach.

The goal of this URC-OSU collaborative effort was to develop magnetic hardware and methods to control the degree of fluidization (or conversely consolidation) of granular ferromagnetic media and to employ these innovations in sequential filtration and fluidized bed processes for the segregation and decomposition of solid waste materials, and for the concentration and collection of inorganic residue (ash). This required the development of numerous enabling technologies and tools.

During the course of the three year effort, the Magnetically Assisted Gasification (MAG) project has investigated and developed novel high temperature capable magnetic materials, new and innovative means for the projection of magnetic fields to produce constant magnetic field gradients, original software to facilitate the design of electromagnets in both rectangular and cylindrical geometries, mathematical models to simulate Magnetically Assisted Fluidization and Magnetically Assisted Filtration processes in both normal gravity and microgravity, and culminated in the design, assembly, and initial testing of a Magnetically Assisted Gasification test-bed. The fundamental magnetic control techniques have also been demonstrated in microgravity flight experiments.

This work resulted in the publication of two scientific papers in the peer reviewed literature[35,36], with one additional manuscript currently under consideration for publication[37]. Two papers describing various aspects of the MAG project have also been published by SAE and presented at International Conferences on Environmental Systems[38,39]. Technical presentations have also been made at a variety of venues, including: Life Support and Biosphere Conference[40], Bioastronautics Investigators Workshop[41], International Conference on Circulating Fluidized Beds[42], World Space Congress[43], AIChE Annual Meeting[44,45], ALS TIM Telecon, and Annual ALS Principal Investigators Meetings. One Master of Science[46] and one Doctor of Philosophy[47] degree have been awarded, in part, for the work conducted under this project. It is anticipated that one additional doctorate will be awarded within three months following submission of this report.

1. INTRODUCTION

Development of efficient means for the decomposition of solid wastes and recovery of valuable resources is a critical requirement for future Advanced Life Support (ALS) systems which will be needed to sustain long duration manned missions in space. Of particular importance are technologies which may be employed in hypogravity and microgravity environments. This report describes the results of a three-year effort conducted jointly by investigators at UMPQUA Research Company (URC) and the Chemical Engineering department of Oregon State University (OSU) with primary emphasis on the development of microgravity and hypogravity compatible equipment and methods.

Conceptually, Magnetically Assisted Gasification (MAG) embodies a three step process consisting of: 1) separation and concentration of solid wastes from an aqueous slurry by filtration, 2) gasification of the organic content of the entrapped solid waste by a combination of pyrolysis, steam reforming, and oxidation reactions, and 3) removal and collection of the remaining inorganic ash (Figure 1.1). Depending upon mission specific requirements, any or all of these processes may be employed. High temperature capable ferromagnetic materials are used as both filtration media and heterogeneous catalyst. In each step, the degree of consolidation (or conversely, fluidization) of the granular ferromagnetic media is controlled using magnetic forces. Given suitable reaction conditions, solid wastes can be decomposed and valuable resources such as hydrogen, carbon dioxide, and water can be recovered.

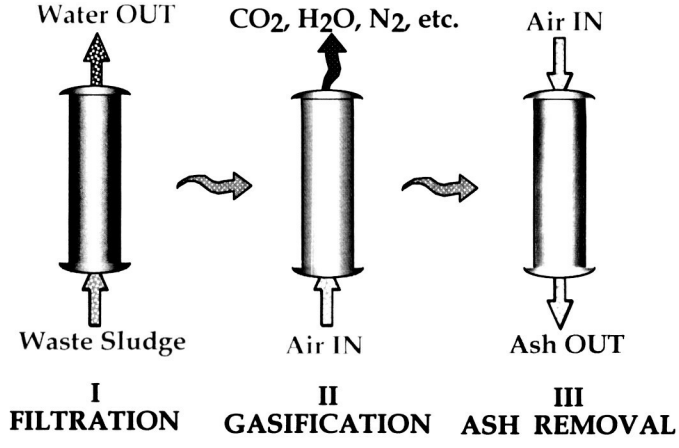

Figure 1.1 Three Step MAG Process.

Currently, the two most well studied physico-chemical solid waste processing concepts embody Supercritical Water Oxidation[1-7] (SCWO) and Fluidized Bed Incineration[8-12] (FBI) based methods. Both of these technologies are relatively mature, having been developed over a time span of more than a decade; but neither is particularly microgravity compatible, and both present challenges with respect to operation in hypogravity. Because all investigations of these two solid waste destruction methodologies to date have been conducted under 1*g*, it is easy to underestimate the potential difficulty of operation which may arise in hypogravity. An FBI system designed for operation in 1*g* will behave very differently under either Martian or Lunar gravity. For example, an air fluidized bed containing sand particles with 0.2 mm average diameter will require a minimum fluidization velocity[34] of ~ 0.14 m/s; while on the Martian surface the equivalent degree of fluidization will be achieved with a much reduced flow of ~ 0.085 m/s; or ~ 0.057 m/s for the minimum fluidization velocity on the Moon. One practical implication of this is that, for an equivalent degree of fluidization of an FBI system operating on Mars or the Moon, the mass transfer rate for the oxidant will be reduced by 39% or 59%, respectively. This will have profound effects on the efficiency of solid waste decomposition, the distribution and chemical nature of the reaction byproducts[48,49], and the rate of heat production by the exothermic reactions. To produce a solids processing rate equivalent to that achieved on Earth, the FBI designed for hypogravity must be substantially larger and heavier (i.e., the Equivalent System Mass (ESM) will be substantially increased). Also, testing of a hypogravity design on earth may be very difficult. However, our work has shown that not only can magnetic forces be used to achieve fluidization in microgravity (which otherwise would be impossible) but that potential hypogravity related problems may also be overcome through the use of properly constructed magnetic fields and magnetic field gradients acting upon suitable ferromagnetic media.

While the application of these methods to solid wastes processing was the primary focus of our attention, we believe that the magnetic materials, magnetic control methods, design and modeling software which has been developed under this project may potentially be employed across a broad spectrum of additional microgravity and hypogravity applications in support of ALS, *In Situ* Resource Utilization (ISRU), and materials science objectives. For example, using granular ferromagnetic materials as the fluidization media and Gradient Magnetically

Assisted Fluidized Bed (GMAFB) methods developed by our team, an FBI system could be constructed to achieve earth-equivalent processing rates on either Mars, the Moon, or in microgravity, using successively larger magnetic field strengths and magnetic field gradients to compensate for the progressively weaker gravitational forces.

Owing to the relative immaturity of the MAG technology, a substantial portion of the effort was directed toward the development of enabling technologies, materials, and tools, including: synthetic methods for the production of novel high temperature capable magnetic materials, new and innovative means for the projection of magnetic fields to produce constant magnetic field gradients, computer programs to facilitate the design of electromagnets in both rectangular and cylindrical geometries, magnetic fluidization and consolidation methodologies, and mathematical models to simulate Magnetically Assisted Fluidization and Magnetically Assisted Filtration processes in both normal gravity and microgravity. These fundamental magnetic control techniques have also been validated in microgravity flight experiments. During the third year, a Magnetically Assisted Gasification testbed was designed, assembled, and subjected to initial testing.

2. MAGNETIC MATERIALS DEVELOPMENT.

Materials which interact strongly with externally applied magnetic fields (**H**) are either ferromagnetic, antiferromagnetic, or ferrimagnetic. Ferromagnetic materials are composed of domains of aligned spins which strongly interact with an external field to produce a magnetization (**M**) which is proportional to field strength,

$$\mathbf{M} = \chi_m \mathbf{H}$$

where χ_m is the magnetic susceptibility of the medium. This produces a flux density (**B**) within the material (also termed magnetic induction) which is proportional to field strength, magnetization, and the magnetic permeability (μ) of the material,

$$\mathbf{B} = \mu_o(\mathbf{H} + \mathbf{M}) = \mu_o(\mathbf{H} + \chi_m \mathbf{H}) = \mu \mathbf{H}$$

$$\mu = \mu_o(1 + \chi_m)$$

where μ_o is the magnetic permeability of free space. Examples of ferromagnetic substances include: iron, cobalt, and nickel. In ferromagnetic materials, electron spins align with the applied field to yield magnetization, whereas,spins align antiparallel in antiferromagnetic substances. In ferrimagnetic materials, due to magnetocrystalline anisotropy, both parallel and antiparallel alignments occur. However, ferrimagnetic materials yield a net magnetization. Ferrimagnetics are represented by a wide variety of ceramics with a spinel crystal structure of the general form XM_2O_4, where X and M represent transition metals. These materials are termed ferrites. The prototypical ferrite is magnetite, Fe_3O_4. Maghemite (γ-Fe_2O_3) another iron oxide is also ferrimagnetic. Due to their low costs, ferrites are commonly used in magnetic recording media, and as permanent magnets in speakers, etc.

Magnetic materials are characterized as *'soft'* if they are easily magnetized and demagnetized, and as *'hard'* if they require high magnetic fields to demagnetize or to reverse the polarity of magnetization. Therefore, permanent magnets utilize *'hard'* materials. Among ferromagnetic materials, the pure metals

such as Fe, Co, and Ni, are all soft. The construction of permanent magnets from these materials requires the use of alloys, such as Al-Ni-Co. Samarium-cobalt ($SmCo_5$), and iron-neodymium-boron ($Nd_2Fe_{14}B$) solid solutions form particularly strong permanent magnets. Among the ferrimagnetic substances, typical hard ceramic magnets are made using barium hexaferrite ($BaFe_{12}O_{19}$) or less commonly strontium hexaferrite ($SrFe_{12}O_{19}$). Where soft ferrites are needed, zinc-manganese ($xZnFe_2O_4$-$yMnFe_2O_4$) and zinc-nickel ferrites ($xZnFe_2O_4$-$yNiFe_2O_4$) are most commonly employed.

Two very important physical properties of magnetic materials are the magnetization - demagnetization characteristics (hysteresis), and Curie temperatures. The Curie temperature (T_c) represents the point at which thermal energy is sufficient to overcome the applied magnetic field and randomize the ferromagnetic domains. When the Curie temperature is reached, the material becomes paramagnetic (demagnetized). Because typical solid waste gasification reactions (pyrolysis, combustion, steam reforming, etc.) occur at relatively high temperatures, the Curie temperature of the magnetic media used in Magnetically Assisted Gasification (MAG) must also be relatively high. T_c values for several high permeability - low coercivity (easily magnetized - demagnetized) ferromagnetic metals and ferrimagnetic ceramics are shown in Tables 2.1 and 2.2, respectively. Cobalt, with a Curie temperature of 1121°C, is clearly superior from the standpoint of high temperature operation.

Table 2.1 Curie Temperatures of Metals.

Metal	T_c (°C)
Iron	770
Cobalt	1121
Nickel	358

Table 2.2 Ferrite Curie Temperatures.

Ferrite	T_c (°C)
Li-ferrite	632
Li/Fe-ferrite	590-670
Ni-ferrite	575-597
Magnetite	563-590
Co-ferrite	495-520
Cu-ferrite	410-490
Mn-ferrite	295-303
Zn/Ni-ferrite	100-500
Zn/Mn-ferrite	100-250

Three magnetic properties are required for the media to be used for the Magnetically Assisted Filtration and Gasification solid waste treatment process: 1) high magnetic susceptibility - the material must be easily magnetized, 2) high Curie temperature - the material must not lose magnetization at reactor temperature, and, 3) low coercivity - the material must be easily demagnetized. The particle size distribution of the magnetic media is also very important, particularly with respect to the filtration step for confinement of the solid waste

within the bed, prior to thermal decomposition. Maximal filtration efficiency can be gained by utilization of a suitable distribution of particle sizes, in conjunction with the development of magnetic methods to stratify the bed so that a particle size gradient is obtained, with the largest particles at the inlet and the smallest particles near the outlet of the bed. Based upon the above, and also upon excellent catalytic properties, metallic cobalt was selected as the preferred high temperature ferromagnetic media. However, suitable forms of metallic cobalt were not commercially available and therefore a substantial materials development effort was required. Low temperature ferromagnetic media composed of ferrite impregnated calcium alginate beads were also prepared for employment in filtration and fluidization experiments which were performed at ambient temperature. Preparation procedures and characterizations of the material properties of these media are summarized below.

2.1 Porous Cobalt Media. Spherical porous metallic cobalt beads were prepared utilizing a four step process consisting of: [1] production of cobalt oxide loaded polymeric spheres by alginate gelation, [2] oxidative and pyrolytic decomposition of the organic polymer, yielding cobalt oxide spheres, [3] reduction of cobalt to the zero valent state, and [4] sintering of the metallic cobalt. Sodium alginate and a well-dispersed cobalt oxide powder are mixed together to form a slurry in which the cobalt oxide particles do not significantly settle during the gelation step. Droplets of this slurry are then contacted with a cobalt chloride solution causing divalent cobalt ions to cross-link with monovalent carboxylate functionalities between different alginate strands, using the apparatus illustrated in Figure 2.1. This causes gelation of the droplet into a spherical polymerized bead. The gelled beads are removed and then aged in a $CoCl_2$ solution for 12 hours. After this, the fully gelled beads are thoroughly rinsed with deionized water and dried.

The cobalt oxide impregnated alginate beads are converted to metallic cobalt in a series of thermal processes. The alginate binder is first removed in ambient air at 550°C for 4 hours in a tube furnace. The temperature is raised at 2°C/min. The binder-free cobalt oxide beads are then reduced to cobalt metal using a 5 % mixture of H_2 in N_2 at 550°C. The time required for completion of the reduction step is strongly dependent on the gas flow rate. The cobalt beads are then densified in a sintering step at 900°C. Most typically, sintering is accomplished in 240 minutes at a lower reducing gas flow rate to minimize

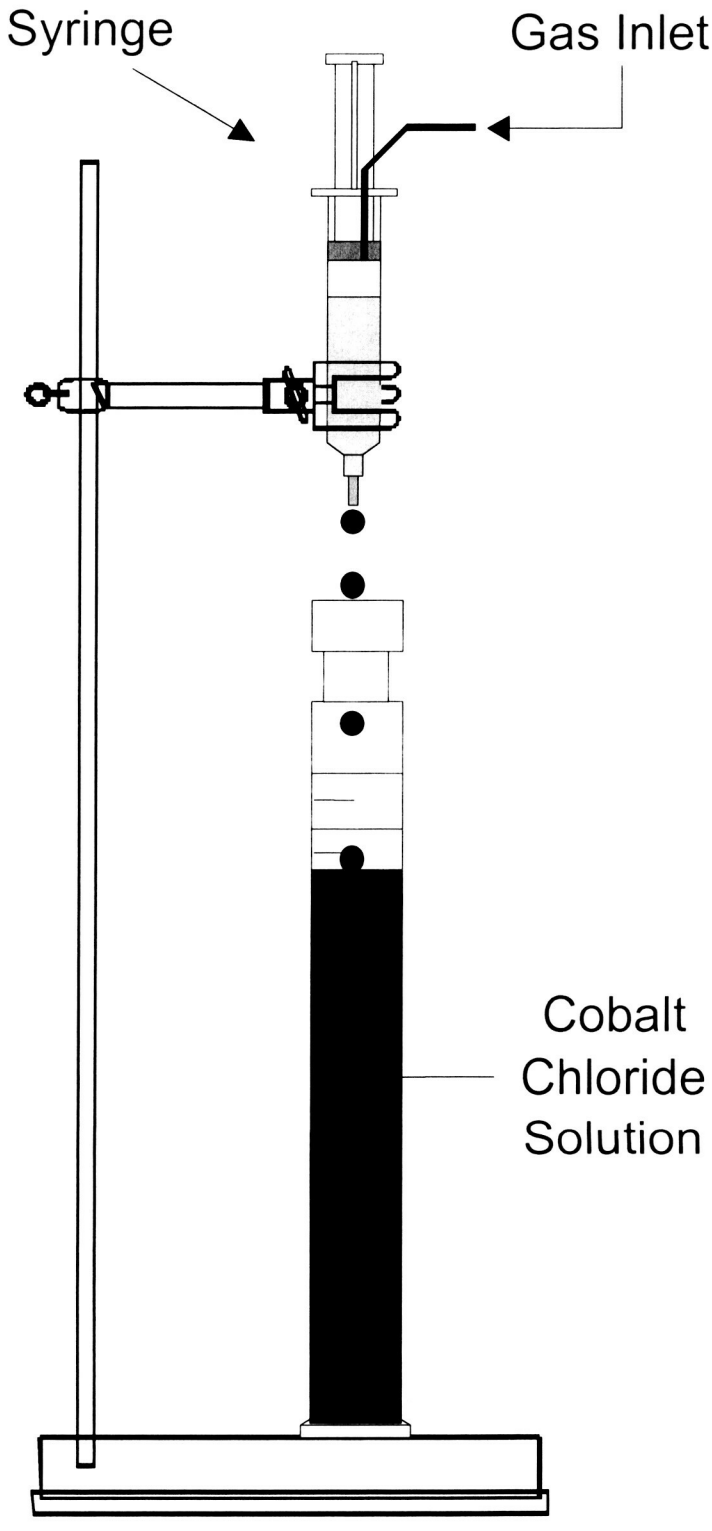

Figure 2.1. Cobalt Alginate Extrusion - Gelation Method.

temperature gradients within the tube furnace. The combined process produces highly porous and mechanically strong cobalt media.

Numerous technical challenges were overcome in the development of this process. To produce more than a few grams of cobalt beads at a time, improvements in the control of the alginate slurry rheology, strength of the dried gelled beads, removal of the alginate binder during thermal processing, and thermal process scale-up were required. The alginate - cobalt oxide formula was varied until stable and physically strong beads of ~1 mm diameter resulted. The reduction of cobalt oxide to cobalt metal required significant modification of the reaction conditions from those of the initial small scale experiments. With larger batches (i.e., 50-100 g), the reduction of cobalt oxide was limited by the availability of hydrogen in the reducing gas, since the maximum safe hydrogen content of the nitrogen process gas is 5%. For large batches, hydrogen became rapidly depleted by reduction reactions during the ramp-up to sintering temperature, so that sintering temperatures were reached before complete reduction of the cobalt oxide was achieved. This situation resulted in inconsistent sintering and densification within each batch. At this point, an attempt to substitute cobalt metal for cobalt oxide was made since cobalt metal does not require a reduction step. This proved unsuccessful due to the reaction of cobalt with water to produce cobalt oxide and a mixture of hydrogen and oxygen. Consequently, the original cobalt oxide reduction process was altered by providing longer reaction times and higher hydrogen/nitrogen gas flows at 550°C to completely reduce cobalt oxide prior to the sintering step.

Following the complete reduction of cobalt oxide to cobalt metal, sintering runs to endpoint temperatures of 700°C, 800°C, 900°C, and 1000°C were carried out to determine the thermal requirements for densification. In each case, the beads were heated from 550°C to the final temperature under 5 % hydrogen in nitrogen at 10°C min^{-1}. The beads were held at the final temperature for 4 hours, and then cooled to ambient temperature at the maximum furnace cooling rate. Sample densities were determined utilizing a linear point count methodology. These were 49.6, 58.4, 68.8, and 87.0 % of theoretical for samples processed at 700°, 800°, 900°, and 1000°C, respectively. Scanning Electron Photomicrographs taken at 2500X magnification for the cobalt bead surfaces of samples fired at these temperatures are shown in Figures 2.2-2.5, respectively.

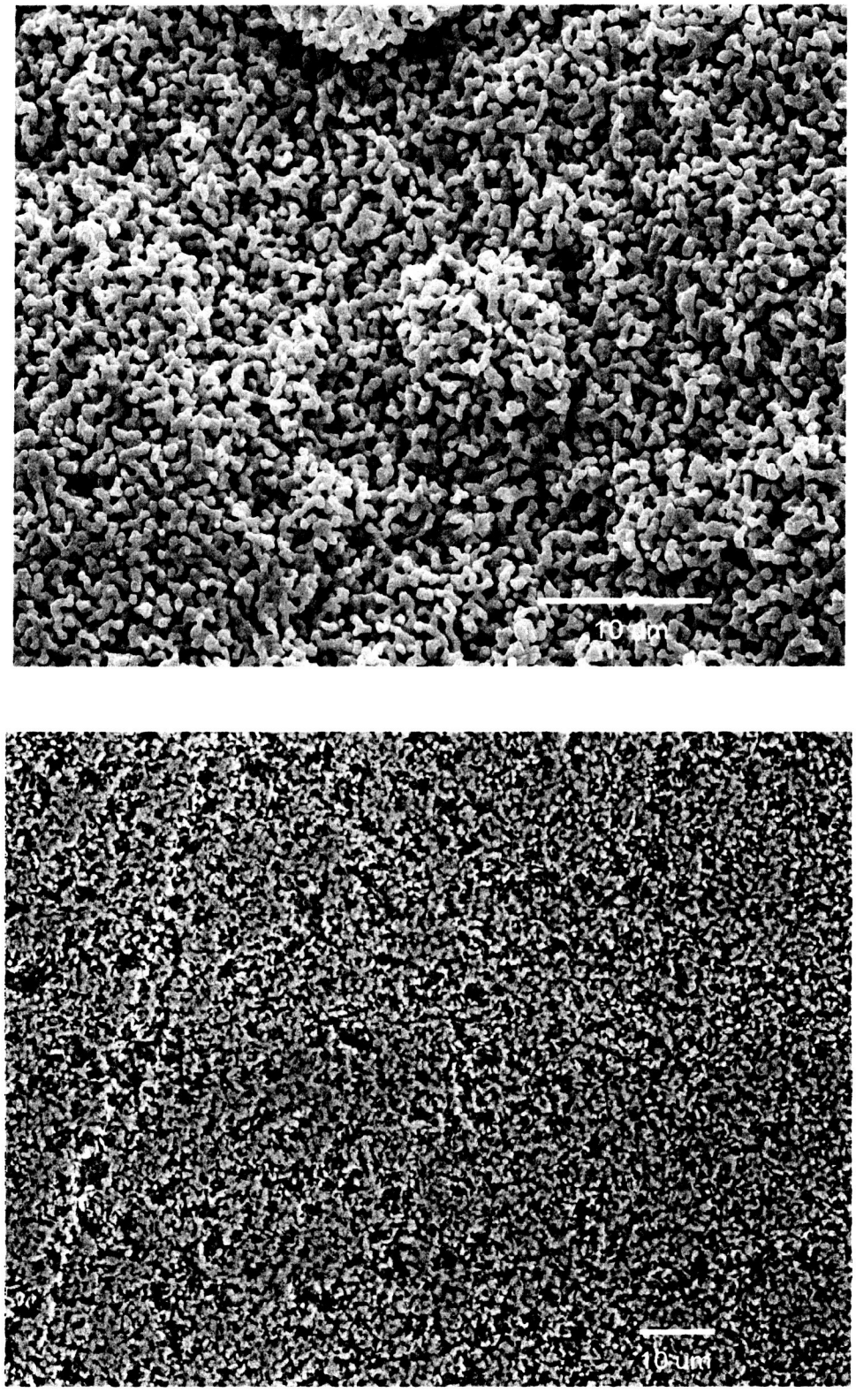

Figure 2.2. SEM Image of Porous Cobalt Bead Cross-Section (bottom) and Surface (top)-Sintered at 700°C.

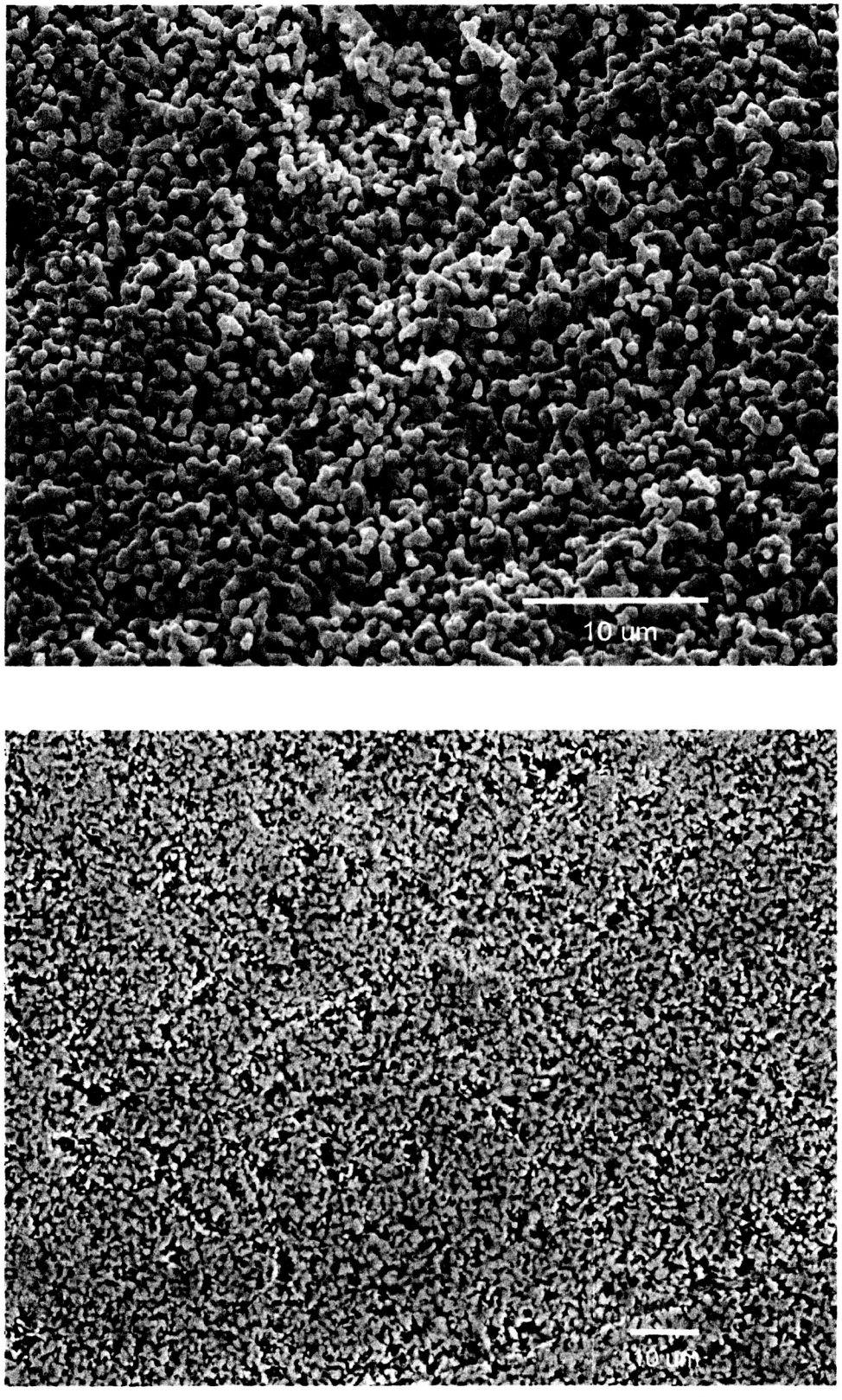

Figure 2.3. SEM Image of Porous Cobalt Bead Cross-Section (bottom) and Surface (top)-Sintered at 800°C.

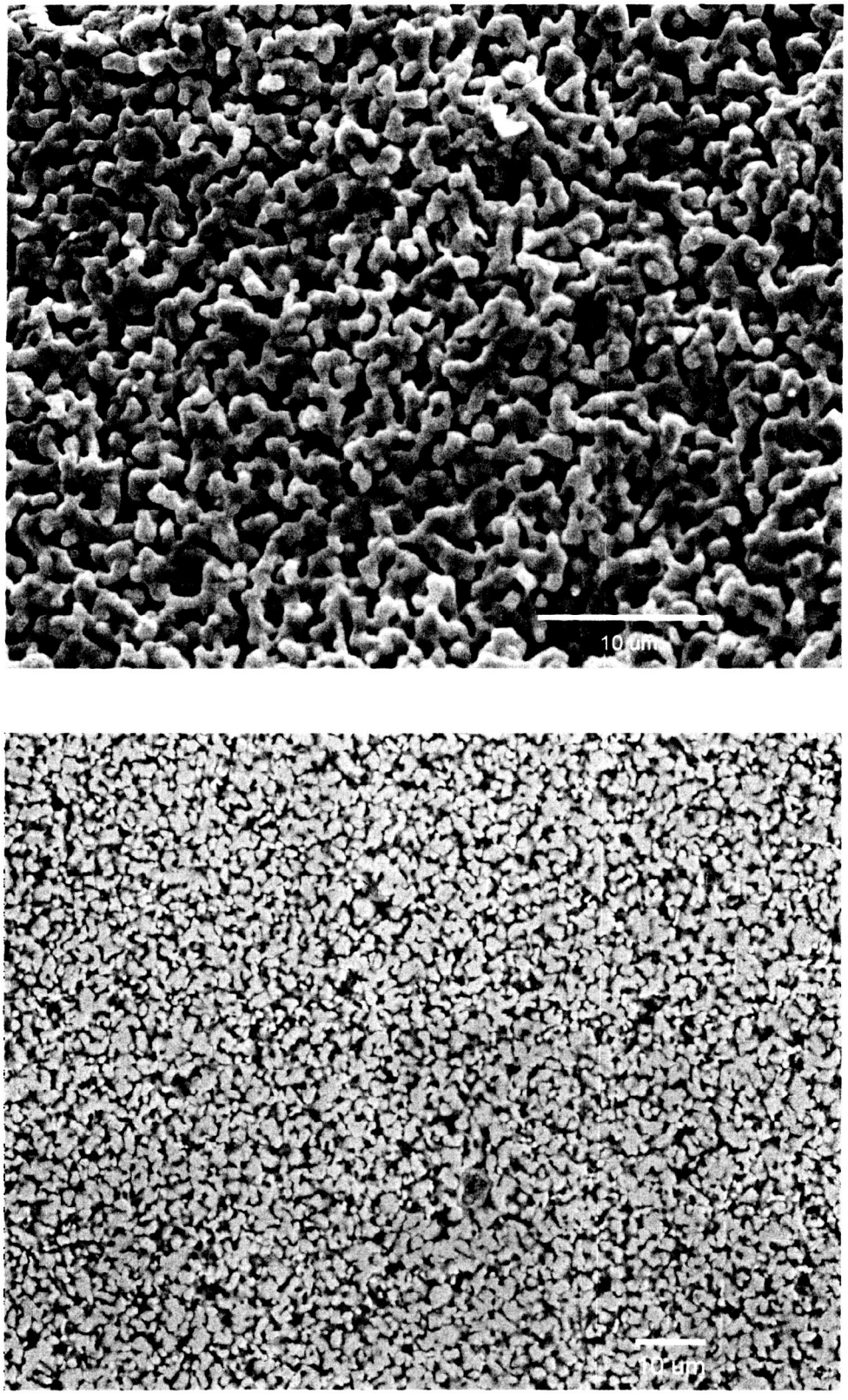

Figure 2.4. SEM Image of Porous Cobalt Bead Cross-Section (bottom) and Surface (top)-Sintered at 900°C.

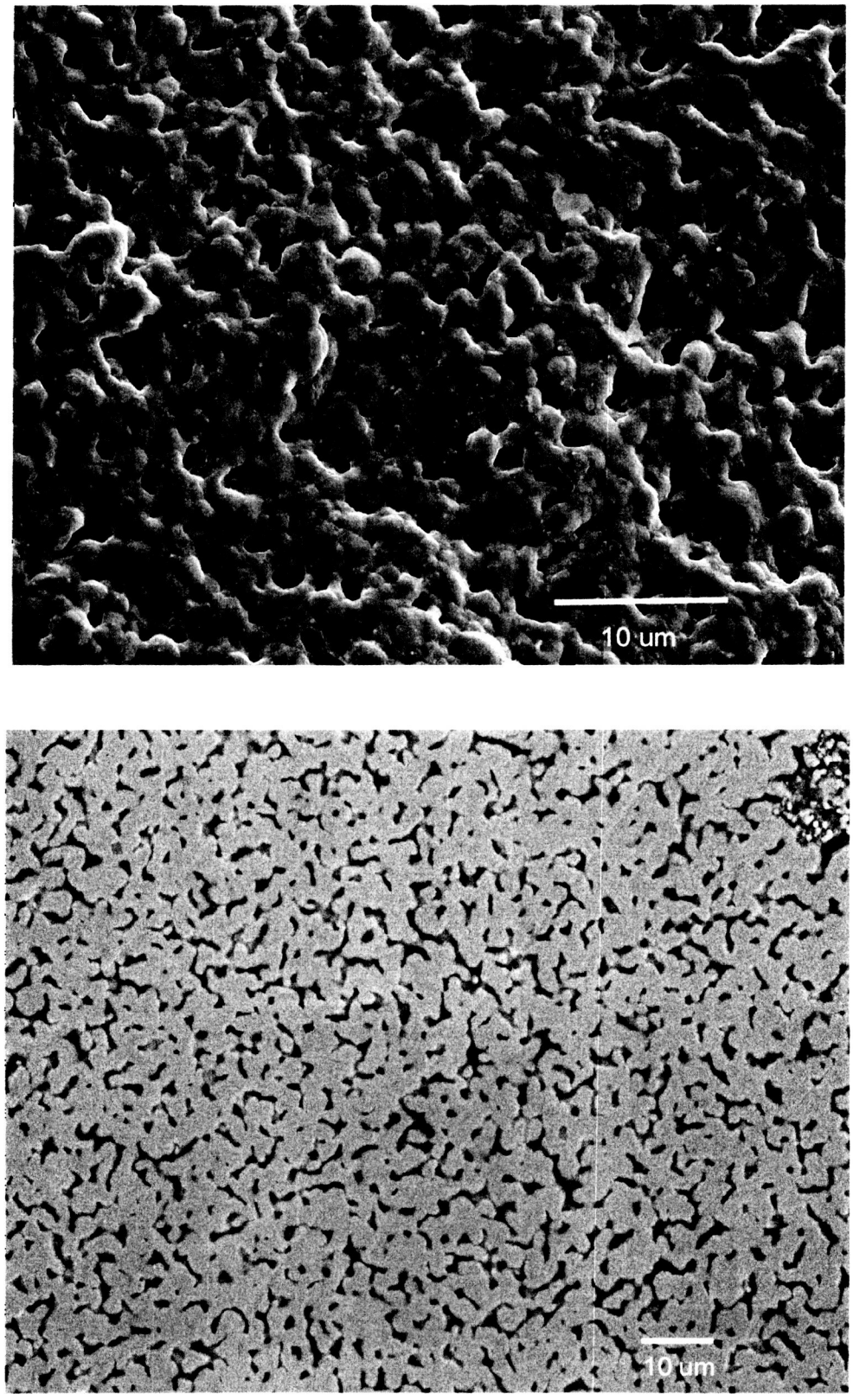

Figure 2.5. SEM Image of Porous Cobalt Bead Cross-Section (bottom) and Surface (top)-Sintered at 1000°C.

At the lowest temperature, the reduction of the sub-micron cobalt oxide powder resulted in a loosely connected metal compact with a grain size of ~ 0.5 μ m. The higher thermal treatment temperature of 800°C increased the grain size to ~ 1 μm. Both of these samples were mechanically weak, and therefore, unsuitable for use in a gasification reactor. At 900°C, the grain size increased to between 1.5 and 2 μm. Beads produced at this temperature were mechanically robust and relatively dense (6.12 g/cm^3). The grain size in the beads processed at 1000°C increased to between 2 and 3 μm.

The catalytic activity of MAG media may be an important factor in the promotion of solid waste gasification reactions. Hence, surface area, pore size distribution, and the interconnectivity of pores are important physical properties. The relationship between porosity (as determined by point count methods) of the cobalt beads and sintering temperature is illustrated in Figure 2.6. These values range from a high of ~50% at 700°C to a low of 11% at 1000°C. To further clarify the relationships between pore size distribution, surface area, and sintering temperature, nitrogen adsorption isotherms were acquired for cobalt beads sintered at 700°C and 900°C. These isotherms and the plots of cumulative surface area versus pore diameter are shown in Figures 2.7 through 2.10. Pore size distributions resulting from these two sintering temperatures are presented in Figures 2.11 and 2.12, respectively. BET surface areas of 1.24 and 0.64 m^2/g, and average pore diameters of 79.7 Å and 84.4 Å were determined for cobalt beads sintered at these two temperatures, respectively. The loss of approximately half of the surface area, while increasing the density from 49.6 to 68.8 % is a reasonable compromise, considering the increase in mechanical strength. The beads produced at 900°C were selected as the best candidate for application as high temperature fluidization media in the MAG process owing to the combination of physical robustness and reasonably high surface area.

Magnetization-demagnetization curves were also obtained for the porous cobalt spheres. These are shown in Figures 2.13 through 2.16, for temperatures of 700°C, 800°C, 900°C, and 1000°C, respectively. All cobalt beads showed strong magnetic susceptibility and very little hysteresis, indicating low remnant magnetization. The saturation volumetric magnetization generally increases with sintering temperature, correlating with increased densification. These results are in good agreement with the magnetic susceptibility of pure metallic cobalt.

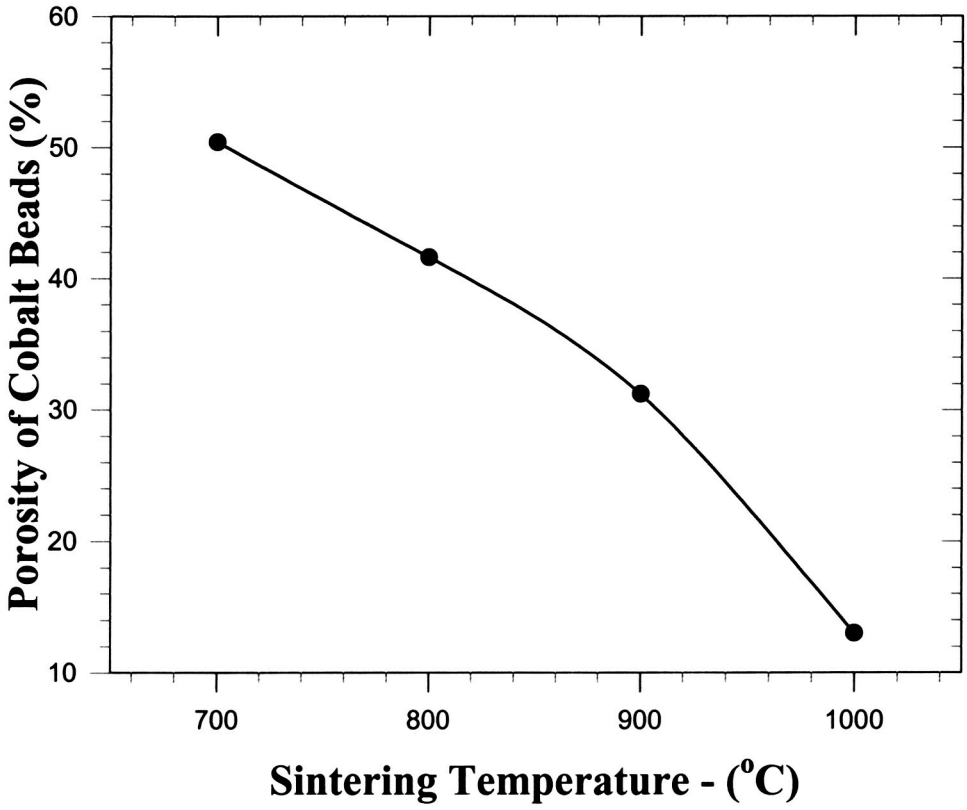

Figure 2.6. Porosity versus Sintering Temperature for Cobalt Beads.

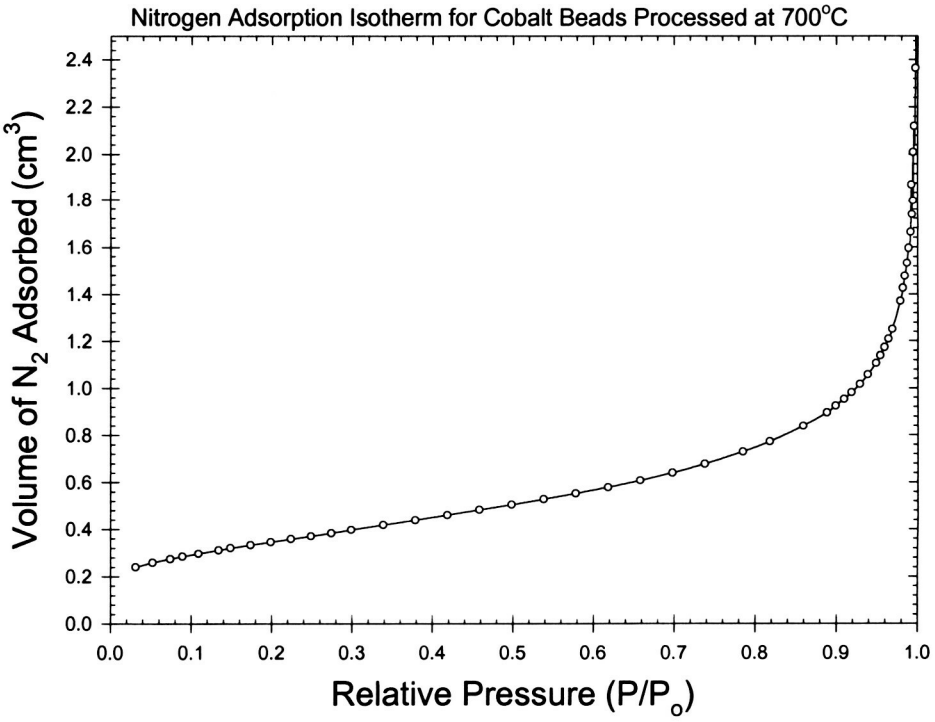

Figure 2.7. Nitrogen Adsorption Isotherm for Cobalt Beads Processed at 700°C.

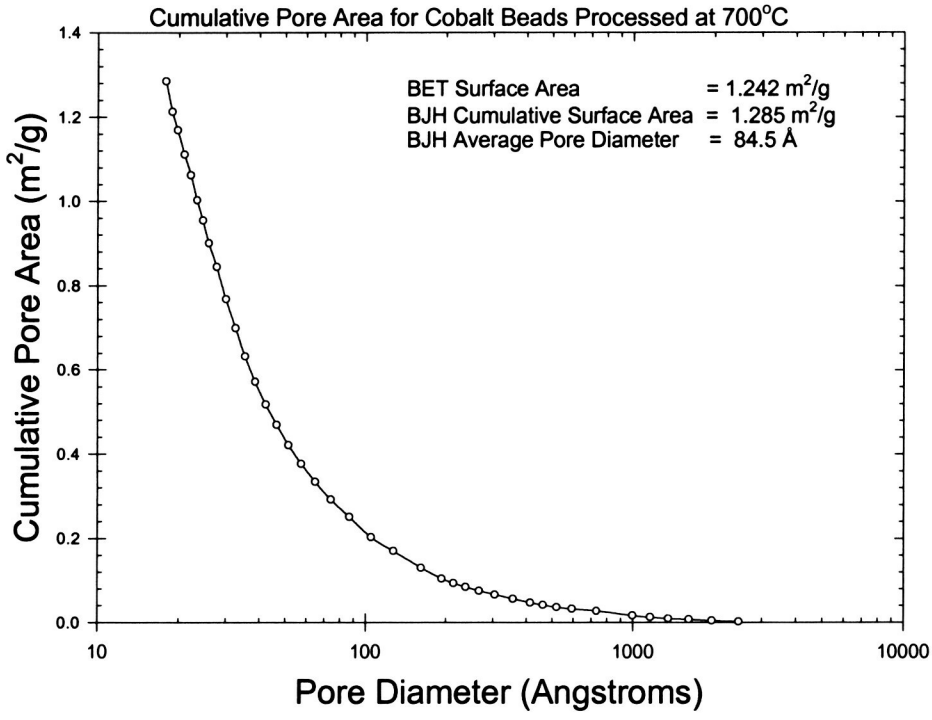

Figure 2.8. Cumulative Pore Surface Area for Cobalt Beads Processed at 700°C.

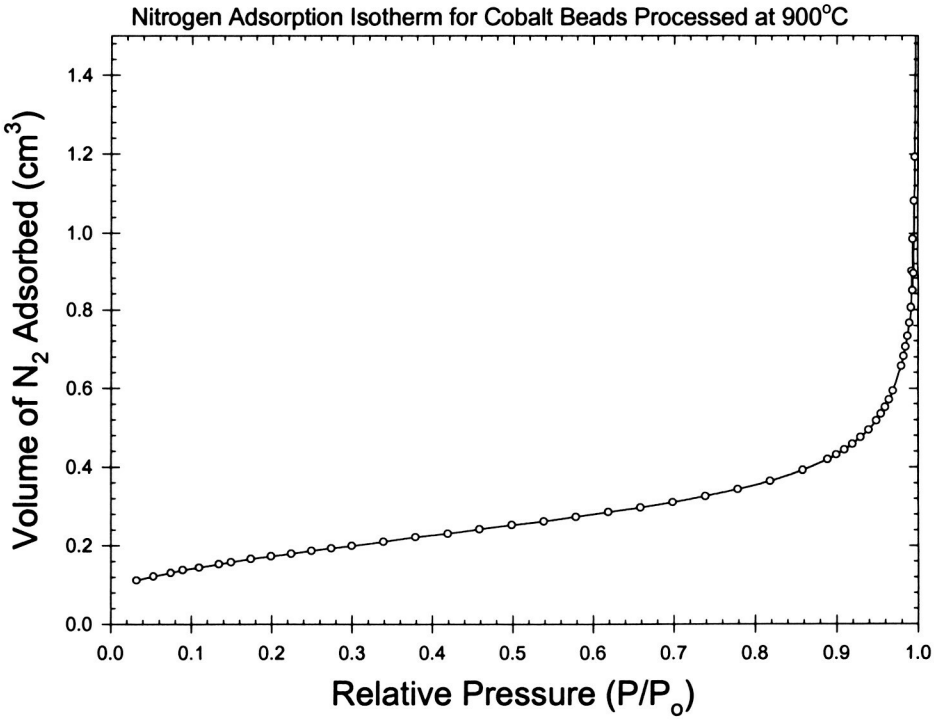

Figure 2.9. Nitrogen Adsorption Isotherm for Cobalt Beads Processed at 900°C.

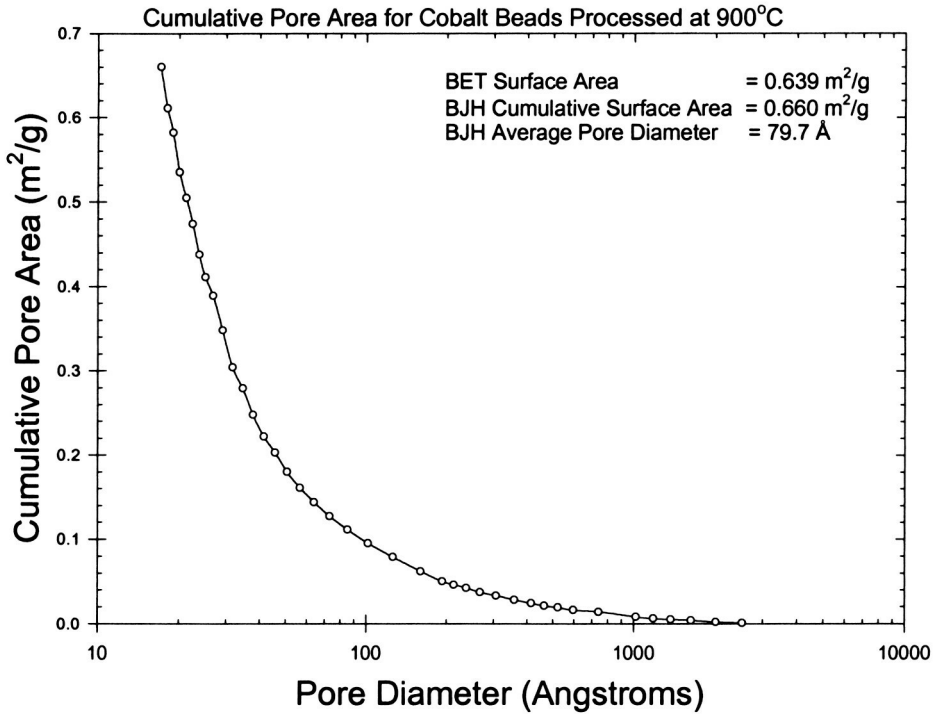

Figure 2.10. Cumulative Pore Surface Area for Cobalt Beads Processed at 900°C.

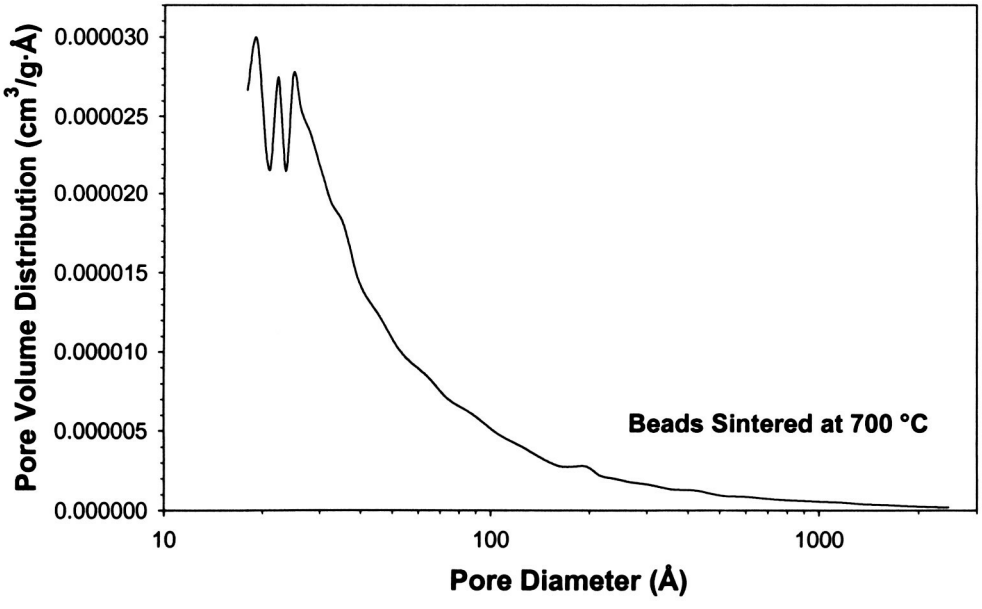

Figure 2.11. Pore Size Distribution for Cobalt Beads Sintered at 700°C.

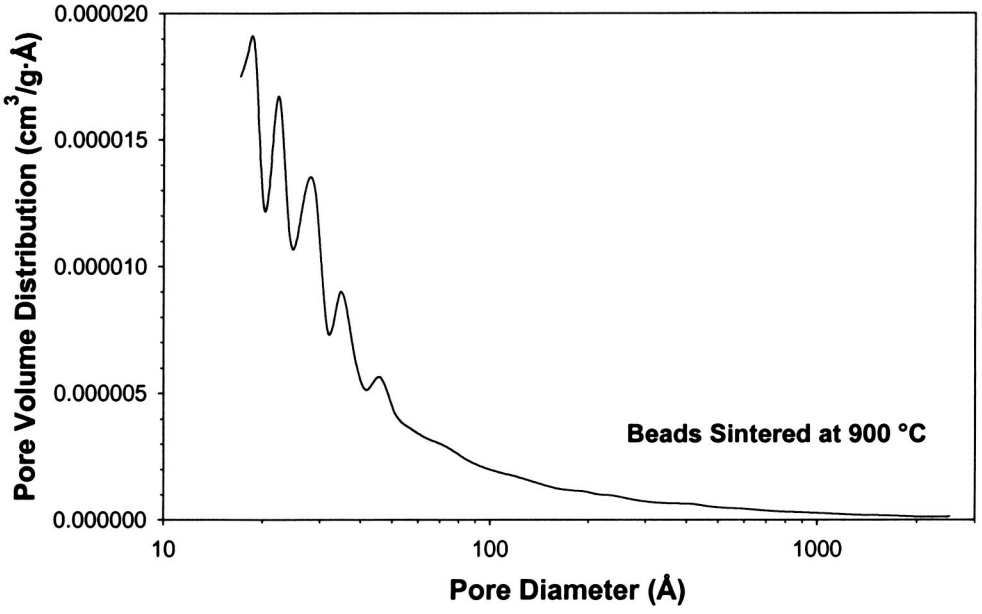

Figure 2.12. Pore Size Distribution for Cobalt Beads Sintered at 900°C.

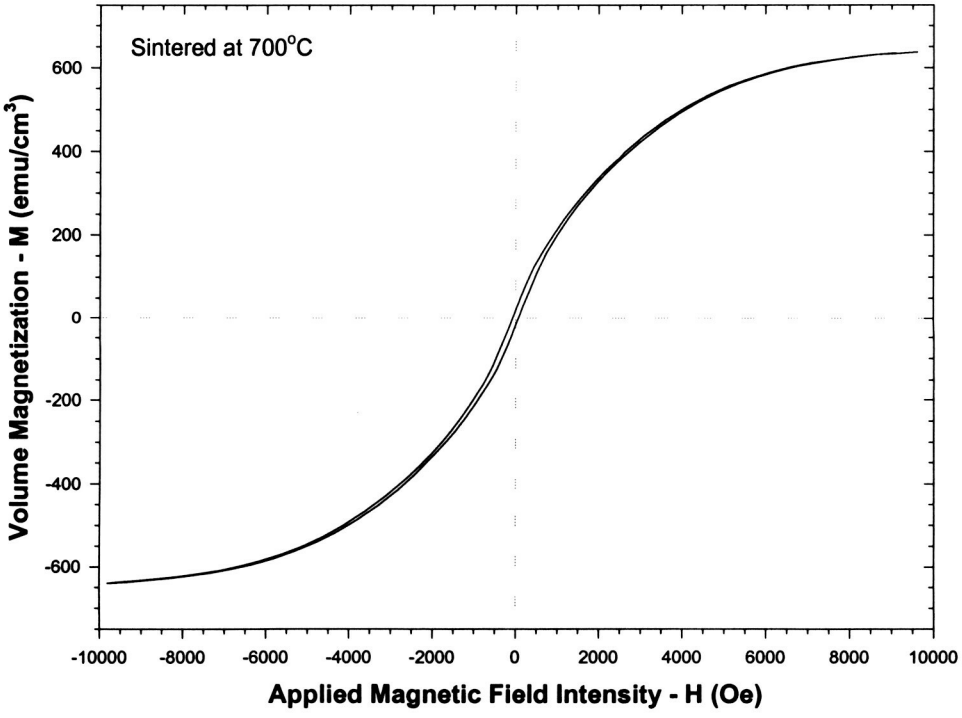

Figure 2.13. Magnetization-Demagnetization Curves for Cobalt Beads Sintered at 700°C.

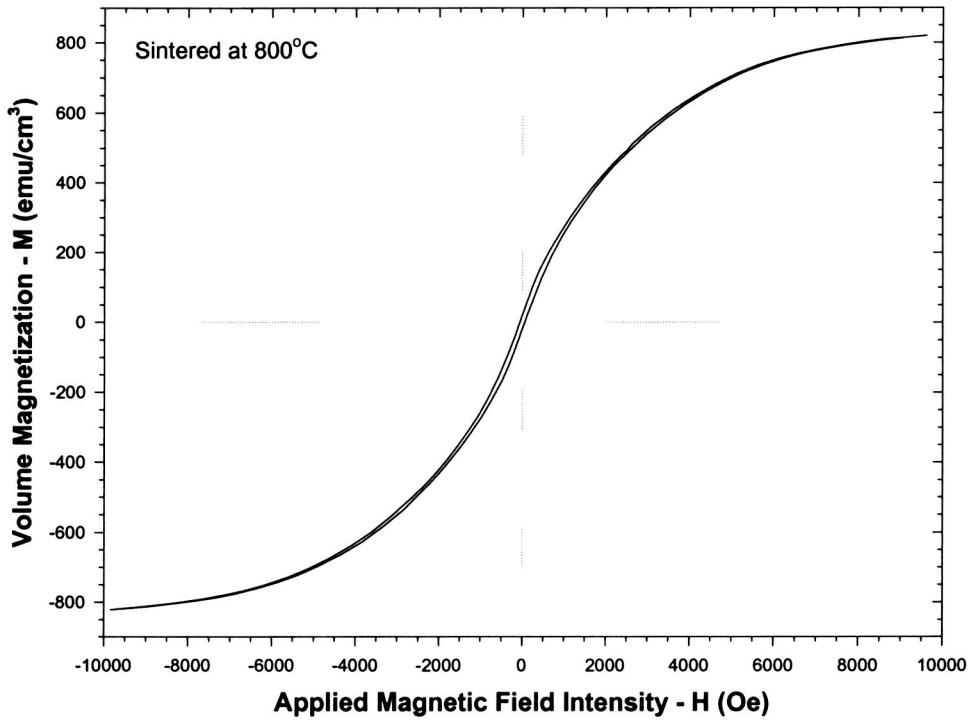

Figure 2.14. Magnetization-Demagnetization Curves for Cobalt Beads Sintered at 800°C.

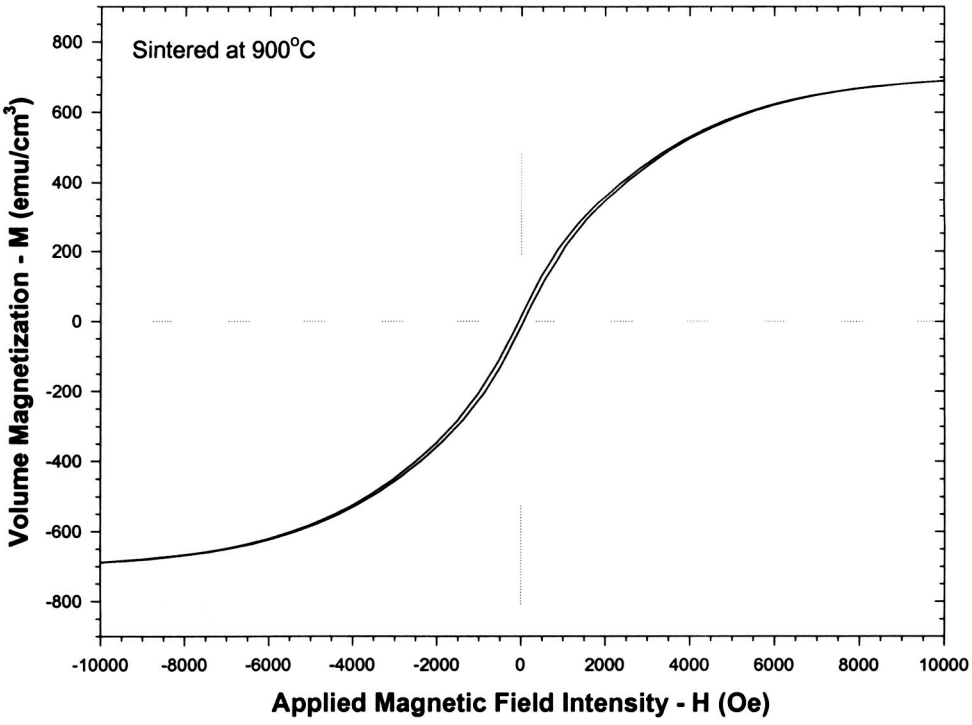

Figure 2.15. Magnetization-Demagnetization Curves for Cobalt Beads Sintered at 900°C.

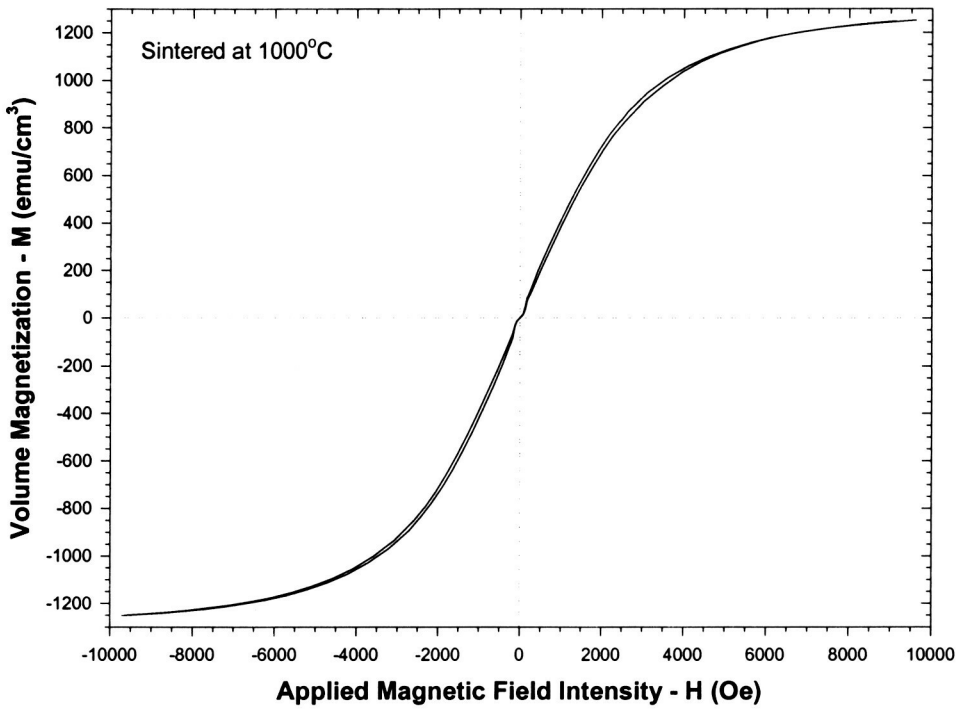

Figure 2.16. Magnetization-Demagnetization Curves for Cobalt Beads Sintered at 1000°C

2.2 Ferrite Impregnated Calcium Alginate Beads. Ferromagnetic media for use in ambient temperature experiments were prepared from a mixture of sodium alginate solution, ferrite powder, and hollow glass microspheres (sodium borosilicate). The composition of the resulting ferromagnetic particle is illustrated in Figure 2.17.

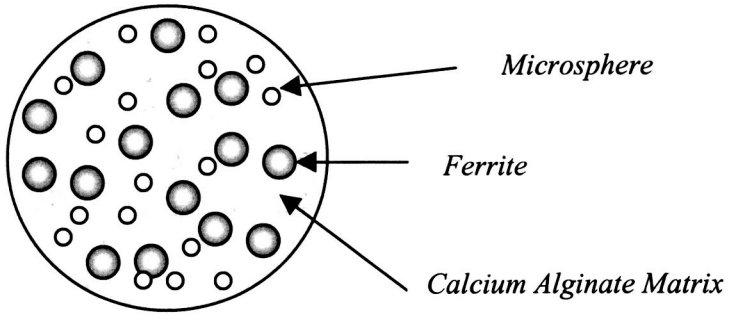

Figure 2.17. Ferrite Loaded Calcium Alginate Particle.

These particles are prepared in batches beginning with a well mixed suspension consisting of ~ 70 mL of 1.75 % aqueous sodium alginate solution to which 20 grams of ferrite powder and 8 grams of glass microspheres are added. After mixing for four hours, the suspension is transferred to the particle generator shown in the photograph presented in Figure 2.18 and illustrated schematically in Figure 2.19. The particle generator consists of a nozzle, which is connected to the bottom of a steel column. When the ferromagnetic alginate mixture is poured at top of the column, it slowly flows through the nozzle, forming drops which fall into a 1.0 M calcium chloride solution. The particle size can be controlled by regulating the air pressure at the top of the column, and by adjusting the airflow at the tip of the nozzle which shears off the drops. The divalent cation promotes polymerization by crosslinking of alginate monomers. Calcium chloride immediately reacts with sodium alginate, and forms calcium alginate on the surface of the droplets. Initially, only the surface of the sodium alginate droplet reacts with the calcium ion. For this reason, the newly formed beads are aged in the calcium chloride solution. Over a period of time, calcium ions diffuse toward the center of the particle, and form a complete calcium alginate structure throughout the droplet. The particles are then rinsed with deionized water and stored in a low concentration calcium chloride solution at room temperature. Properties of the resulting beads, the alginate and ferrite powders, and the hollow glass microspheres are summarized in Tables 2.3 – 2.6, respectively.

Table 2.3 Ferrite Particle Properties.

Particle	Ferrite
Particle Diameter (mm)	2.5
Density (kg / m^3)	1156
Ferrite	20%
Hollow Microsphere	8%
1.75% Alginate Solution	72%
Void Volume of Packed Bed	0.43
Magnetic Susceptibility, χ	0.425

Table 2.4 Physical and Chemical Properties of Hollow Glass Microspheres.

Chemical Compositions	SiO_2 70% Na_2O 25% B_2O_3 5%
Density (g/cm^3)	0.35
Median Particle Size (μm)	55

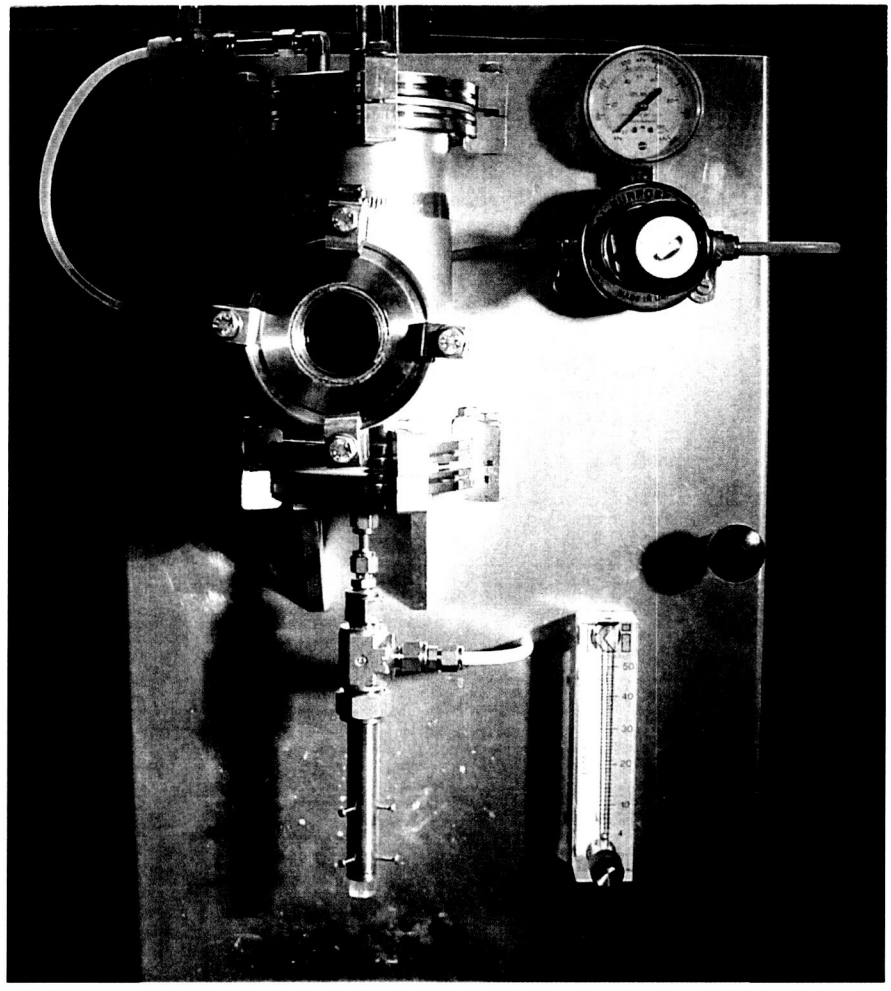

Figure 2.18. Ferrite Impregnated Calcium Alginate Bead Extruder.

Table 2.5 Properties of Sodium Alginate Powder.

Chemical Name	Algin (Sodium Alginate)
Chemical Family	Polysaccharide gum
Bulk Density	0.8 g/cm^3
pH 1% Solution	pH $\approx$ 7
Solubility in water	Soluble, forming a viscous solution, becoming a paste at a concentration of about 5%
Molecular Weight	Range from approx. 10,000 to 200,000 depending on viscosity

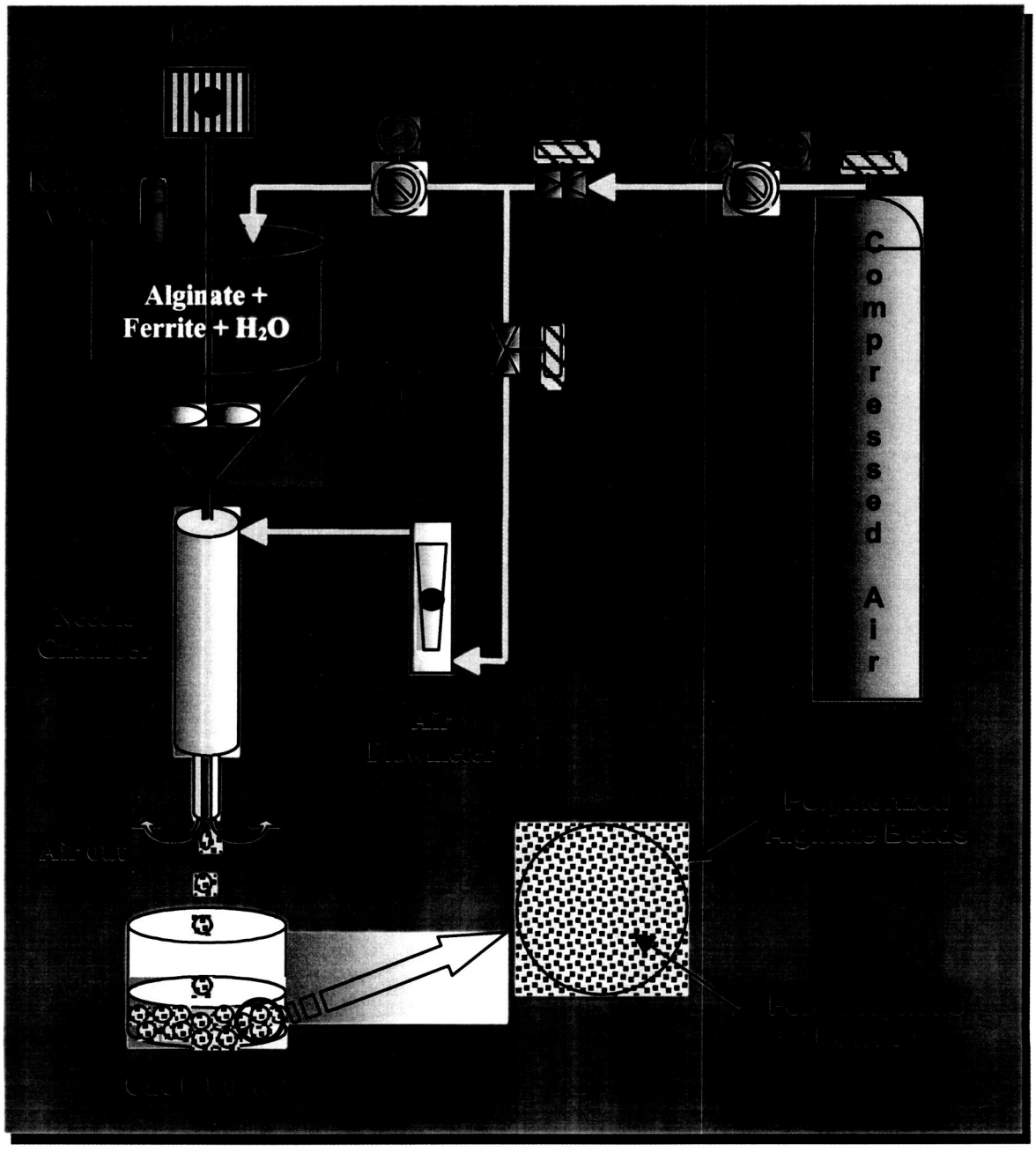

Figure 2.19. Ferrite Impregnated Alginate Bead Extrusion and Gelation Process.

Strong magnetic susceptibility (χ) is a critical requirement for both magnetically assisted fluidization and magnetically assisted filtration processes. Its numerical value can be used to evaluate both the external force imposed on a magnetic particle by the magnetic field as well as the forces acting between magnetized particles. The magnetic susceptibility of the ferrite loaded calcium alginate beads

Table 2.6 Composition and Properties of Ferrite Powder.

Chemical Composition	$MnOFe_2O_3$ 45-70% Fe_2O_3 22-55% $FeOFe_2O_3$ 0-0.5%
Density (g/cm^3)	2.2
Median Particle Size (μm)	2
Surface Area (cm^2/g)	2.286
Moisture %	0.01
Solubility in water	Negligible
Reactivity in water	Negligible
Melting Point	> 1500 C

was determined using a Thermogravimetric Analyzer (TGA) which was modified by the addition of an electromagnet positioned underneath the sample canister (Figure 2.20). The particle is pulled toward the coil as consequence of the magnetic force. This force is evaluated indirectly by measuring the apparent added weight of the particle. A schematic representation of the experimental apparatus is shown in Figure 2.21. The external magnetic field is generated by currents ranging between 5 to 40 amperes DC passing through the electromagnet coils. Basic properties of the electromagnet are presented in Table 2.7.

Table 2.7 Electromagnet used in Magnetic Susceptibility Measurements.

Electromagnet for TGA	**Characteristics**
Wire Type	AWG 10 HAPT
Wire Diameter	0.0027 m
Coil Inner Diameter	0.0266 m
Coil Thickness	0.0173 m
Layers	5
Turns	10 per layer

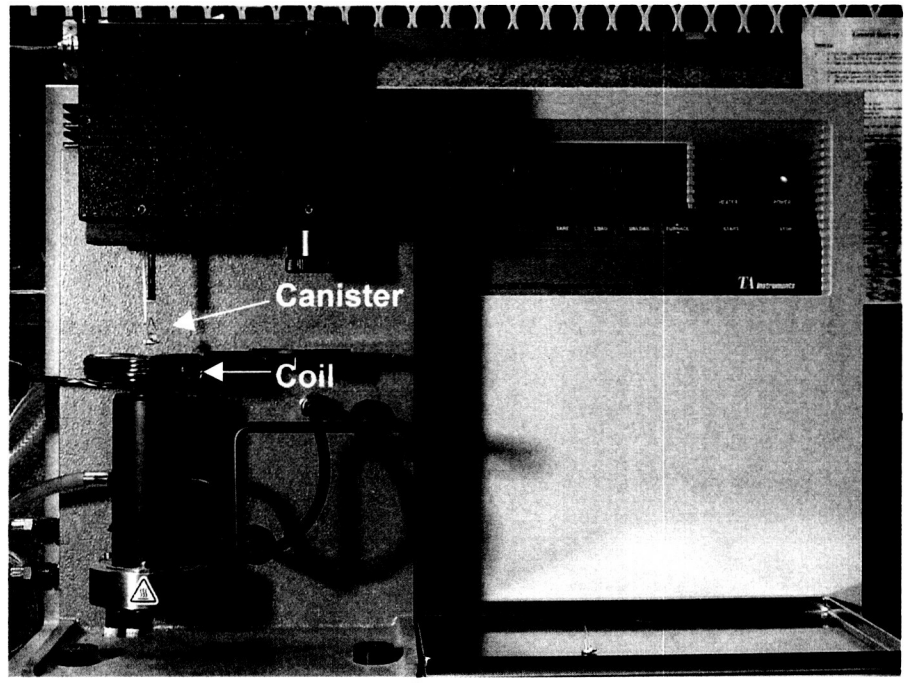

Figure 2.20 Thermogravimetric analyzer (TGA) showing the canister for the particle above the coil.

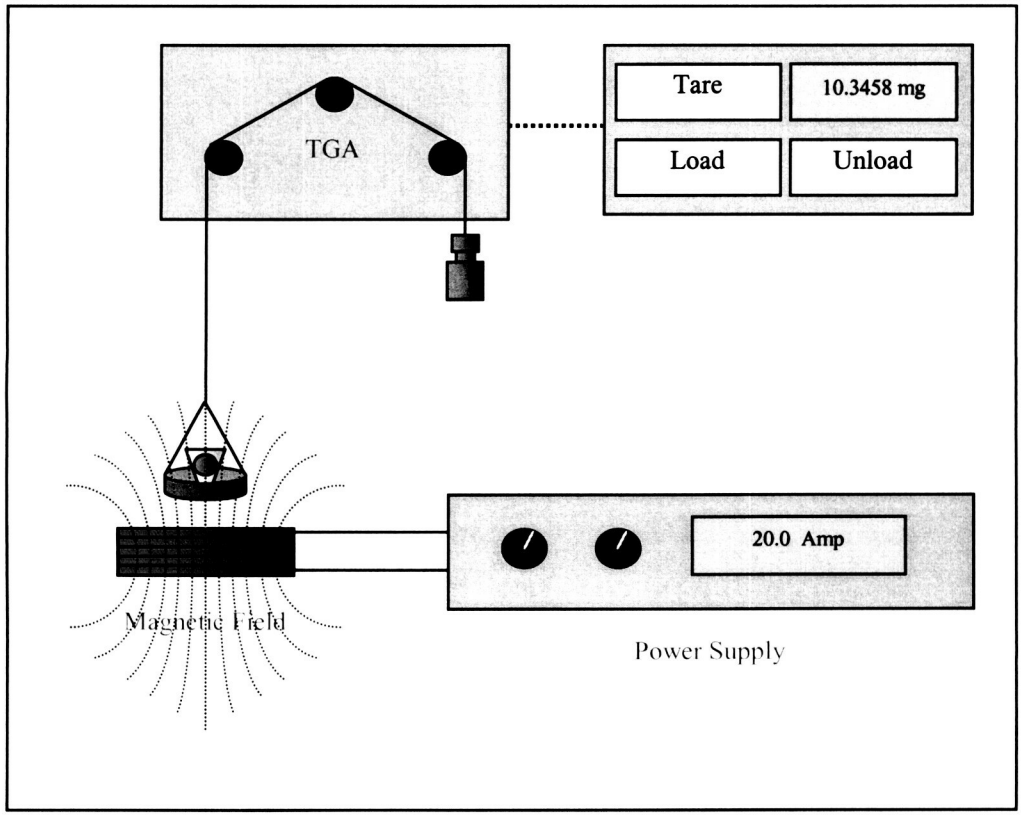

Figure 2.21. Schematic Representation of the Magnetic Susceptibility Experimental Apparatus.

The magnetic force acting on a single particle in a non-uniform magnetic field is given by,

$$\mathbf{F}_m = V\mu_0 \mathrm{M}\ \nabla \mathrm{H}$$

where V is the particle volume. Since the magnetization is proportional to the product of the particle susceptibility and the magnetic field intensity, the above equation may be expressed as,

$$\mathbf{F}_m = V\mu_0\chi_b\ \mathrm{H}\ \nabla \mathrm{H}$$

The magnetic susceptibility of the ferrite powder (χ_f) is related to the overall susceptibility of the alginate bead (χ_b) by,

$$\chi_f = \frac{\chi_b}{\phi}$$

where ϕ represents the volume fraction of ferrite powder. The ferrite volume fraction is calculated by applying the ratio between the volume occupied by the ferrite and the total bead volume. This leads to the following equation,

$$\phi = \frac{y_f \rho_b}{\rho_f}$$

where ρ_b is the bead density, ρ_f is the ferrite powder density, and y_f represents the ferrite weight fraction. Finally, considering the ferrite volumetric fraction, the magnetic force can be expressed as

$$\mathbf{F}_m = \chi_f\ \phi\ V\mu_0 \mathrm{H}\ \nabla \mathrm{H}$$

During the experiment, the canister containing the particle is positioned above the coil at the axis. The position of the particle must be measured as precisely as possible. The coil is aligned horizontally. The magnetic field generated by the electromagnet was measured directly using a gaussmeter and also estimated by a mathematical model that considers the contribution of every single loop. The model will be discussed in greater detail in the following section.

Evidence of the good agreement between theory and experiment is shown in Figure 2.22.

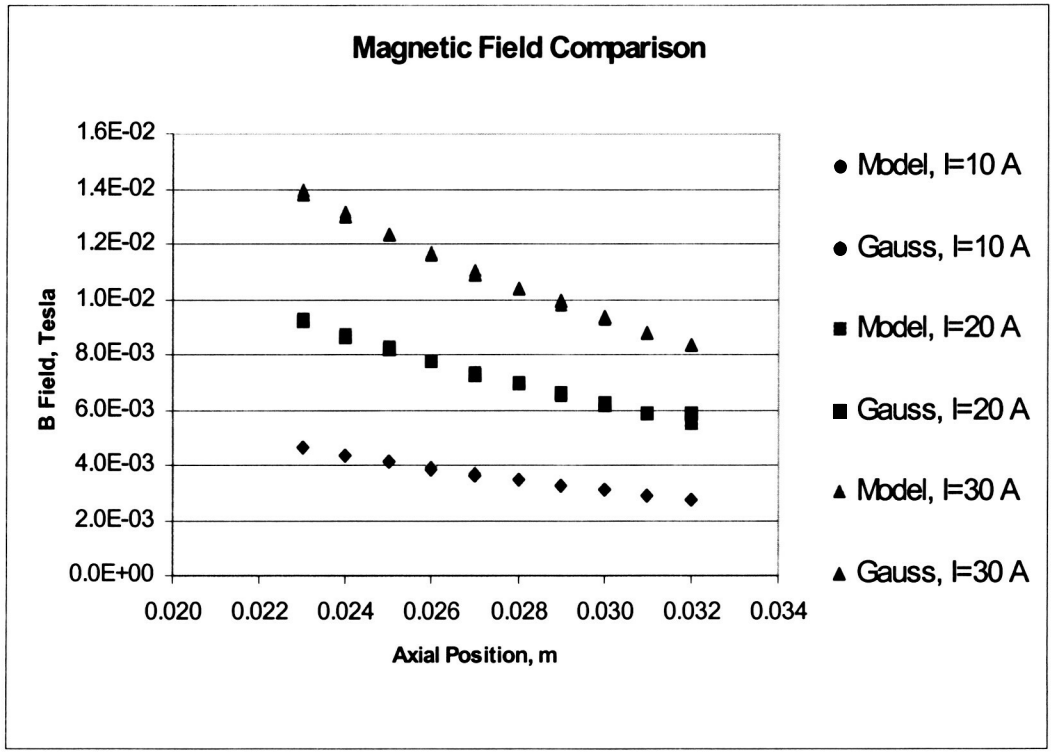

Figure 2.22. Magnetic Field Produced by Electromagnet used in the Determination of Magnetic Susceptibility.

Replicate measurements were made of the force exerted on the ferrite impregnated beads using a range of currents applied to the electromagnet. In Figure 2.23, the measured forces are plotted versus the variable magnetic field strength term. From these data, the magnetic susceptibility of the pure ferrite was determined by linear regression as the slope of the best fit line. The resultant magnetic susceptibility value was 4.88. Knowledge of the magnetic susceptibility of the ferrite material was then used in the calculation of the bulk properties of the ferrite impregnated beads.

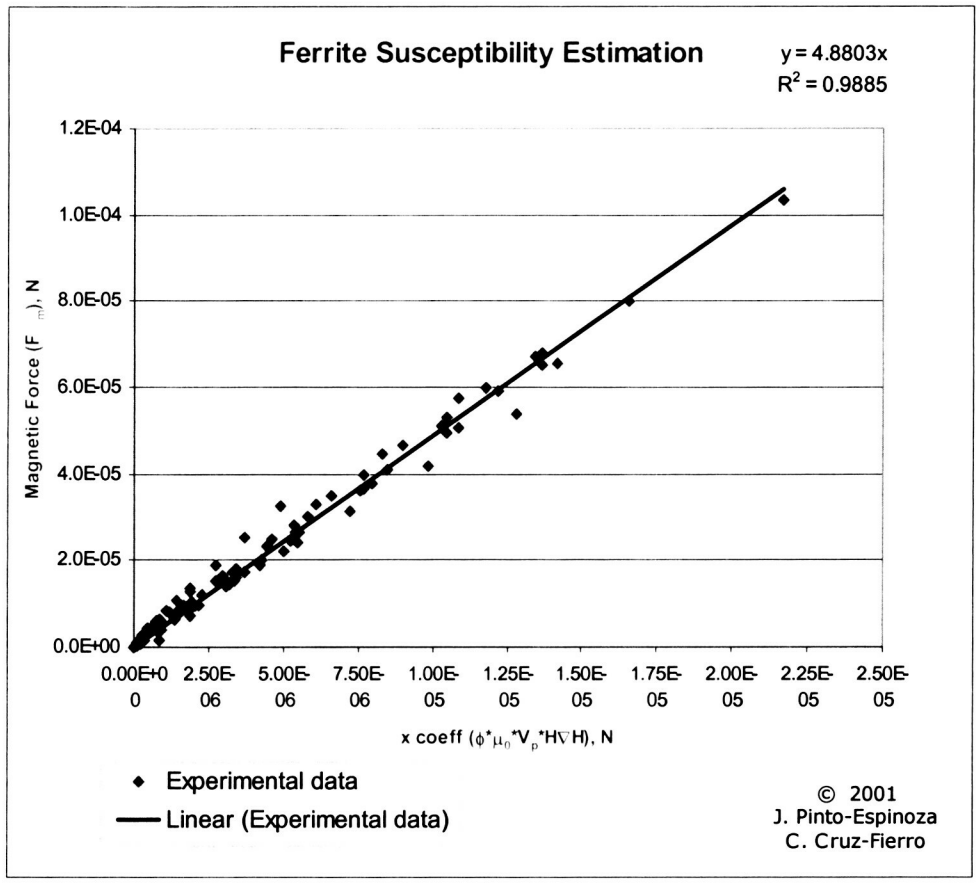

Figure 2.23. Ferrite Magnetic Susceptibility Determination from Force Measurements over a Range of Magnetic Field Intensities.

3. MAGNET DESIGNS.

Magnetic confinement, manipulation of the degree of consolidation (or conversely fluidization), and particle size stratification in a microgravity environment requires the employment of magnetic fields which produce forces of sufficient magnitude and spatial distribution. The necessary fields may be created using electromagnets, permanent magnets, or a combination of the two. The primary advantage in utilization of an electromagnet is the ease with which field strength can be controlled by varying the current. Magnetic field lines and flux density distributions for a generalized air-filled solenoid are illustrated in Figure 3.1.

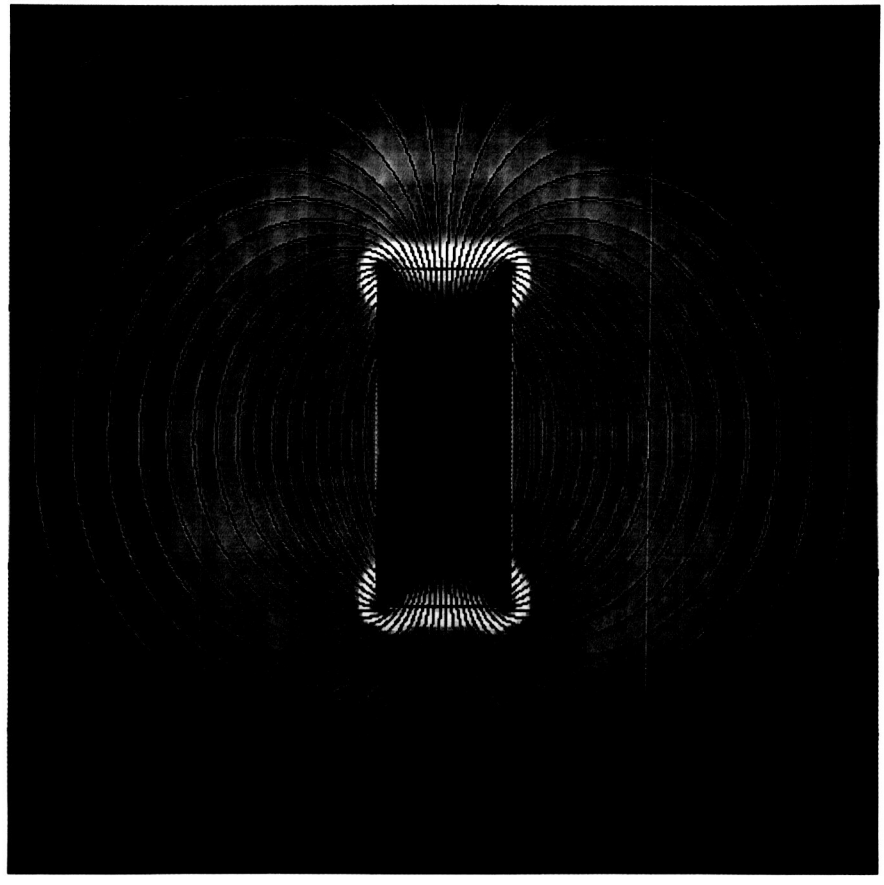

Figure 3.1. Field Lines and Magnetic Flux Density (colors) in a Generalized Air Filled Solenoid. In this representation, regions of the highest flux density values appear in red, while those of lowest flux density are dark blue.

The magnetic flux density inside a solenoid is approximated by,

$$\mathbf{B} = \frac{\mu n I}{\ell}\,\hat{\mathbf{i}}$$

where n is the number of turns, I is the current, ℓ is the length of the solenoid, and $\hat{\mathbf{i}}$ is a unit vector in the direction of **B**. This approximation is valid because of the relatively uniform field produced within the coils. More complex calculations are required to predict the spatial variations of **B** within solenoids of differing designs. An individual coil within a solenoid can be approximated by the current ring shown in Figure 3.2. For this simple system, magnetic flux density values in the axial ($\mathbf{B_z}$) and radial ($\mathbf{B_r}$) directions can be calculated from,

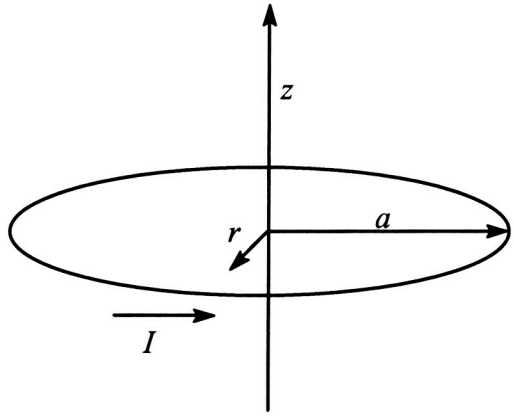

Figure 3.2. Current Ring: Radial (r), Axial (z) Distances from Center.

$$\mathbf{B}_z(\mathbf{r},\mathbf{z}) = 2 \times 10^{-4}\,\frac{I}{a}\sqrt{\frac{1}{\left(1+\frac{r}{a}\right)^2+\left(\frac{z}{a}\right)^2}}\left[K(\nu) + \frac{1-\left(\frac{r}{a}\right)^2-\left(\frac{z}{a}\right)^2}{\left(1-\frac{r}{a}\right)^2+\left(\frac{z}{a}\right)^2}\,E(\nu)\right]$$

$$\mathbf{B}_r(\mathbf{r},\mathbf{z}) = 2 \times 10^{-4}\,\frac{I}{a}\left(\frac{z}{r}\right)\sqrt{\frac{1}{\left(1+\frac{r}{a}\right)^2+\left(\frac{z}{a}\right)^2}}\left[\frac{1+\left(\frac{r}{a}\right)^2+\left(\frac{z}{a}\right)^2}{\left(1-\frac{r}{a}\right)^2+\left(\frac{z}{a}\right)^2}\,E(\nu) - K(\nu)\right]$$

where the elliptic integrals of the first and second kind are given by,

$$K(\nu^2) = \int_0^{\frac{\pi}{2}} \frac{d\theta}{\sqrt{1-\nu^2\sin^2\theta}},$$

and

$$E(\nu^2) = \int_0^{\frac{\pi}{2}} \sqrt{1 - \nu^2 \sin^2\theta}\, d\theta \ ,$$

respectively, with,

$$\nu^2 = \frac{4\,\frac{r}{a}}{\left(1+\frac{r}{a}\right)^2 + \left(\frac{z}{a}\right)^2}$$

These basic relationships can be used to model $\mathbf{B_r}$ and $\mathbf{B_z}$ arising from a solenoid by approximating each loop as a current ring, and then summing the fields of each of the equidistantly spaced rings to give total values as functions of distance in the axial (*z*) and radial (*r*) directions. With the long axis of the solenoid oriented vertically, and with the 1st current ring at the bottom of the coil, positive current flows in a counter-clockwise direction when viewed in cross section from above. As illustrated in Figure 3.3, for long thin coils, axial magnetic flux densities are fairly uniform within the solenoid, except for the regions close to the surface of the coils, and near the ends.

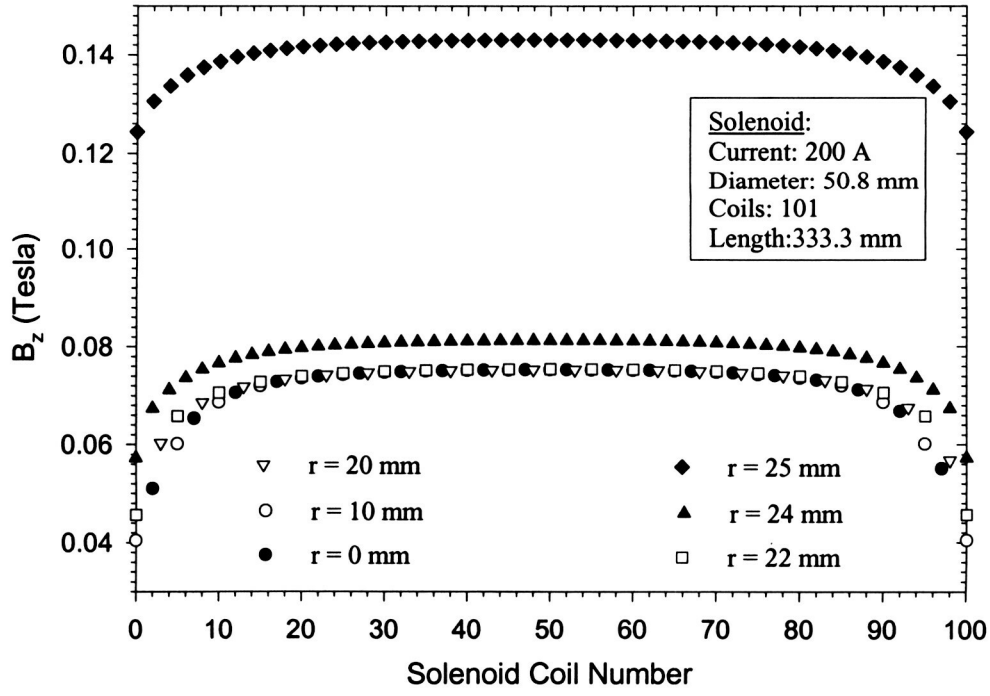

Figure 3.3. Solenoid Axial Magnetic Flux Densities at Various Radial Distances (r) from the Center.

While solenoids are capable of producing the necessary magnetic field strengths, the nearly uniform distribution inside the coils does not produce the field gradients, which are required to exert the strong magnetic force (**F**) needed for the Magnetically Assisted Filtration and Fluidization processes in microgravity.

$$\mathbf{F} = V \cdot \nabla(\mathbf{M} \cdot \mathbf{B})$$

Where V is the particle volume on which the force acts and $\mathbf{M}$ is the magnetization in that particle due to the applied magnetic field $\mathbf{B}$. Magnetic field gradients can be produced, however, using a series of coils (Helmholtz coils) in which varying current levels are supplied to successive coils, or alternatively using variable coil spacings or coil radii.

We have substantially improved our technical capability to assemble an integrated set of discrete magnetic field generating elements into an overall field of needed shape and strength within any desired accuracy. This has been achieved through the development of Fortran coded software, named Tesla-I, which calculates all design parameters needed for the magnetic field generator system. In order to design a set of modified Helmholtz coils, which will match a desired magnetic field profile, Tesla-I uses an optimization routine with an objective function that is provided by the user. The program compares the desired magnetic field profile to the solution of the Biot-Savart equation. The absolute value of the error between the two solutions is integrated over the area of interest. The optimization attempts to minimize this error while meeting the constraints set by the user (specified number of coils, maximum current, field strength, field gradient etc.). Using this software it is possible to not only optimize a set of modified Helmholtz coils for the desired magnetic field, but also for the field gradient, and even the force acting upon a magnetically susceptible object. In order to preserve accuracy when comparing the objective function to the generated field, the general forms of the field have been solved analytically and the exact solutions are used instead of a numerical solution.

Tesla-I contains two separate programs for field optimization. One is written for modified Helmholtz circular coils and the other for rectangular coils. The major difference between the two programs is that in the rectangular coils, each turn of wire is modeled as four separate lines of wire. The effect of spacing

between the wires is taken into account, and the field is calculated as if all current is passing through the center of the wire. Each turn of wire (or segment for the rectangular case) is calculated separately and then summed to provide the total field as a function of position along the *z* axis. Each coil is treated separately, allowing for greater flexibility. The number of turns (vertical and horizontal), current, wire diameter, and dimensions are all independent variables in the design of the modified Helmholtz coil. Individual coils can also be placed anywhere in relation to each other, but the coil with the lowest axial position defines the centerline for all calculations. There is no limit to the number of turns a coil can have, although the computation of the field becomes impractical with more than 100 turns per coil. The limit on coils is 1000 although more than 50 makes calculation very memory intensive and slow.

In the design of both circular and rectangular coils we start from the Biot-Savart law,

$$dB = \frac{\mu_0}{4\pi} \frac{\vec{i}\, ds \times -\vec{r}}{r^3}$$

where *i* and *r* are current and radius vectors, respectively. For the optimization program we are primarily concerned with the axial component of the field at the center of the set of coils. For the case of rectangular coils, illustrated below we expand the cross product in the Biot-Savart law and we remove all terms without a resultant axial field. Thus we obtain,

$$\vec{i}\, ds \times \vec{r} = ((i_y r_z - i_z r_y)\hat{i} + (i_z r_x - i_x r_z)\hat{j} + (i_x r_y - i_y r_x)\hat{k})ds \Rightarrow (ids \times r)_z = (i_x r_y - i_y r_x)\hat{k}ds$$

A single rectangular turn (Figure 3.4) is represented with four straight lines that define the boundaries. Each side of the rectangle represents one equation. For

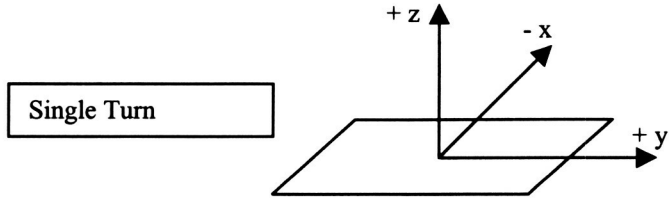

Figure 3.4 Single Turn of Rectangular Electromagnet Coil.

each turn of wire there is a fixed value of axial position *z*, and for each segment either the *x* or *y* component will also be fixed, leading to a univariate equation to be solved. An example of one line integral is the line segment parallel with the y-axis located in the positive *x* portion of the x-y plane bounded by ($-l$ = -L/2) < y < (l = L/2) shown in Figure 3.5

$$B_{i,h,v} = \frac{\mu_0}{4\pi} \int_{-l}^{l} \frac{i_y r_x}{r^3} dy$$

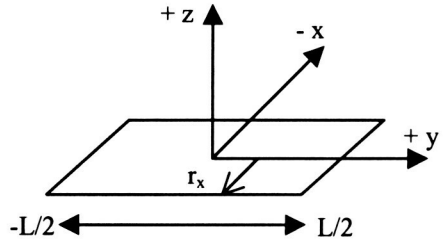

Figure 3.5 Line in Positive X portion of the X-Y Plane.

In this case r_x and i_y are constants, and r^3 can be represented by:

$$r^3 = (\sqrt{r_x^2 + r_y^2 + r_z^2})^3$$

Because we are considering a set of turns which have different positions in the vertical direction we must replace r_z with $z\text{-}z_{i,h,v}$ where the 'l' denotes the coil index, 'h' is the horizontal turn index, and 'ν' is the vertical turn index. Also we replace r_y with y.

$$r^3 = (\sqrt{r_x^2 + y^2 + (z - z_{i,h,v})^2})^3$$

After repeating this for the remaining three sides we can assemble the equation for a single turn of a modified Helmholtz coil;

$$B_{i,h,v} = \frac{\mu_0}{4\pi}\left[2i_y \left|r_x\right| \bullet \int_l^l \frac{1}{\sqrt{r_x^2 + y^2 + (z - z_{i,h,v})^2}^3} dy + 2i_x \left|r_y\right| \bullet \int_w^w \frac{1}{\sqrt{r_y^2 + x^2 + (z - z_{i,h,v})^2}^3} dx \right]$$

Now each turn of wire is summed vertically into horizontal layers which are added into coils. Finally, the coils are summed to form the complete field. Although only the first turn of wire is shown, clearly, the limits of integration will change as the coils become thicker. The derivation of these equations is simple but rather lengthy and so has been omitted.

The Tesla-I and Tesla-Ic software provides a way to design sets of electromagnetic coils to meet a variety of applications. The user provides the physical constraints of the system such as number of coils available, current limits, wire size, and the desired field profile. The program then optimizes the arrangement of the coils available to provide the best fit to the desired field profile. Besides simply matching magnetic fields, the Tesla-I series of programs can also tune coils to field gradients and force fields (product of field and gradient). The following example illustrates the utility of the Tesla-I series of programs. Here, Tesla-Ic is used to design a set of six coils to provide a constant gradient field in a cylindrical magnetically stabilized fluidized bed, such as that shown in Figure 3.6. The dimensions of the rings are summarized below in Table 3.1. The coils are numbered from the bottom up and the axial ordinate is taken as the bottom of the lowest coil.

In this case the Tesla-Ic program was run to optimize the coils for production of a constant gradient field. A target gradient of -55 mT/m was chosen with an intensity of 13 mT at the origin. Before Tesla-Ic was invoked, a preliminary configuration of electromagnetic coils was arranged, based on experience and some elementary calculations. The field intensity was measured along the centerline of the column. The coil configuration was fed into CircleView, the configuration evaluation portion of Tesla-Ic, and the results recorded. Next, the configuration of coils was entered into the optimization portion of Tesla-Ic as a

starting point. The optimization was constrained to currents of less than 30 amperes to maintain practicality. The graph shown in Figure 3.7 presents the desired field gradient, the measured and calculated field gradients, and finally the field gradient produced by the optimized coil configuration.

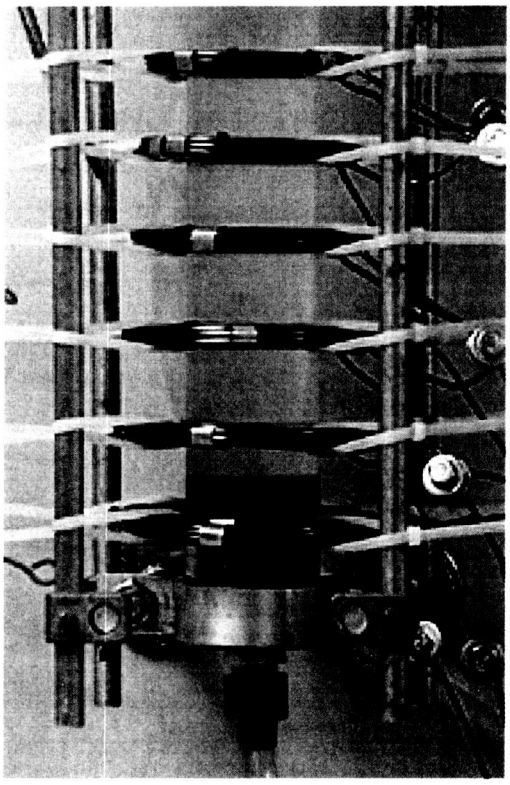

Figure 3.6 Cylindrical Magnetically Stabilized Fluidized Bed with Six Coils.

Clearly, the optimized coil design more closely matches the desired gradient. The difference between the model field and measured field can be accounted for by the error in measurement, as well as slight modeling errors. It can also be seen that all the models fit fairly closely, indicating that a better fit may only be possible by the use of additional coils. In the current version of the Tesla-I series software, coils are modeled as point lines of current. This simplification has relatively little effect on the computations, except when small diameters and large currents are employed in conjunction with large arrays of coils. The current software does take into account the spacing between coils and can even account for irregularities within the coil windings.

Table 3.1 Constant Gradient Electromagnetic Coil Configuration – Initial Design.

Coil #	Axial Position (m)	Current (A)	Vertical Turns	Horizontal Turns
1	0.00	25	3	8
2	0.042	25	3	7
3	0.084	20	3	6
4	0.124	20	3	5
5	0.163	15	3	4
6	0.200	15	3	3

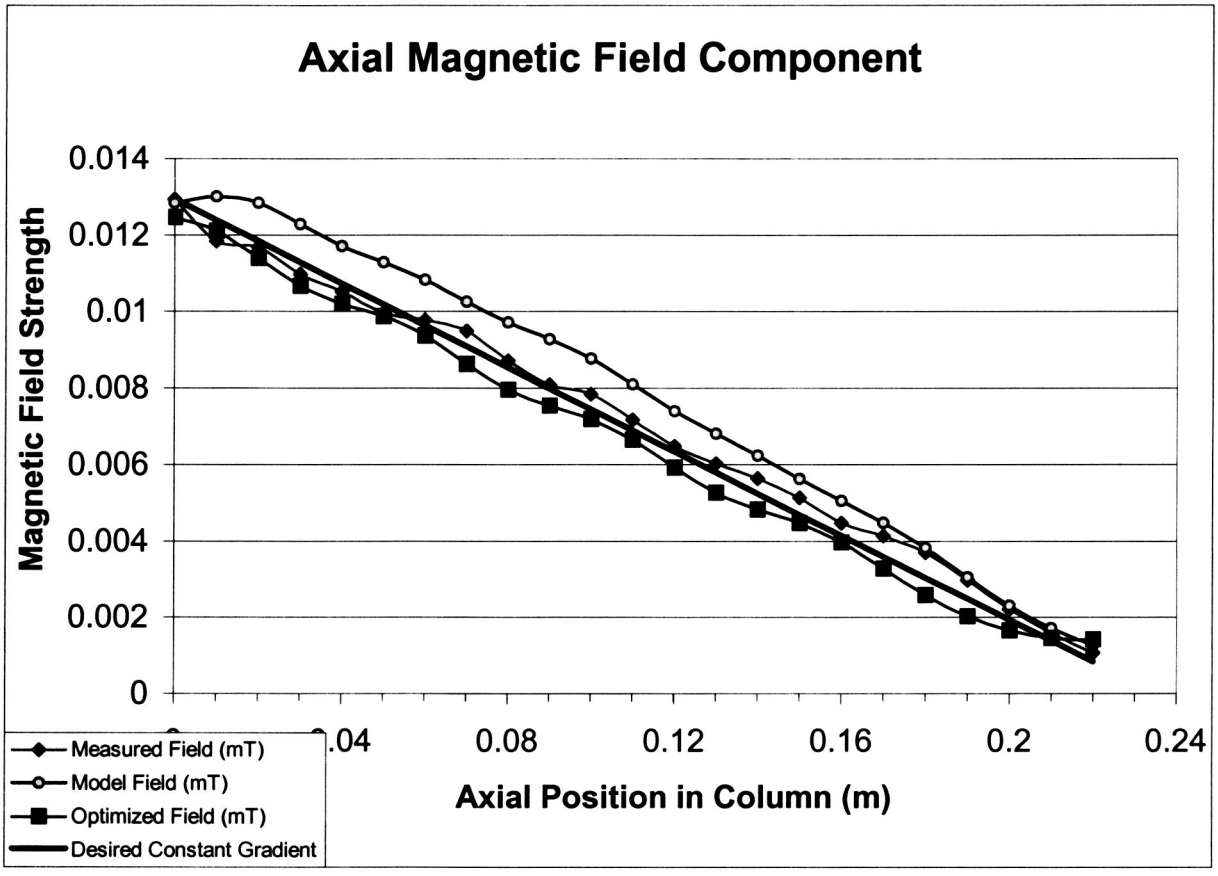

Figure 3.7 Comparison of Magnetic Field Gradients.

The Tesla-I series of software can also be used to generate input for other programs. Currently all graphical output is provided through Microsoft Excel in the form of imported data files. The software also has the ability to output the coil configuration data to Z-field, software developed in Maple IV, which produces 3-D representations of the field profiles. Using Z-field software in conjunction with Tesla-I all three individual components (*x, y, z*) of the magnetic field can be mapped over three dimensional space and displayed in any combination. This is illustrated in the design optimization of a Gradient Magnetically Stabilized Fluidized Bed based upon a set of six square coils (Figure 3.8). The centerline magnetic field (Tesla) is shown as a function of height in Figure 3.9, which illustrates both individual contributions of all coils and the resultant field. Z-field

can also display 3-D field plots in a variety of formats such as the cross sectional slice in the x-y plane shown in Figure 3.10. The field can also be profiled for y-z and x-z coordinates as in Figures 3.11 and 3.12, respectively.

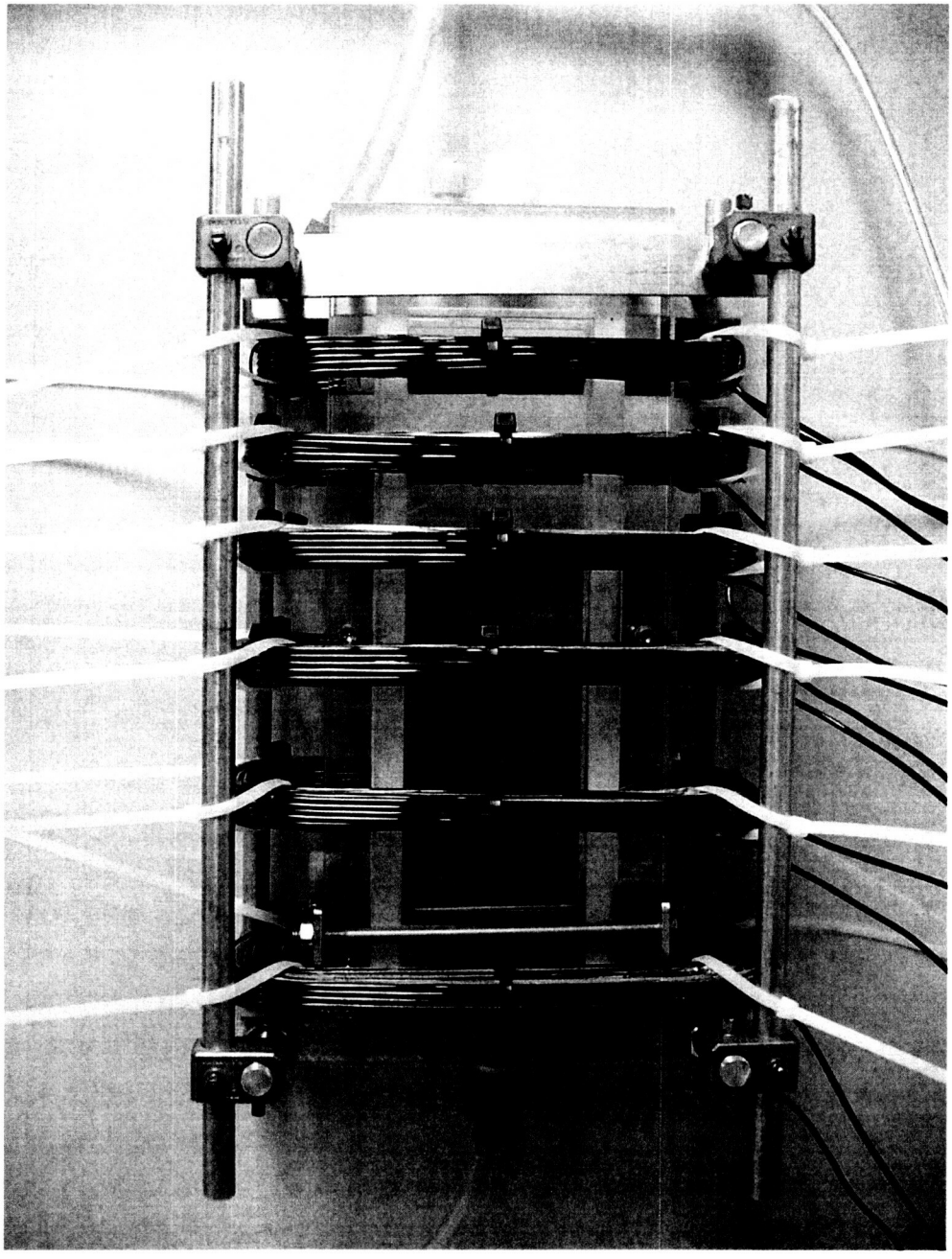

Figure 3.8 Constant Gradient Magnetically Stabilized Fluidized Bed in Square Coil Geometry.

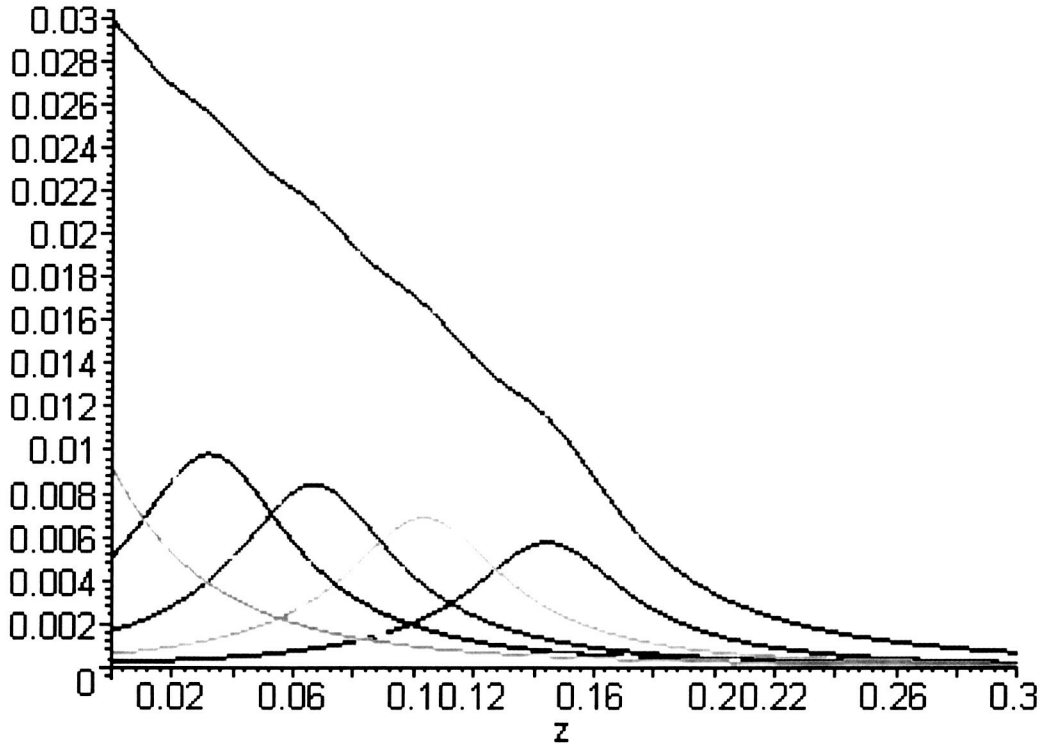

Figure 3.9. Fields from Individual Coils and Cumulative Field to Produce a Constant Axial Magnetic Field Gradient.

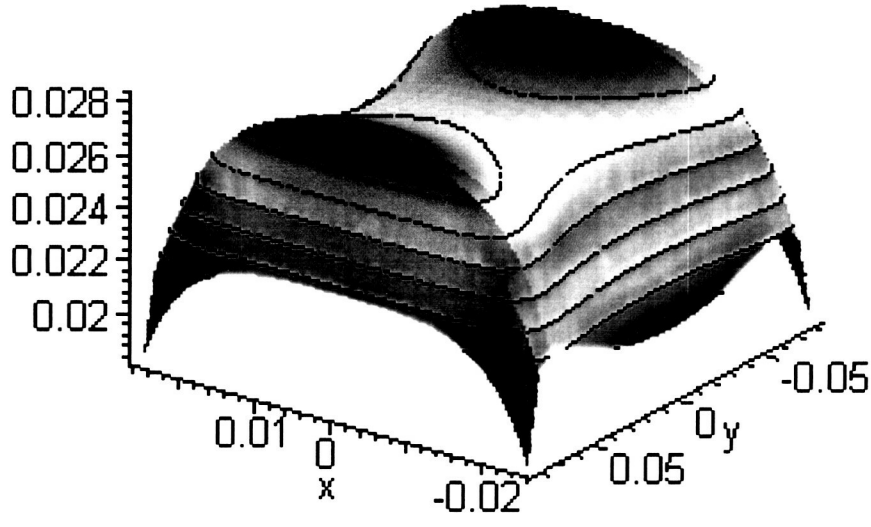

Figure 3.10. Field Cross Section Through Cylindrical Coils.

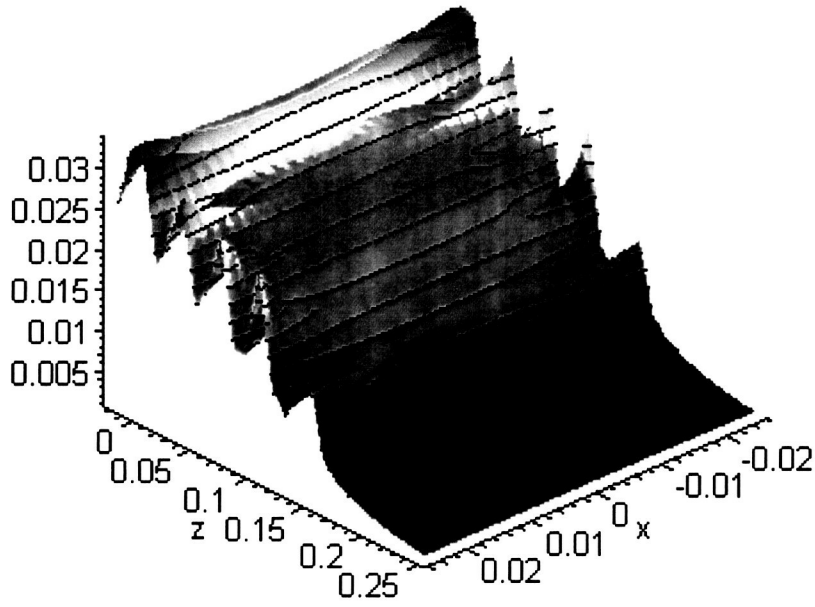

Figure 3.11. Z-Field Output in the X-Z Plane.

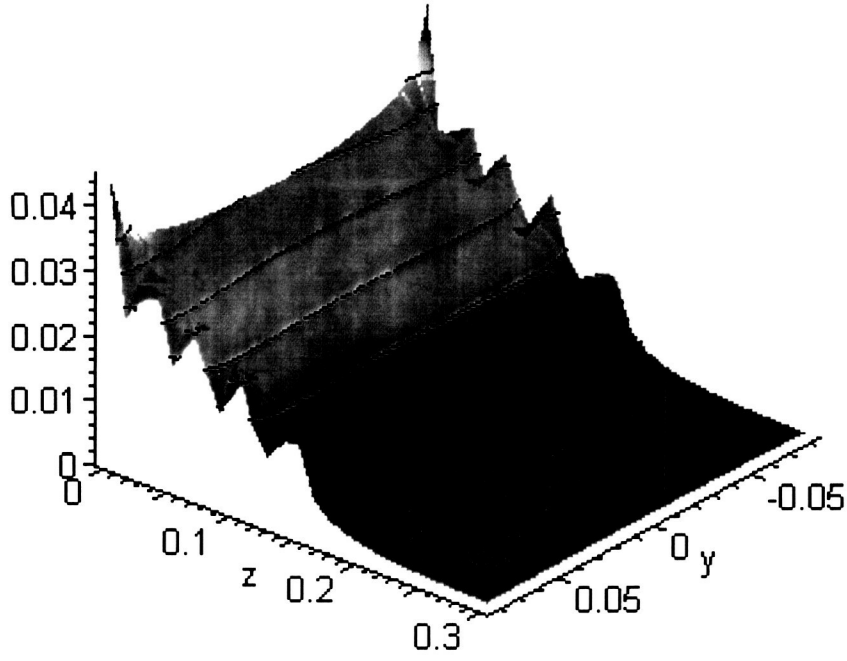

Figure 3.12. Z-Field Output in the Y-Z Plane

Having developed the Tesla-I electromagnet design software, the creation of a series of coils to produce a constant magnetic force along the *z*-axis of the Magnetically Stabilized Fluidized Bed was investigated. In order to design a system of coils that can provide a constant magnetic force, an equation for force per unit volume as a function of magnetic field was developed.

$$F_z \propto \chi \times B_z \times \frac{dB_z}{dz}$$

Here χ is the susceptibility of the particle in the magnetic field and B_z is the field in the *z* direction. The constant of proportionality in the above equation is $1/\mu_o$. By setting the force per unit volume in the *z* direction constant, the expression becomes,

$$C_1 = \chi \times B_z \times \frac{dB_z}{dz} \rightarrow B_z \times \frac{dB_z}{dz} = \frac{C_1}{\chi}$$

Now, by integrating the expression we have:

$$\int B_z dB_z = \int \frac{C_1}{\chi} dz \Rightarrow \frac{B_z^{\,2}}{2} = \frac{C_1}{\chi} \times z$$

Rearranging the expression we have the final form, which is then used with the Tesla-I software to provide the necessary coil configuration.

$$B_z = \sqrt{\frac{2C_1}{\chi} \times z}$$

This approach was validated using a system of eighteen cylindrical coils. The coils are optimized to provide constant force to a tubular fluidized bed reactor 16 cm in length. The coils are all of the same diameter and construction. The specifications for the coils resulting from this exercise are shown in Table 3.2. Comparisons between the desired (tune) and values calculated from the optimum design for the magnetic field strength and magnetic force versus axial distance are shown in Figures 3.13 and 3.14, respectively. It is important to note that these are

not ideal coils, and therefore the force produced is not perfectly constant. It should be emphasized that this is only a simple solution to the problem of developing a constant force field profile. There are several ways to improve the quality of the field produced. By increasing the number of coils, smoother transitions between coils result which lead to smaller swings in the field gradient, thereby greatly improving the homogeneity of the resulting force field. Coils can also be made with a larger radius, which again cuts down on deviations arising from the derivative term in the force equation.

Table 3.2. Coil specifications for Constant Force Electromagnet.

Coil No.	Z-pos(m)	Current (A)	Vertical Turns	Horiz. Turns	Radius (m)	Wire Dia.(m)
1	-0.3	7.912	4	5	0.05	0.0021
2	-0.139	6.493	4	5	0.05	0.0021
3	-0.065	0.215	4	5	0.05	0.0021
4	-0.04	-1.477	4	5	0.05	0.0021
5	-0.027	-2.162	4	5	0.05	0.0021
6	-0.025	-3.019	4	5	0.05	0.0021
7	-0.015	2.496	4	5	0.05	0.0021
8	0.031	4.908	4	5	0.05	0.0021
9	0.073	2.609	4	5	0.05	0.0021
10	0.085	3.241	4	5	0.05	0.0021
11	0.122	4.154	4	5	0.05	0.0021
12	0.125	2.207	4	5	0.05	0.0021
13	0.165	7.476	4	5	0.05	0.0021
14	0.212	3.016	4	5	0.05	0.0021
15	0.213	8.158	4	5	0.05	0.0021
16	0.217	2.258	4	5	0.05	0.0021
17	0.228	1.751	4	5	0.05	0.0021
18	0.242	0.062	4	5	0.05	0.0021

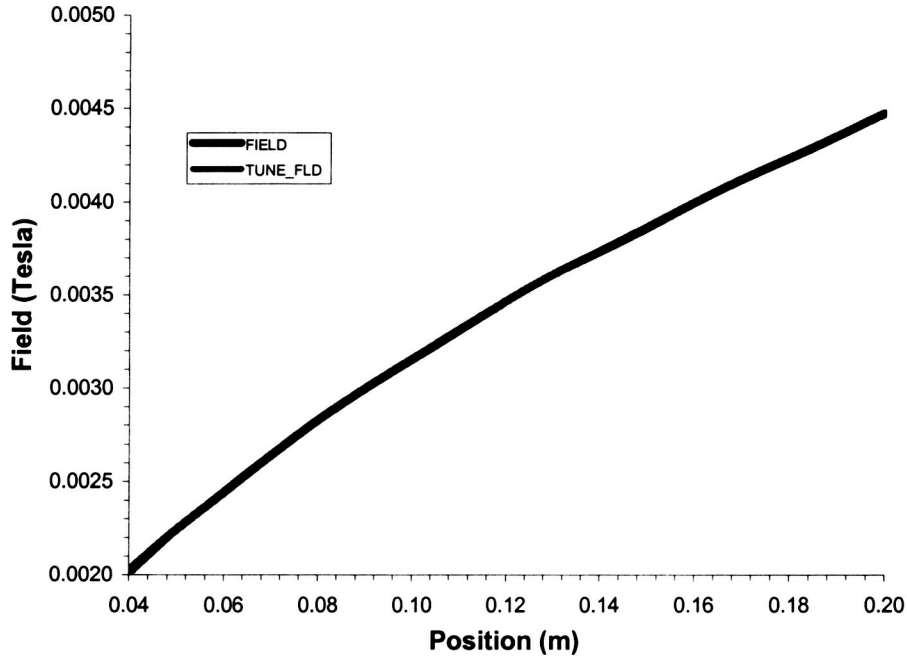

Figure 3.13. Field Profile for Constant Force Magnet Design.

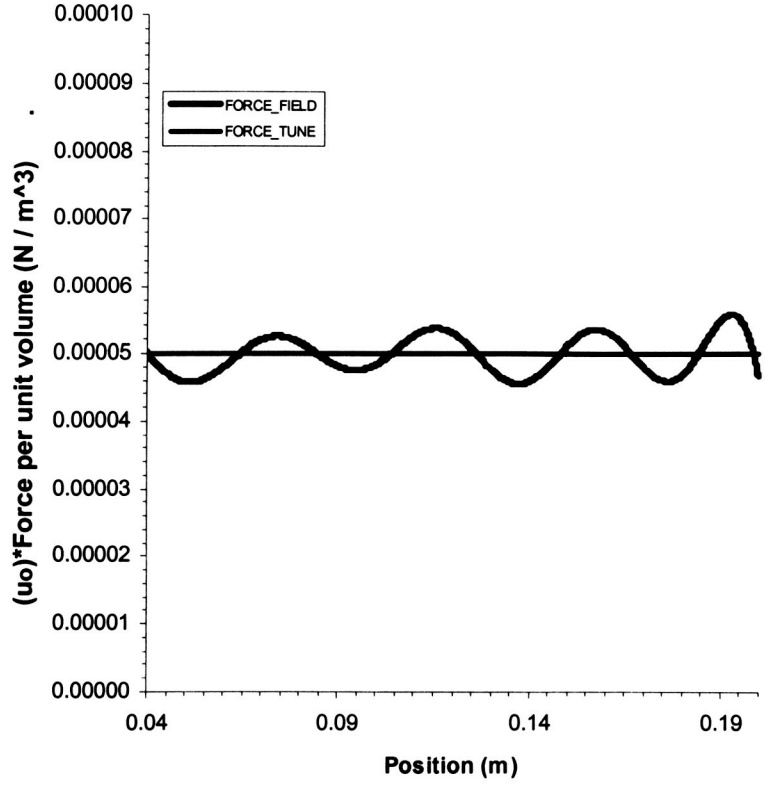

Figure 3.14. Magnetic Force Profile for Constant Force Magnet Design.

4. MATHEMATICAL MODELING AND NUMERICAL SIMULATION.

Accurate predictive mathematical models were needed to facilitate the investigation of magnetic control methods and the design of associated hardware. In addition to the electromagnet design software discussed in the previous section, mathematical models were also developed which describe Gradient Magnetically Assisted Fluidization and Magnetically Assisted Filtration processes. Two lines of inquiry were pursued regarding fluidization phenomena: a Fortran coded Voidage Distribution Model was developed from first principals, and this work was augmented by numerical simulations performed using custom modified computational fluid dynamics code.

4.1 The Voidage Distribution Model. The Voidage Distribution Model (VDM) is a discrete particle method (DPM) theoretical fluid-dynamic treatment describing behavior of granular ferromagnetic media in non-homogenous magnetic and fluid flow fields. This model simulates the fluidization of ferromagnetic media under variable conditions of magnetic field strength, magnetic field gradient, particle density, fluid density and viscosity, flow rate, and gravity. Fluid (water) and particulate phases are represented as two interacting continua[50,51]. The VDM consists of equations of continuity*,

$$\frac{\partial \varepsilon}{\partial t} + \nabla \cdot (\varepsilon U) = 0 \qquad \frac{\partial (1-\varepsilon)}{\partial t} + \nabla \cdot \left[(1-\varepsilon) V \right] = 0$$

and equations of motion,

$$\rho_f \varepsilon \left(\frac{\partial U}{\partial t} + (U \cdot \nabla) U \right) = -\varepsilon \nabla P_f - \varepsilon \nabla \cdot \tau_f + \rho_f \varepsilon g - \varepsilon F_1$$

* Nomenclature for the VDM are summarized on page 46.

$$\rho_p(1-\varepsilon)\left(\frac{\partial V}{\partial t}+(V\cdot\nabla)V\right)=-(1-\varepsilon)\nabla P_f-(1-\varepsilon)\nabla P_p-(1-\varepsilon)\nabla\cdot\tau_p+\rho_p(1-\varepsilon)\varepsilon g+\varepsilon F_1+F_m$$

for the fluid and solid phases, respectively. Here F_1 is the force between fluid and solids, and F_m is the magnetic force acting on the ferromagnetic particles.

$$F_1=\beta(\varepsilon)U+\frac{(1-\varepsilon)}{\varepsilon}C(\varepsilon)\rho_f\frac{d(U-V)}{dt} \qquad \beta(\varepsilon)=\frac{150(1-\varepsilon)^2\mu_f}{D_p^2\varepsilon^2}$$

$$F_m=\mu_0(1-\varepsilon)M_p\nabla H$$

The following specific experimental conditions and assumptions were used in this study:

(1) The magnetic field intensity is highest at the bottom of the bed and decreases linearly with the height of the bed.

(2) The system is symmetrical in the θ direction (cylindrical column). Therefore, any derivative with respect to θ can be neglected.

(3) The system is at steady state.

(4) The mean particle velocity is assumed to be zero, **V** = 0. With this assumption, all terms that include the particle velocities, v_r, v_θ,and v_z, or their derivatives are negligible.

(5) The fluid phase is treated as an inviscid flow except for mutual interaction with the particle phase. Therefore, the stress tensor (τ) terms in the liquid phase can be ignored.

(6) The magnetic field intensities in r and θ directions are much smaller than the field intensity in the z direction. Therefore, the magnetic field intensity in r and θ directions in can be ignored.

(7) The virtual mass force due to the relative acceleration between fluid and particle is small compared to the force due to gravity.

(8) The distribution of flow inside the column is assumed to be plug flow (u_r and u_θ are much smaller than u_z.

(9) The magnetic forces in the r and θ directions are small compared to the magnetic force in the z direction.

(10) The momentum terms due to the change of fluid velocity are small compared to the gravitational, drag, and magnetic forces.

(11) There is no gravitational acceleration in r and θ directions.

With the specific experimental conditions and assumptions listed above, the set of governing equations and the magnetic force equations yield the following solution:

$$\frac{\partial \varepsilon}{\partial z/L} = \frac{\varepsilon^3 - \alpha(1-\varepsilon) - \phi - \gamma H \varepsilon^3}{\pi E \varepsilon^3}$$

where

$$\alpha = \frac{150\mu_f u_0}{d_p^2(\rho_p - \rho_f)g}, \qquad \phi = \frac{1.75\rho_f u_0^2}{d_p(\rho_p - \rho_f)g},$$

$$\pi = \frac{1}{(\rho_p - \rho_f)gL} \qquad \gamma = \frac{\mu_0 \chi}{(\rho_p - \rho_f)g}\frac{dH}{dz}$$

with the boundary conditions: $z/L = 1$, $\varepsilon = 1$.

These equations were solved numerically, first using Maple V, and then using algorithms coded and compiled into Fortran. Numerical predictions of the VDM model were fitted to experimental laboratory data obtained at 1g. Additionally, flight experiments were conducted under gravity conditions ranging from 0g to 2g.

VDM Nomenclature

ρ_f	Fluid density (kg/m^3)
ρ_p	Particle density (kg/m^3)
ε	Void fraction of bed (/)
τ_f	Fluid stress tensor (N/m^2)
τ_p	Particle stress tensor (N/m^2)
μ_0	Magnetic permeability of free space ($4\pi \times 10^{-7}$) ($kg\ m/A^2s^2$)
μ_b	Magnetic permeability of the bed mixture ($kg\ m/A^2s^2$)
μ_f	Viscosity of the fluid phase ($N\ s/m^2$)
d_p	Average particle diameter (m)
E	Elastic modulus of the fluidized bed (N/m^2)
F_l, F_d	Interface interaction force between fluid and particle (N/m^3)
F_b	Buoyancy force exerted on the particle (N/m^3)
F_g	Gravitational force exerted on the particle (N/m^3)
f_m	Interparticle magnetic force due to the magnetization (N)
F_m	Magnetic force exerted on the particle (N/m^3)
g	Gravitational acceleration (m/s^2)
h	Height of the bed (m)
h_{in}	Initial height of the bed (m)
H	Magnetic field intensity (A/m)
M_p	Magnetization of the particle (A/m)
P_f	Total fluid pressure (N/m^2)
P_p	Effective pressure in particle phase (N/m^2)
t	Time (s)
u_x, u_y, u_z	Interstitial fluid velocity in x, y and z components (m/s)
U	Velocity of fluid phase (m/s)
U_0	Superficial fluid velocity (m/s)
v_x, v_y, v_z	Interstitial fluid velocity in x, y and z components (m/s)
V	Velocity of particle phase (m/s)
x, y, z	Cartesian coordinates

4.2 Computational Fluid Dynamics Simulations.

Computational fluid dynamics (CFD) simulations were also used to study the effects of variable magnetic field gradients and variable gravity conditions on fluidization phenomena[52]. Star CD, a commercially available CFD package, was utilized. The Lagrangian-Eulerian approach implies that both phases interact with each other. Normally, the carrier fluid is the continuous phase, which can be gaseous or liquid. The discrete or dispersed phase is in the form of solid particles, liquid droplets, or gas bubbles. In the case of fluidized beds, the dispersed phase consists of solids. Following is a summary of the relationships used by the CFD program*.

Conservation Equations of the Liquid Phase:

$$\frac{1}{\sqrt{g}}\frac{\partial}{\partial t}\left(\sqrt{g}\,\rho\varepsilon\right)+\frac{\partial}{\partial x_j}\left(\rho\varepsilon\tilde{u}_j\right)=s_m$$

$$\frac{1}{\sqrt{g}}\frac{\partial}{\partial t}\left(\sqrt{g}\,\rho\varepsilon u_i\right)+\frac{\partial}{\partial x_j}\left(\rho\varepsilon\tilde{u}_j u_i-\tau_{ij}\right)=\frac{\varepsilon\partial p}{\partial x_i}+s_i$$

Constitutive relations:

Laminar regime

$$\tau_{ij}=2\mu\varepsilon s_{ij}-\frac{2}{3}\mu\varepsilon\frac{\partial u_k}{\partial x_k}\delta_{ij}$$

$$s_{ij}=\frac{1}{2}\left(\frac{\partial u_i}{\partial x_j}+\frac{\partial u_j}{\partial x_i}\right)$$

* CFD Nomenclature are summarized on page 51.

Turbulent regime

$$\tau_{ij} = 2\mu\varepsilon s_{ij} - \frac{2}{3}\mu\varepsilon\frac{\partial u_k}{\partial x_k}\delta_{ij} - \overline{\rho}\varepsilon\overline{u_i' u_j'}$$

Sources:

Buoyant forces

$$s_i = g_i(\rho - \rho_0)$$

Rotational forces

$$s_i = f(u_k, \omega_k, r_k)$$

Conservation Equations of the Solid Phase:

The conservation equations for droplets in the Lagrangian framework are as follows:

Momentum

$$m_d \frac{d\vec{u}_d}{dt} = \vec{F}_{dr} + \vec{F}_p + \vec{F}_{am} + \vec{F}_b + \vec{F}_M$$

where the drag force, $\vec{F}_{dr}$, is given by,

$$\vec{F}_{dr} = \frac{1}{2}C_d\rho A_d|\vec{u} - \vec{u}_d|(\vec{u} - \vec{u}_d)$$

the pressure force, $\vec{F}_p$, is given by,

$$\vec{F}_p = -V_d\nabla p$$

the virtual mass force, $\vec{F}_{am}$, is given by,

$$\vec{F}_{am} = -C_{am}\rho V_d\frac{d(\vec{u}_d - \vec{u})}{dt}$$

the body force, $\vec{F}_b$, is obtained by

$$\vec{F}_b = m_d \vec{g}$$

and the external magnetic force, $\vec{F}_M$, is calculated from

$$\mathbf{F}_m = V\mu_0 M \nabla H$$

Knowledge of the droplet velocity allows the droplet's instantaneous position vector $\vec{x}_d$ to be determined by integrating:

$$\frac{d\vec{x}_d}{dt} = \vec{u}_d$$

$$\tau_M = \frac{m_d|\vec{u} - \vec{u}_d|}{|\vec{F}_{dr}|} = \frac{2m_d}{C_d \rho A_d |\vec{u} - \vec{u}_d|} = \frac{4\rho_d D_d}{3C_d \rho |\vec{u} - \vec{u}_d|}$$

The Drag Coefficient, C_d, uses the standard correlation,

$$C_d = \begin{cases} 24\left(1 + 0.15\mathrm{Re}_d^{0.687}\right)/\mathrm{Re}_d & \mathrm{Re}_d \le 10^3 \\ 0.44 & \mathrm{Re}_d > 10^3 \end{cases}$$

where the Re_d is the droplet Reynolds number, defined as

$$\mathrm{Re}_d = \frac{\rho|\vec{u} - \vec{u}_d|D_d}{\mu}$$

Graphical output from a CFD simulation run is shown in Figure 4.1. This simulation represents a liquid-solid fluidized bed under variable magnetic field strengths and variable gravity. The solid phase is composed of ferromagnetic media. Distributions of solid and liquid phases are illustrated as a series of time-slices moving from left to right. At t_o, the first time-slice indicates the initial

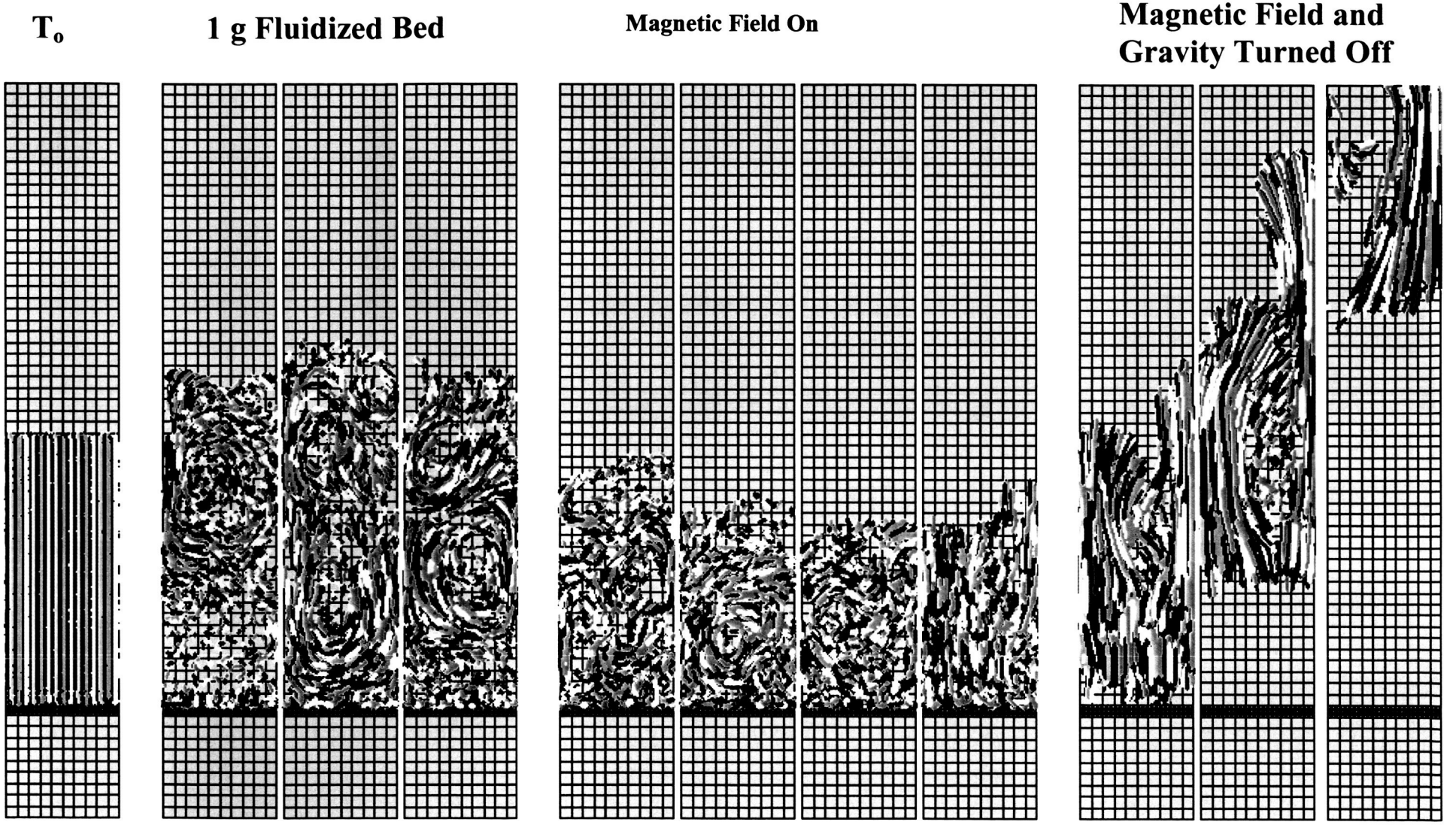

Figure 4.1. Computational Fluid Dynamics Simulation. From Left to Right: Frame 1 – Initial position of ferromagnetic media, Frames 2,3,4 – Fluidized Bed under 1 g and no magnetic field, Frames 5,6,7,8 – Magnetic Field Applied (bed contracts), Frames 9,10,11 – Magnetic Field and Gravity Set to Zero.

positions of particles as a series of vertical multicolored bars. The next three time slices illustrate a typical highly fluidized bed under normal gravity without the aid of a magnetic field. The next four time slices illustrate the effects of an applied magnetic field in which both the field and gradient vectors point down toward the bottom of the bed. This pulls the ferromagnetic particles toward the distributor plate, reducing the height of the bed and the void fraction. Following this, the last four pictures show the effects of simultaneously removing both gravity and the magnetic field. Here, in the absence of any countervaling force, the fluid pushes the particles up and out of the system.

Computational Fluid Dynamics Nomenclature.

Symbol	Description	Units
A_d	particle cross sectional area	m^2
C_{am}	virtual mass coefficient	—
C_d	drag coefficient	—
D_d	particle diameter	m
$D_{d,1}$; $D_{d,2}$	diameter of particles 1 and 2, respectively	m
E_{coal}	probability of particle coalescence	—
$E_{1,2}$	collision efficiency	—
$\vec{F}_{am}$	virtual mass force	N
$\vec{F}_b$	body force	N
$\vec{F}_{dr}$	drag force	N
$\vec{F}_p$	pressure force	N
$\sqrt{g}$	determinant of metric tensor	$(m/s^2)^{1/2}$
g_i	gravitational acceleration component in direction x_i	m/s^2
m	number of particles that take part in the coalescence	—
m_d	particle mass	kg
$N_{d,2}$	number of particles in the second parcel	—
$N_{r,1}$; $N_{r,2}$	random numbers 1 and 2, respectively	—
n'	mean value for Poisson distribution	—
P_n	probability that particle 1 undergoes n collisions	—
p	piezometric pressure	Pa
∇p	pressure gradient of the fluid	Pa
r_k	radius vector	m

s_i	momentum source components	Pa/m
s_{ij}	rate of strain tensor	s^{-1}
s_m	mass source	$kg/m^3 \cdot s$
t	time	s
δt	time interval	s
$\vec{u}$	instantaneous fluid velocity	m/s
$\vec{u}_d$	instantaneous particle velocity	m/s
$u_{d,1}; u_{d,2}$	velocity of particles 1 and 2, respectively	m/s
u_i	absolute fluid velocity component in direction x_i	m/s
u_i'	turbulent velocity fluctuations	m/s
$\widetilde{u}_j$	relative velocity between fluid and local coordinate frame that moves with velocity u_{cj}	m/s
$\overline{u_i'u_j'}$	time-averaged turbulent velocity fluctuations	m^2/s^2
V_d	particle volume	m^3
δV	cell volume	m^3
W	dimensionless parameter for collision efficiency	—
$\vec{x}_d$	instantaneous particle position	m
x_i	Cartesian coordinates	m
γ	particle diameters ratio	—
δ_{ij}	Kronecker delta; $\delta_{ij} = 1$ if $i = j$, otherwise $\delta_{ij} = 0$	—
ε	void fraction	—
μ	molecular dynamic fluid viscosity	Pa·s
ν	particle collision frequency	s^{-1}
ρ	fluid density	kg/m^3
$\overline{\rho}$	time-averaged fluid density	kg/m^3
ρ_0	reference density	kg/m^3
$\rho_{d,2}$	density of particle 2	kg/m^3
σ	surface tension	N/m
τ_{ij}	stress tensor components	Pa
ω_k	rotation vector	rad/s
Re_d	particle Reynolds number	—
We_L	particle Weber number	—
We_{boun}	bouncing Weber number	—

4.3 Magnetically Assisted Filtration Modeling. A mathematical model for solid waste collection in a magnetically consolidated depth filter was developed as a predictive tool. A schematic representation of the Gradient Magnetically Assisted Filtration (GMAF) filtration process is shown in Figure 4.2. In this representation, *C(t)* denotes the suspended solids concentration [kg/m^3 liquid] in the holding tank and F is the flow rate of liquid containing solid waste [m^3 liquid/s]. System boundary I represents the region of the experimental apparatus, including holding tank, pump and flow meter, where only the solid waste particles are present. It is assumed that in this volume the fluid is very well mixed, and hence the particulate concentration is uniform. System boundary II represents the region where the filtration process takes place.

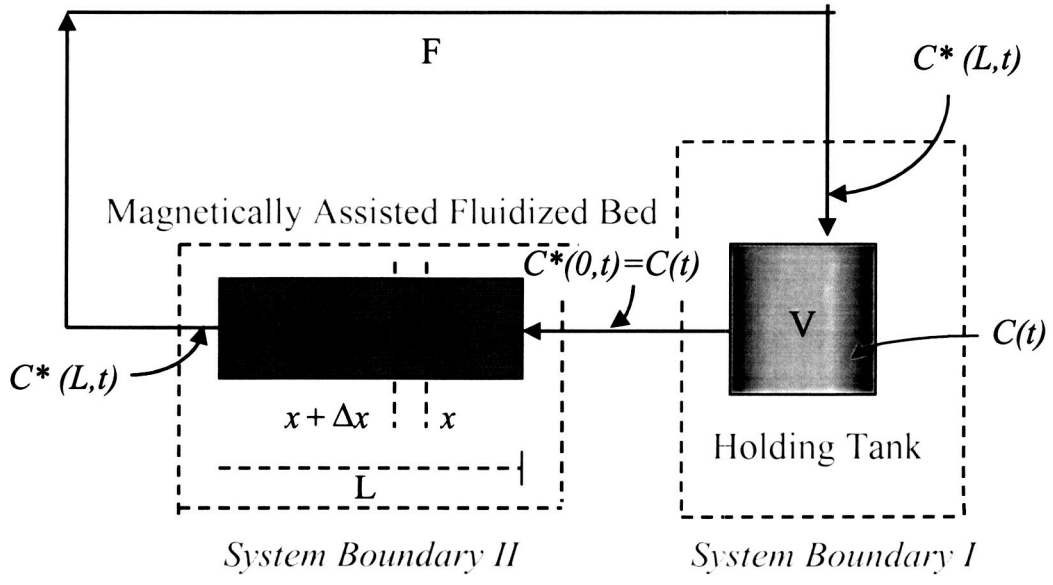

Figure 4.2. Schematic Representation of the GMAF Model.

The differential equations describing the capture of waste solids are as follows:

System Boundary I:

$$FC^*(L,t) - FC(t) = V\frac{\partial C(t)}{\partial t}$$

Initial condition: $C(0) = C_0;\ \ t = 0$

System Boundary II:

$$-\frac{F}{A}\frac{\partial C^*(x,t)}{\partial x}-\left[a\cdot k_1 C^*(x,t)-a\cdot k_2\sigma(x,t)\right]=\varepsilon_o\frac{\partial C^*(x,t)}{\partial t}$$

Initial condition: $C^*(x,0)=0;\quad t = 0,\ 0 < x \le L$

Boundary conditions: $C^*(0,t)=C(t);\quad x = 0,\ t > 0$

$C^*(0,0)=C(0);\quad x = 0,\ t = 0$

The rate of filtration:

$$\frac{\partial\sigma(x,t)}{\partial t}=k_1 C^*(x,t)-k_2\sigma(x,t)$$

Initial condition: $\sigma(x,0)=0;\ \ 0 \le x \le L$

Solution of the differential equation yielded the following expression for solid waste concentration as a function of time.

$$\ln\frac{\left[C-\frac{\varepsilon_0 k_2 C_0}{(ak_1+\varepsilon_0 k_2)}\right]}{\left[C_0-\frac{\varepsilon_0 k_2 C_0}{(ak_1+\varepsilon_0 k_2)}\right]}=\frac{F}{V}\left[\exp\left(-\frac{(ak_1+k_2\varepsilon_0)}{v}L\right)-1\right]t$$

In the above equation, C [kg/m^3 liquid] and σ [kg/m^2 surface] denote the concentrations of the solid waste particles in the liquid and in the particle phases, respectively.

Using numerical methods, these equations were solved simultaneously to determine values for k_1 [m^3 liquid/m^2 surface-s] and k_2.[1/s], the accumulation and detachment coefficients.

Magnetically Assisted Filtration Model Nomenclature

A	cross-sectional area of the bed [m^2]
a	particle surface per unit volume of the bed [m^2 particle/m^3 bed]
C	concentration of solids in the liquid in the tank [mg/m^3 liquid]
C*	concentration of solids in the bed [mg/m^3 liquid]
F	flow rate [m^3 liquid/s]
k_1	accumulation coefficient [m^3-liquid/m^2-surface-s]
k_2	detachment coefficient [s^{-1}]
L	total length of the bed [m]
t	time [s]
v	velocity of fluid [m/s]
V	total volume in the storage tank [m^3]
σ	concentration of solids on the surface of the particles [mg/m^2 particle]
ε_0	voidage of the bed

5. MAGNETICALLY ASSISTED FILTRATION.

Filtration experiments were conducted using the apparatus presented schematically in figure 4.2. Ferrite impregnated calcium alginate beads (20% ferrite, d_p = 2.2 mm) were used as the magnetically consolidated filtration media. Comminuted wheat straw particles suspended in an aqueous stream were recirculated between a holding tank and the magnetically consolidated filter bed under fixed flow rate and magnetic field intensities. Loading of the filter was monitored by the reduction in particulate concentration within the holding tank as a function of time, as determined by changes in optical density of the suspension. These measurements were made over a range of flow rates and magnetic field strengths. The magnetic field intensity inside the filter column was created such that the field intensity was highest at the bottom of the bed, and then decreased linearly toward the top of the column (i.e., a constant gradient configuration). This arrangement produced a direct magnetic force on the ferromagnetic filter media which was oriented downward toward the distributor plate, and fixed the media in position. To confirm the production of a nearly constant gradient magnetic field inside the filter bed, the axial field intensity at the center of the cylindrical bed was measured using a gaussmeter between the distributor and a height of ~ 0.3 m, as shown in Figure 5.1.

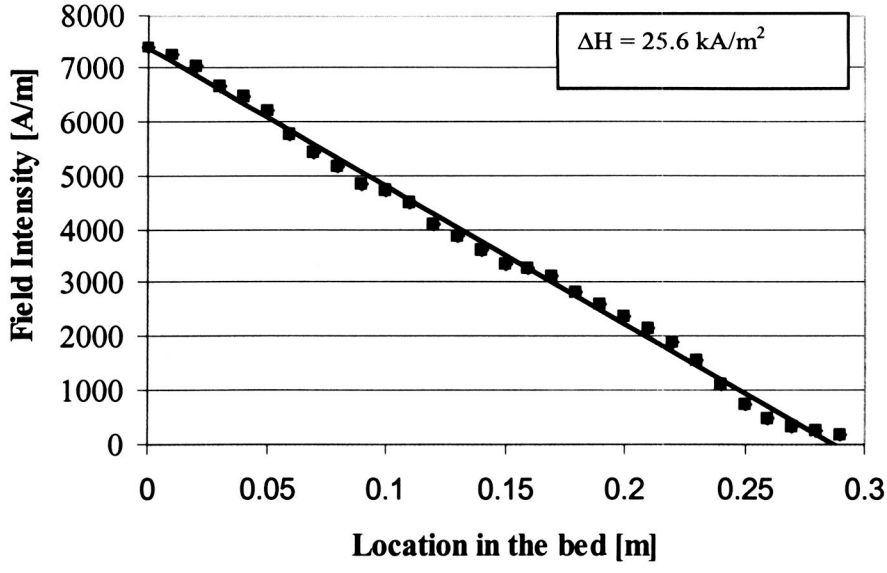

Figure 5.1. Magnetic Field versus Height in Magnetically Consolidated Filter Bed.

Wheat straw particles were first soaked in water and then homogenized in a Waring blender. The suspension was then passed through a series of sieves and only particles with diameters less than 355 μm were used in the filtration experiments. The wheat straw particle size distribution is given for two batches in Table 5.1. Average diameters and specific surface areas are presented in Table 5.2. A photograph of the resulting wheat straw particles is shown in Figure 5.2.

Table 5.1 Wheat Straw Particle Size Distribution.

Diameter [μm]	Batch #1		Batch #2	
	Weight percent [%]	Accumulation [%]	Weight percent [%]	Accumulation [%]
400-300	0.0	100	0.0	100
300-200	9.2	100	8.9	100
200-100	27.3	90.8	24.5	91.1
100-90	2.9	63.5	2.5	66.6
90-80	8.2	60.6	12.7	64.1
80-70	9.0	52.4	3.5	51.4
70-60	9.2	43.4	15.8	47.9
60-50	13.5	34.2	7.4	32.1
50-40	9.2	20.7	14.1	24.7
40-30	6.6	11.5	7.3	10.6
30-20	4.1	4.9	2.7	3.3
20-10	0.3	0.8	0.5	0.6
10-0	0.5	0.5	0.1	0.1

Table 5.2. The Median Size, Standard Deviation, and Specific Surface Area.

Batch	Median Diameter [μ m]	Standard Deviation [μ m]	Specific Surface Area [m^2/g]
1	77.33	68.15	0.089
2	76.00	66.78	0.087

Figure 5.2. Photomicrograph of Comminuted Wheat Straw Particles.

A series of filtration experiments was conducted using a fixed magnetic field gradient of 25.6 kA/m and flow velocities varying between 0.87 and 1.35 cm/s. The experimental results are shown in Figure 5.3. Two similar sets of experiments were also performed at constant flow velocity and variable magnetic field strengths. Results for these filtration experiments are presented in Figures 5.4 and 5.5. From these results we concluded that at a given magnetic field intensity and gradient, the efficiency of the filtration bed increases as the fluid superficial velocity decreases. Also, for a given superficial fluid velocity, the performance of the bed increases as the magnetic field intensity increases.

These experiments show that the efficiency of the filtration operation is increased at the higher magnetic field intensities and higher field gradients while maintaining a constant flow rate. This may be explained by the fact that at the higher magnetic field intensities, the ferromagnetic particles provide a lower

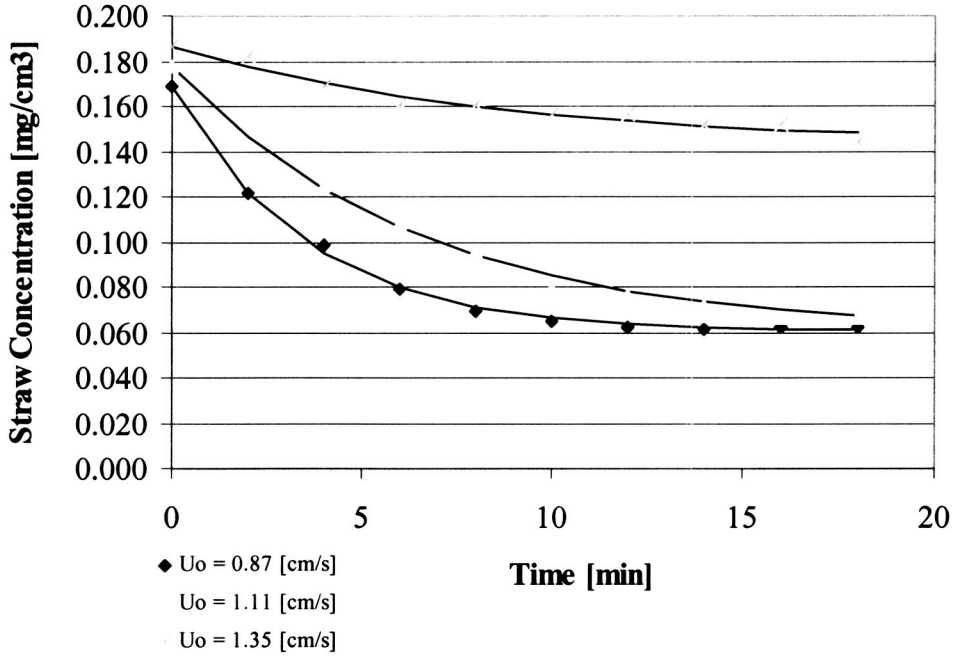

Figure 5.3. Magnetically Assisted Filtration - Constant Magnetic Field and Variable Flow.

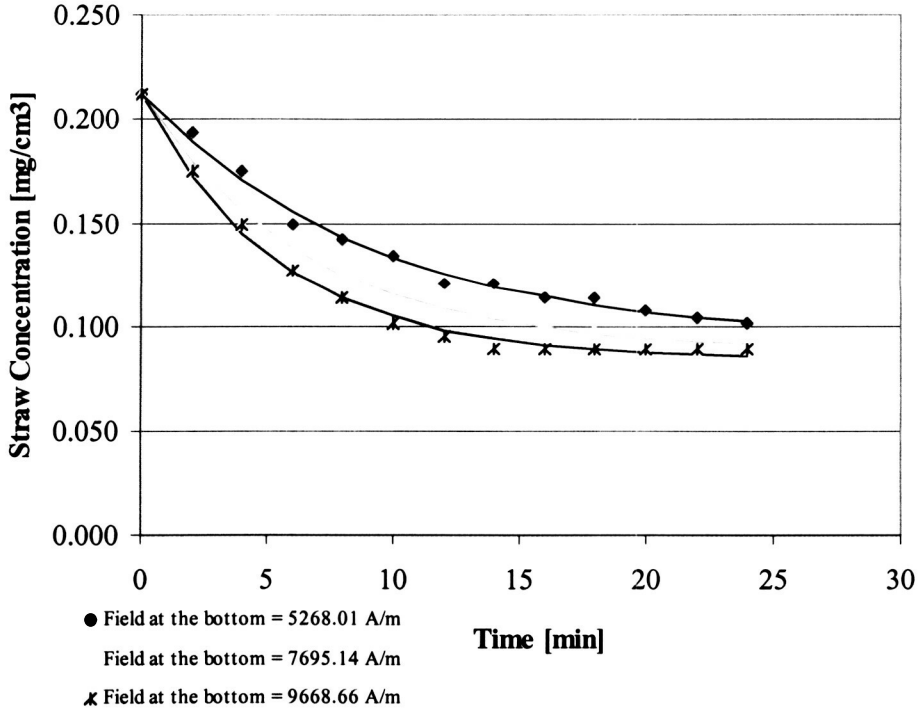

Figure 5.4. Magnetically Assisted Filtration - Constant Flow, U_o = 1.70 [cm/s], Variable Magnetic Field.

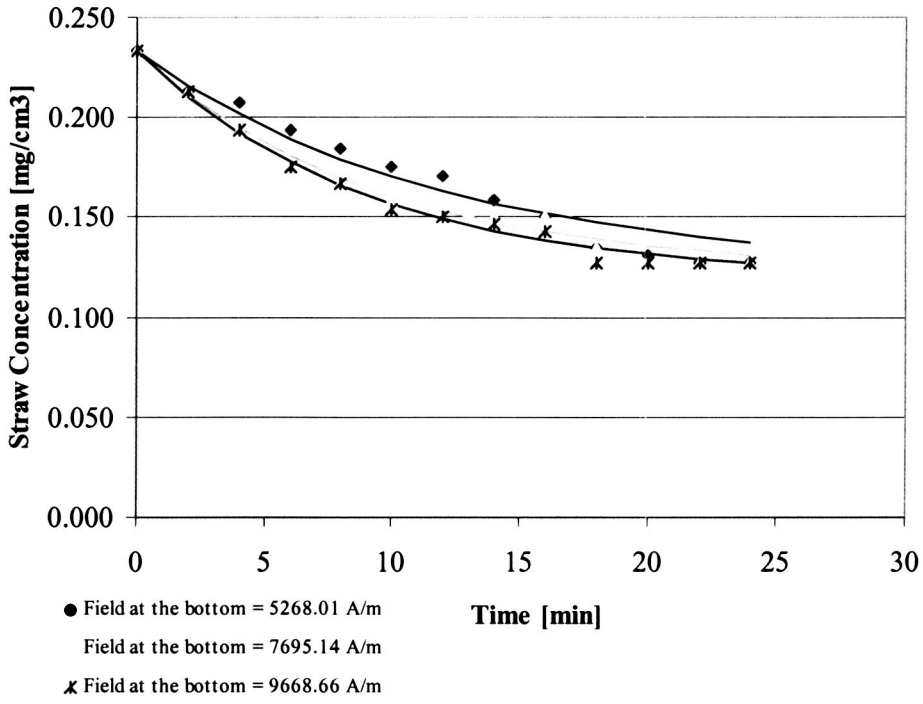

Figure 5.5. Magnetically Assisted Filtration - Constant Flow, U_o = 2.14 [cm/s], Variable Magnetic Field.

degree of voidage within the filter bed, therefore, the contacting points between particles are more numerous, which results in better filtration efficiency. In these experiments, the concentration of the solid waste particles was substantially decreased during the filtration process (60-85% depending on operating conditions). However, the concentration of solid waste particles remains constant after it reaches the maximum capacity of the bed. Hence, the filtration process can be characterized by the rate of accumulation of waste particles in the bed and the rate of detachment of already filtered particles. When these two rates become equal, the maximum capacity of the bed is reached and the filter bed must be regenerated by Magnetically Assisted Gasification reactions.

The results of the filtration experiments were fitted to filtration model presented in Section 4.3 to determine numerical values for the accumulation and the detachment coefficients. These two parameters are related to several mechanisms involved in the deposition of straw particles onto the surface of the magnetic beads, including: diffusion deposition, direct interception, and inertial

deposition. Therefore, both coefficients are expected to vary as a function of hydrodynamic and geometric parameters of the filter system such as magnetic bead size, average straw particle size, velocity of fluid, and bed voidage. Values of k_1 and k_2 derived from the fixed field gradient, variable flow velocity experiments are summarized in Table 6.3

Table 5.3 Values of Accumulation Coefficient (k_1) and Detachment Coefficient (k_2) for Variable Flow Rate, Constant Field Gradient Experiments, $\frac{\partial H}{\partial z} = 25{,}629$ A/m^2.

Fluid Velocity [cm/s]	Initial Concentration [mg/cm^3]	$k_1 \left[\frac{m^3 \text{ liquid}}{m^2 \text{surface} \cdot s}\right]$	$k_2 \left[\frac{1}{s}\right]$
0.87	0.356	1.704×10^{-4}	1.199×10^{-1}
0.87	0.169	6.238×10^{-3}	6.143×10^{-1}
1.11	0.179	5.428×10^{-5}	8.217×10^{-2}
1.35	0.187	1.188×10^{-5}	9.620×10^{-2}

6. MAGNETICALLY ASSISTED FLUIDIZATION.

Fluidized bed contacting is a very effective method for conducting gas-solid and liquid-solid reactions, particularly those which are limited by mass transfer rates[34,53]. In fluidization, a dynamic balance is produced between drag, buoyancy, and gravitational forces, as shown in Figure 1. Maximum gas or liquid flow rates within fluidized bed reactors are limited by the fluid properties and also by the size and density distributions of the granular fluidization media. For a given system, higher rates of mass transfer can be achieved using Magnetically Stabilized Fluidized Bed (MSFB) methods which were pioneered by Rosensweig and coworkers[54-59]. In MSFB technology, magnetically susceptible solids are fluidized within a uniform magnetic field. Here the magnetic forces between the particles augment the apparent size of the fluidization particles and thereby allow higher fluid flow rates under equivalent fluidization conditions. However the homogeneous magnetic field and resulting magnetic interparticle forces do not enable use of this technology in microgravity. In recent years, fluidization phenomena and practical applications of MSFB processes have been extensively studied[60-76]. This has become a rich area of research for the team led by Goran N. Jovanovic at OSU[77-90].

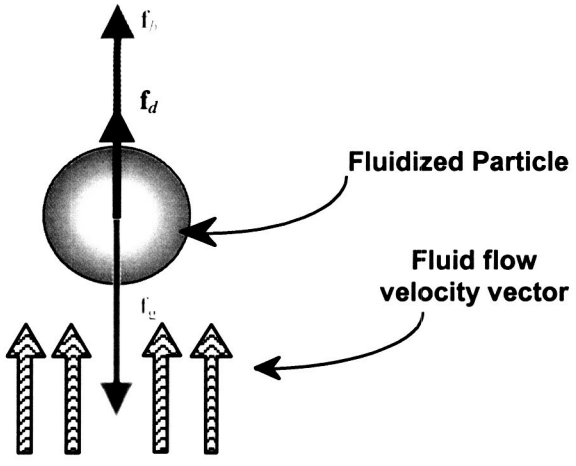

Figure 6.1 Balance of forces acting on a fluidized particle in a conventional fluidized bed.

In MSFB systems, the externally applied magnetic field intensity in the column is uniform. Ferromagnetic particles are magnetized, resulting in a variety of attractive and repulsive interparticle forces (**F**),

$$\mathbf{F} = \frac{\mu}{4\pi} \frac{p_1 p_2}{r^2} \hat{\mathbf{i}}$$

where p_1 and p_2 are the pole strengths of respective particles and r is the distance between them (Figure 6.2). In MSFB systems, these are the only magnetic forces produced. Neither MSFB nor conventional fluidized beds can operate in microgravity, because of the absence of a countervailing force to moderate the drag forces which the fluid exerts on the particles.

However, in our research the ability to achieve controlled fluidization in microgravity has been established using Gradient Magnetically Assisted Fluidized Bed (GMAFB) methods which utilize additional forces produced by a magnetic field gradient,

$$\mathbf{F} = \nabla(\mathbf{M} \cdot \mathbf{B})$$

where **M** and **B** are magnetization and flux density vectors, respectively.

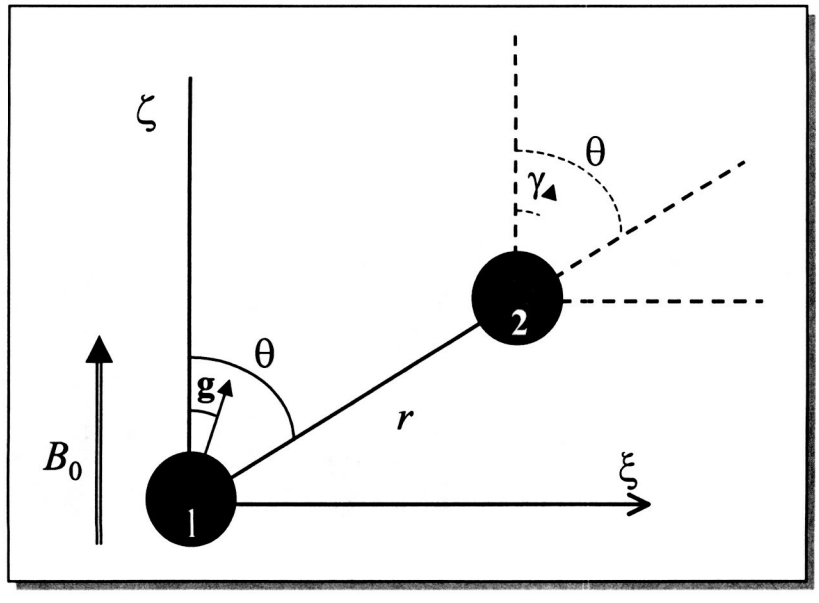

Figure 6.2. Magnetic Interparticle Forces in MSFB.

Employment of these additional forces produced by the magnetic field gradient makes possible a much higher degree of control of fluidization (or conversely consolidation) of granular ferromagnetic media and enables microgravity and hypogravity operation. In Figure 6.3, the forces acting upon a ferromagnetic particle in microgravity are illustrated, both in the presence and absence of a magnetic field gradient. A comparison of the magnetic fields which are employed and the corresponding forces produced by MSFB (homogeneous field) and GMAFB (field gradient) methods is shown in Figure 6.4.

Using the constant gradient electromagnets and ferromagnetic materials discussed in previous sections, gradient magnetically assisted fluidized bed operations have been conducted in the laboratory under normal gravitational conditions and in microgravity aboard NASA's KC-135. These experiments are described in the following sections.

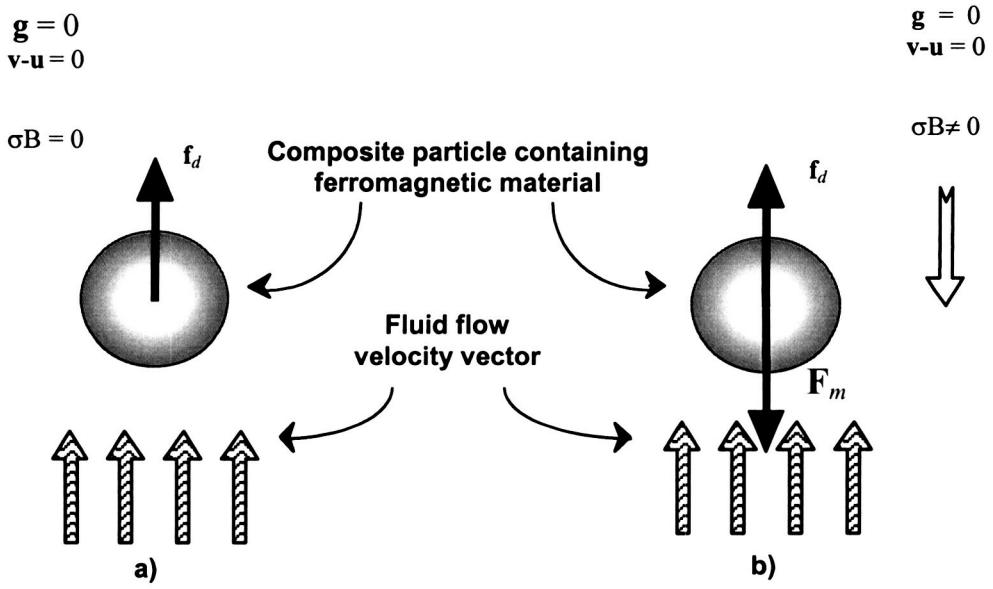

Figure 6.2 Balance of Forces Acting on a Fluidized Magnetically Susceptible Particle Placed in, **a)** an Unsustainable Fluidized Bed in the Absence of Gravity, and **b)** a Gradient Magnetically Assisted Fluidized Bed in the Absence of Gravity.

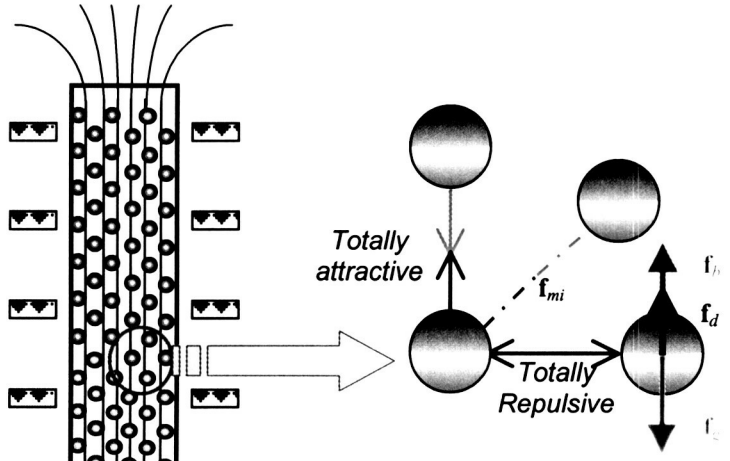

a) In a uniform magnetic field, there is no magnetic body force. However, inter-particle magnetic attraction and repulsion exists. Particle shades represent magnetization.

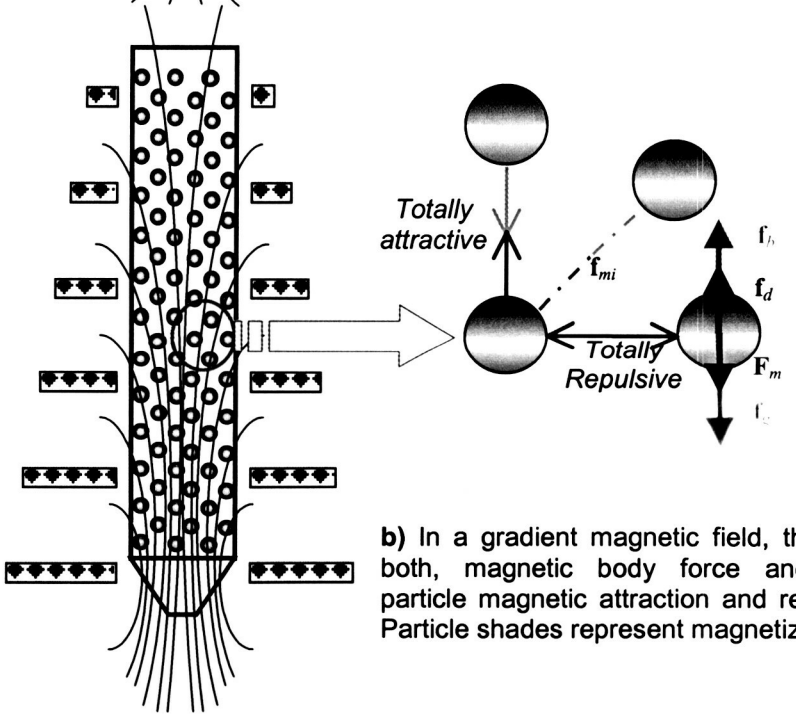

b) In a gradient magnetic field, there are both, magnetic body force and inter-particle magnetic attraction and repulsion. Particle shades represent magnetization.

Figure 6.4 Schematic Representations of Body and Interparticle Magnetic Forces in **a)** Uniform Magnetic Field, and **b)** Gradient Magnetic Field.

6.1 Laboratory GMAFB Fluidization Experiments. The test apparatus used in the 1g laboratory experiments is illustrated schematically in Figure 6.5. These experiments employed ferrite impregnated calcium alginate beads as the ferromagnetic fluidization media. A series of Helmholtz coils were incorporated into the system which produces a nearly constant magnetic field gradient along the height of the fluidized bed. Cylindrical and rectangular magnetic fluidization columns are illustrated in Figure 6.6. In these experiments, a recirculating water stream was fed through a distributor plate at the bottom of the fluidization column and the degree of fluidization (voidage) at various locations within the column was determined via an array of pressure transducers. A variety of experiments were conducted under varying conditions of magnetic field gradient and superficial flow velocity. In general, good agreement was obtained between the predictions from the VDM model and the experimental observations, with the most significant

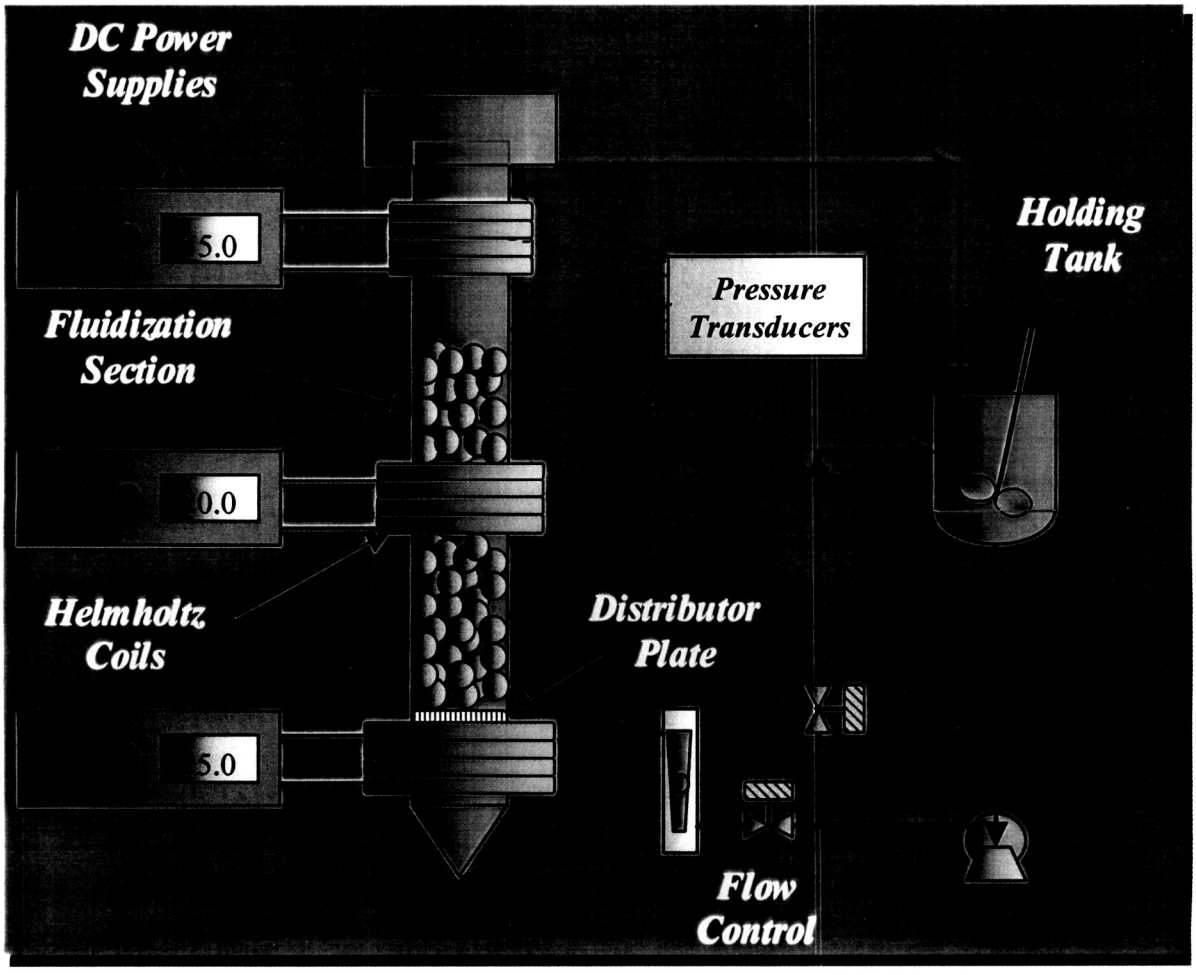

Figure 6.5 Laboratory Gradient Magnetically Assisted Fluidization Apparatus.

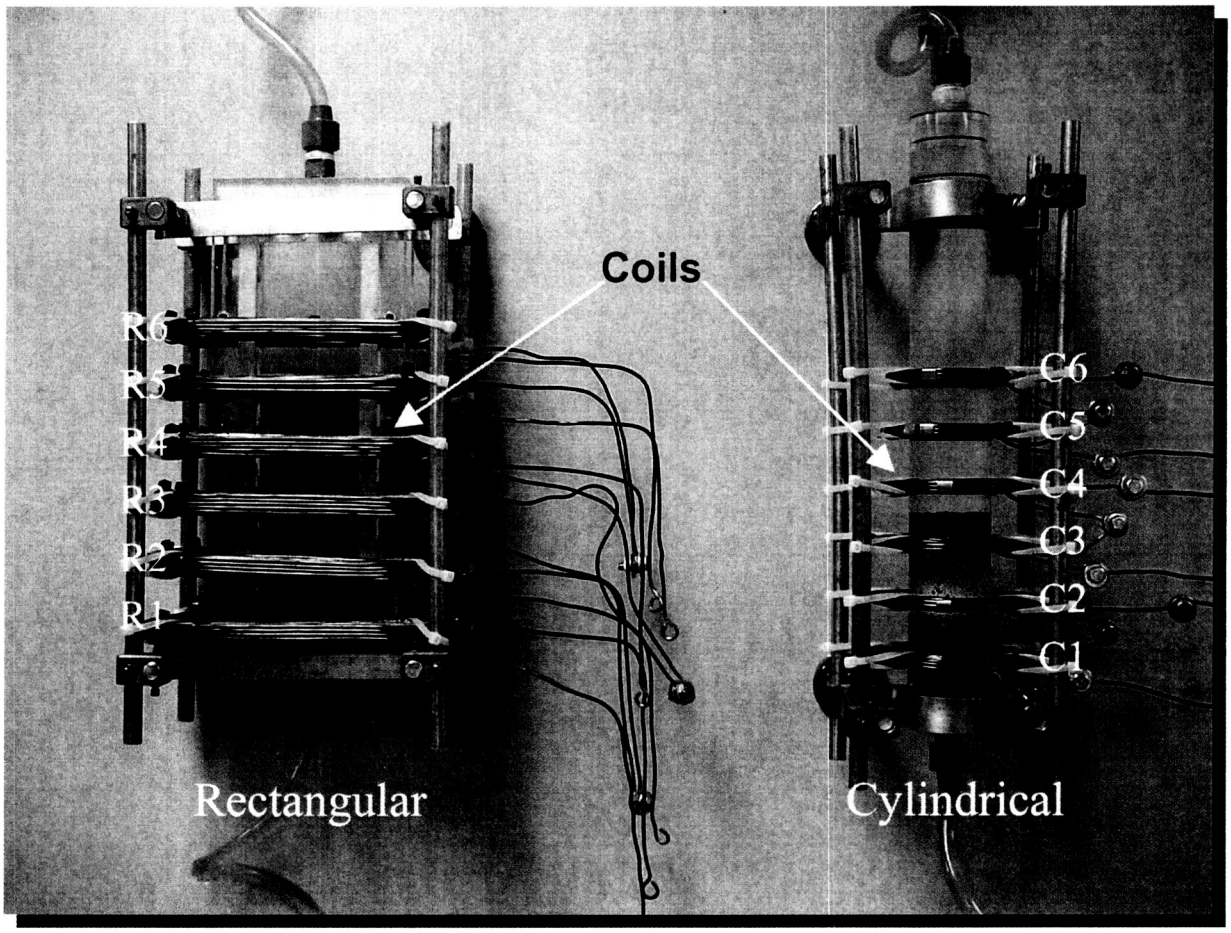

Figure 6.6 Photographs of Cylindrical and Rectangular Gradient Magnetically Assisted Fluidization Columns.

deviations occurring near the bottom and top of the bed. The results for two typical experiments are presented in Figures 6.7 and 6.8. Figure 6.7 corresponds to an experiment conducted under a magnetic field gradient of -14,663 A/m^2 and a superficial fluid velocity of 0.0176 m/s. The experimental results presented in Figure 6.8 correspond to a magnetic field gradient of -20,543 A/m^2 and a superficial fluid velocity of 0.0222 m/s. Fluidization of the magnetic media produced bed heights of 0.250 and 0.217 m, respectively. Under these conditions, the magnetic forces augment the gravitational forces, allowing substantially higher flow rates to produce a given degree of fluidization. The primary benefit of this capability in the terrestrial environment is the potential for much higher rates of mass transfer in fluidized bed reactors than would otherwise be possible. In microgravity, these additional forces make fluidization possible.

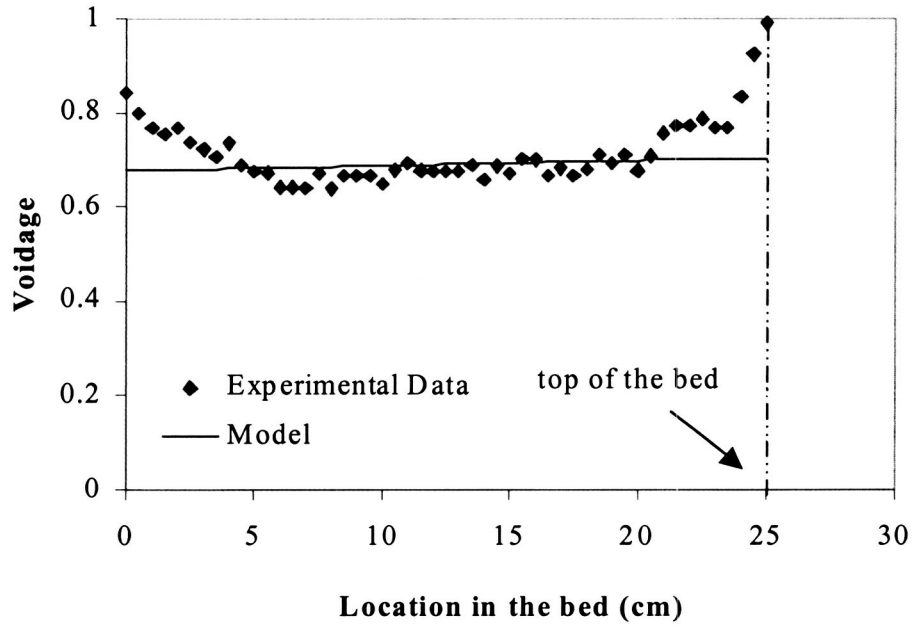

Figure 6.7. Lab Fluidization Experiment- $\nabla H = -14.663$ A/m^2, $U_o = 0.0176$ m/s.

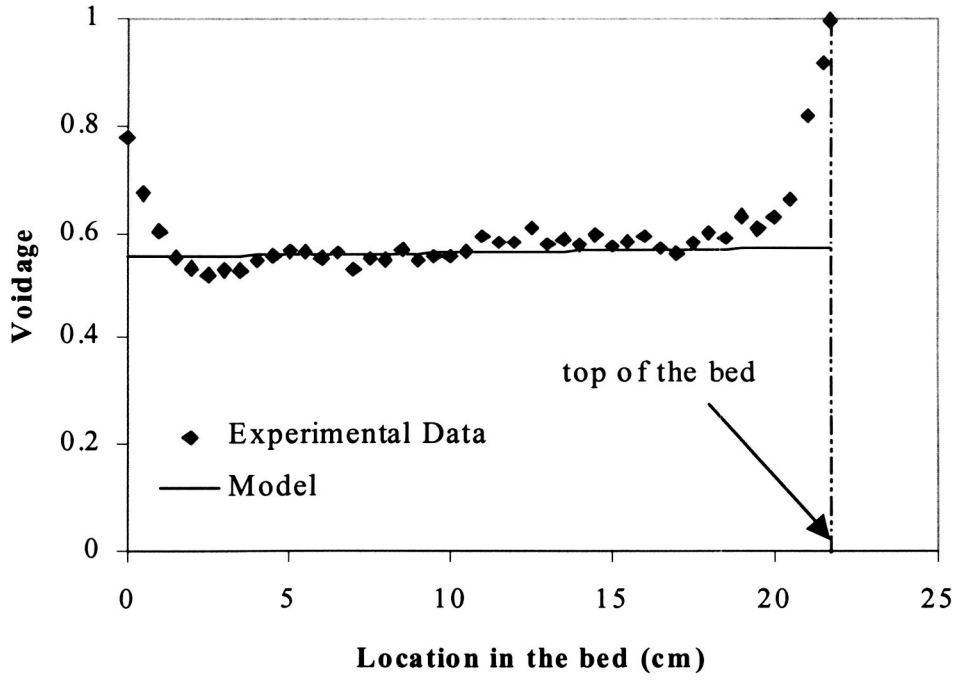

Figure 6.8. Lab Fluidization Experiment- $\nabla H = -20{,}543$ A/m^2, $U_o = 0.0222$ m/s.

6.2 Microgravity Fluidization Experiments. The first Flight Experiments were conducted onboard NASA's KC-135 during the Spring of 2000 (Figure 6.9). In these experiments, magnetically assisted fluidization was monitored under microgravity conditions as a function of superficial flow velocity. The experimental apparatus is shown aboard the aircraft in Figure 6.10, and illustrated schematically in Figure 6.11. Ferrite impregnated calcium alginate beads were employed as the ferromagnetic media. Experiments were performed by recirculating water through the magnetic media housed within a quasi-two dimensional V-shaped bed. The V-shape provides for a variable cross sectional area and thus results in variable superficial flow velocities as a function of height for a given flow rate. A close-up photograph of the two dimensional fluidized bed is shown in Figure 6.12. During the flight experiments, both the magnetic field intensity and the magnetic field gradient were held constant. The total height of the bed was measured under conditions of variable flow rate and superficial flow velocity under microgravity. The generally good agreement between the experimental observations and the bed height predictions of the VDM model are illustrated in Figure 6.13. This was the first demonstration of fluidization in microgravity.

Figure 6.9. First Microgravity Flight Experiments Performed during the Spring of 2000.

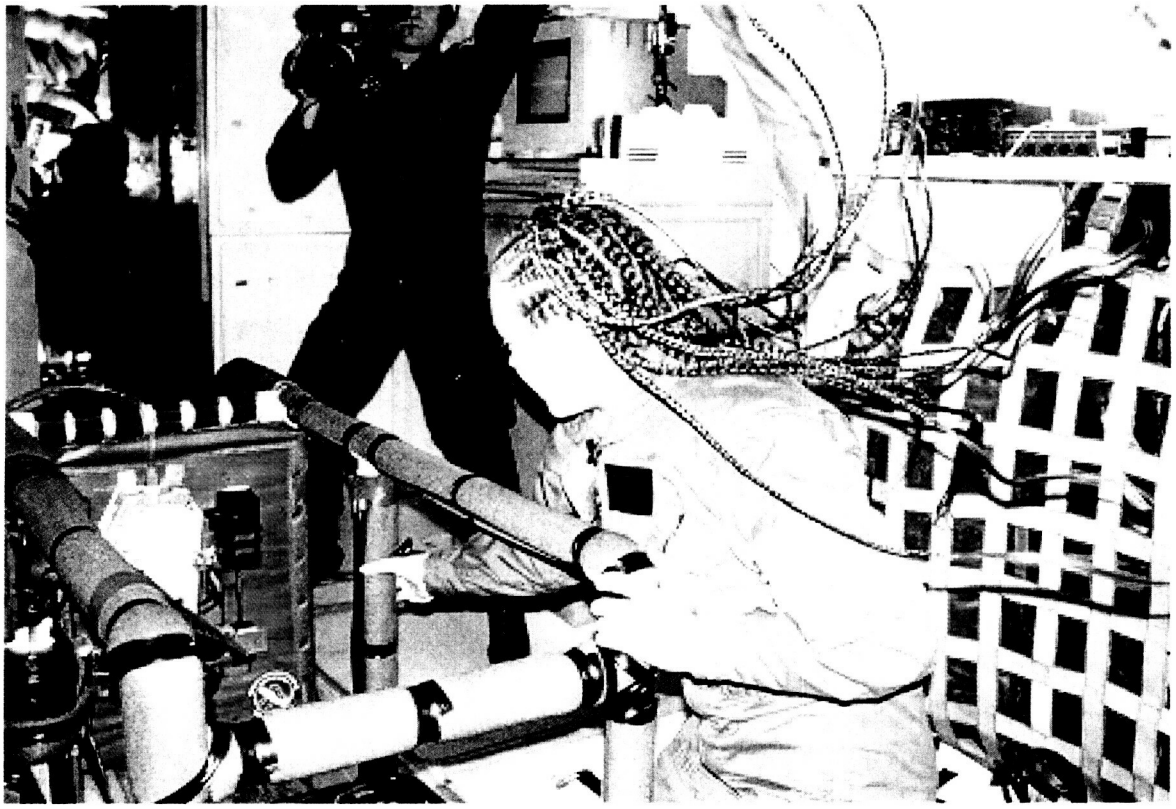

Figure 6.10. Magnetically Assisted Fluidization Microgravity Flight Experiment in Progress. First Microgravity Demonstration of Fluidization Phenomena.

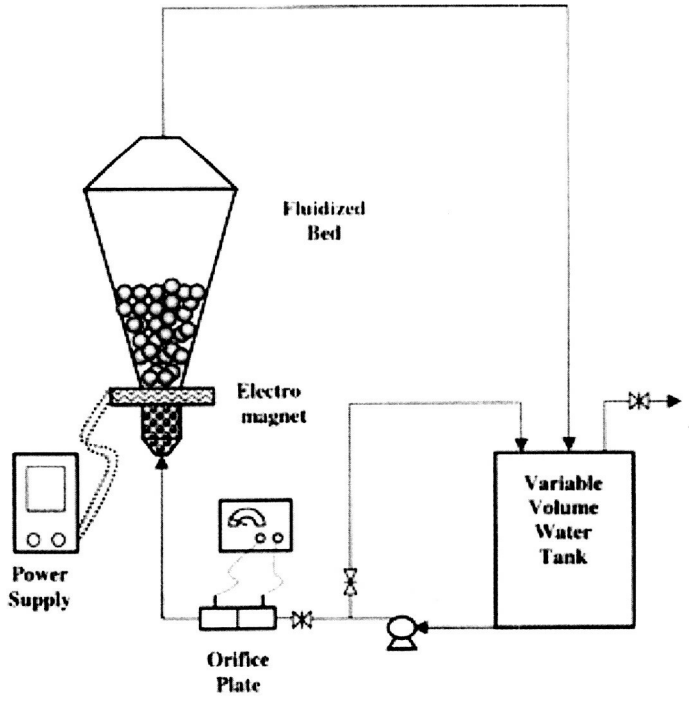

Figure 6.11. Flight Experiment Flow Schematic.

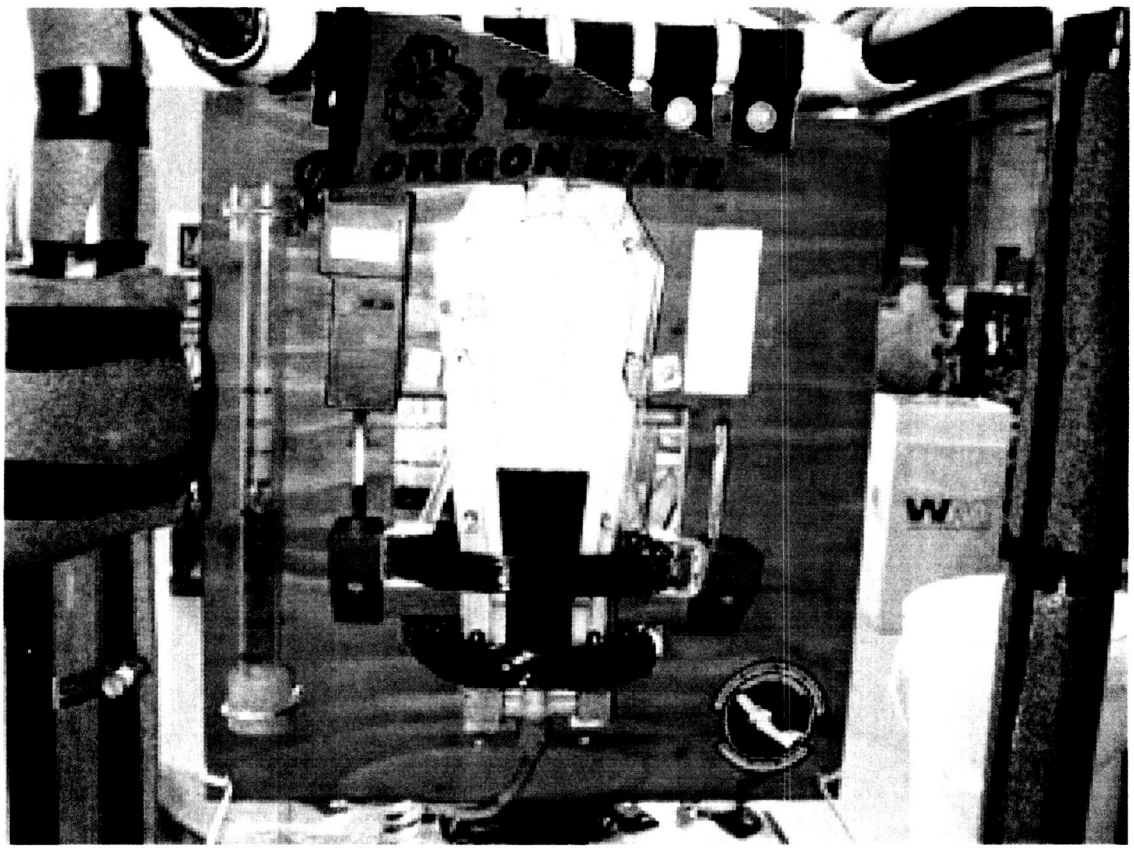

Figure 6.12. V-Shaped 2-D Fluidization Chamber with Helmholtz Coils.

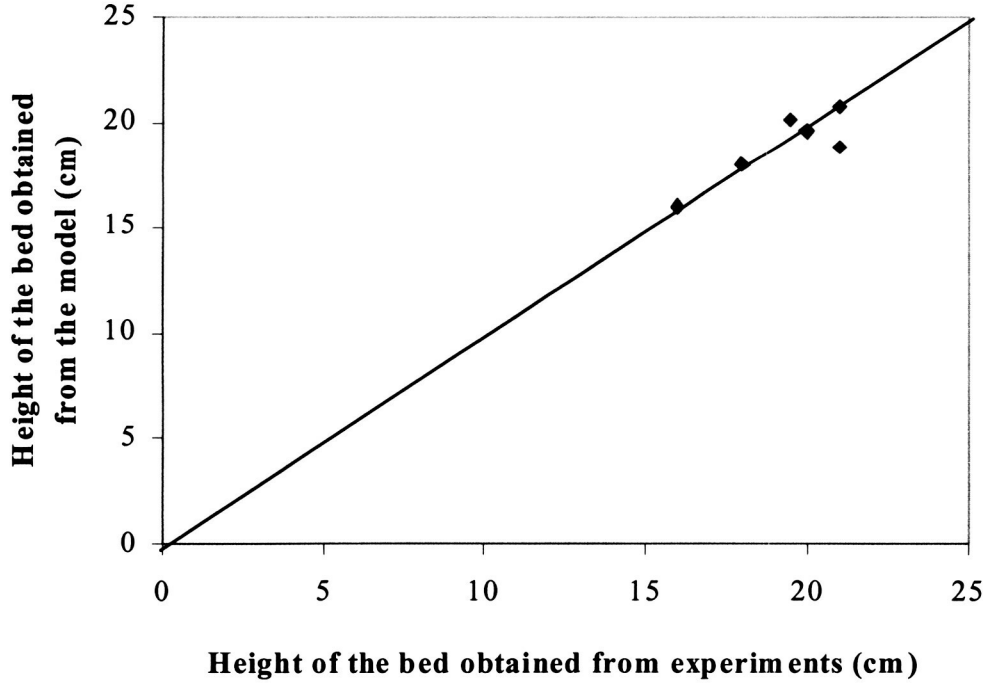

Figure 6.13. Correlation of Experimental and VDM Model Predictions for Magnetically Assisted Fluidization in Microgravity.

A second series of flight experiments was conducted aboard NASA's KC-135 in the Spring of 2001 to further investigate magnetic enabling of fluidized beds in microgravity. The apparatus was modified to incorporate three electromagnet coils which produced a nearly constant magnetic field gradient. Photographs of the fluidization section and the full apparatus taken in the hanger at Ellington Field, are shown in Figures 6.14 and 6.15, respectively. As in the previous year, a two-dimensional, rectangular cross-sectioned, and tapered fluidization column was used. The Plexiglas housing allowed direct visual observation of the fluidized bed. The fluidization column was divided into two main sections: the calming section at the bottom, followed by the fluidization section. The calming section was composed of small marbles enclosed under the distributor plate, providing a uniform upward flow to the fluidization section. The distributor plate was located between the calming section and the fluidization section, and was fabricated from

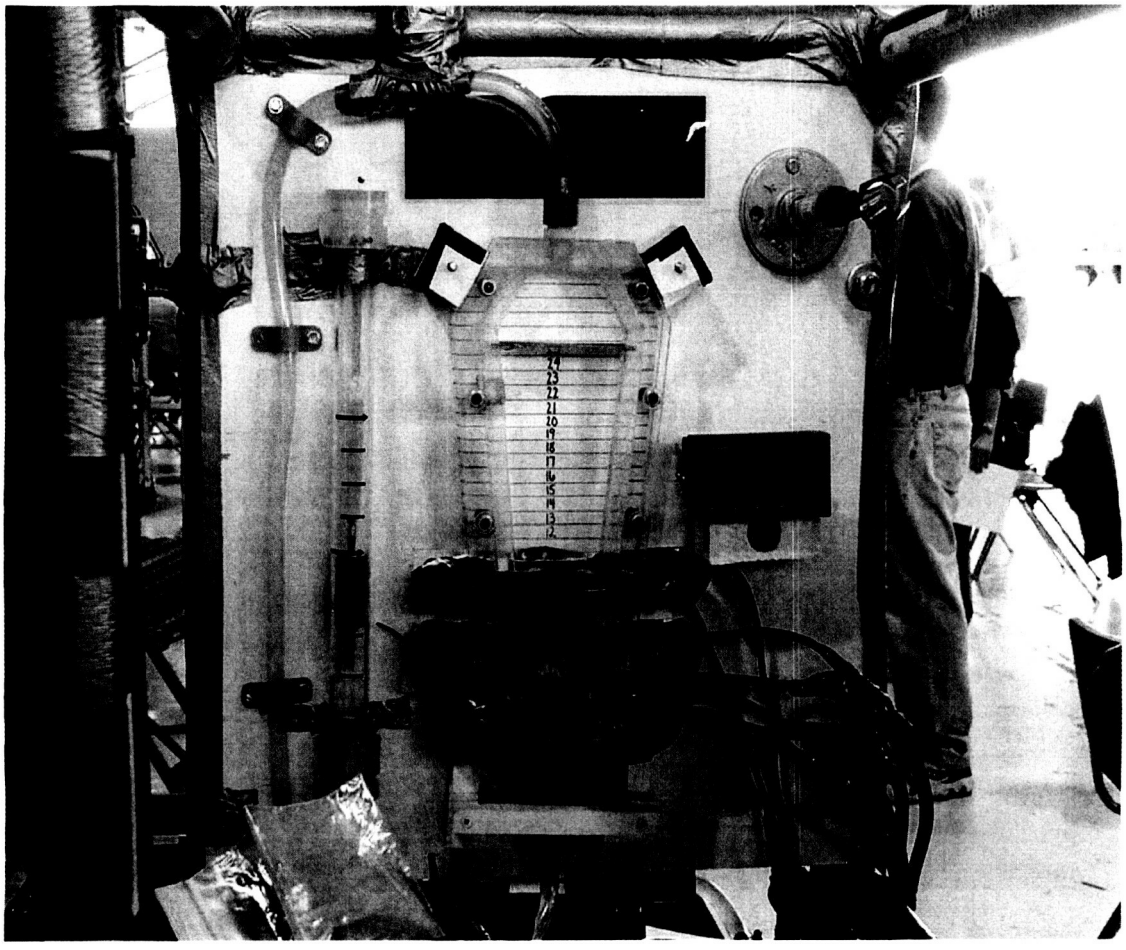

Figure 6.14. Microgravity Fluidization Column with Three Helmholtz Coils.

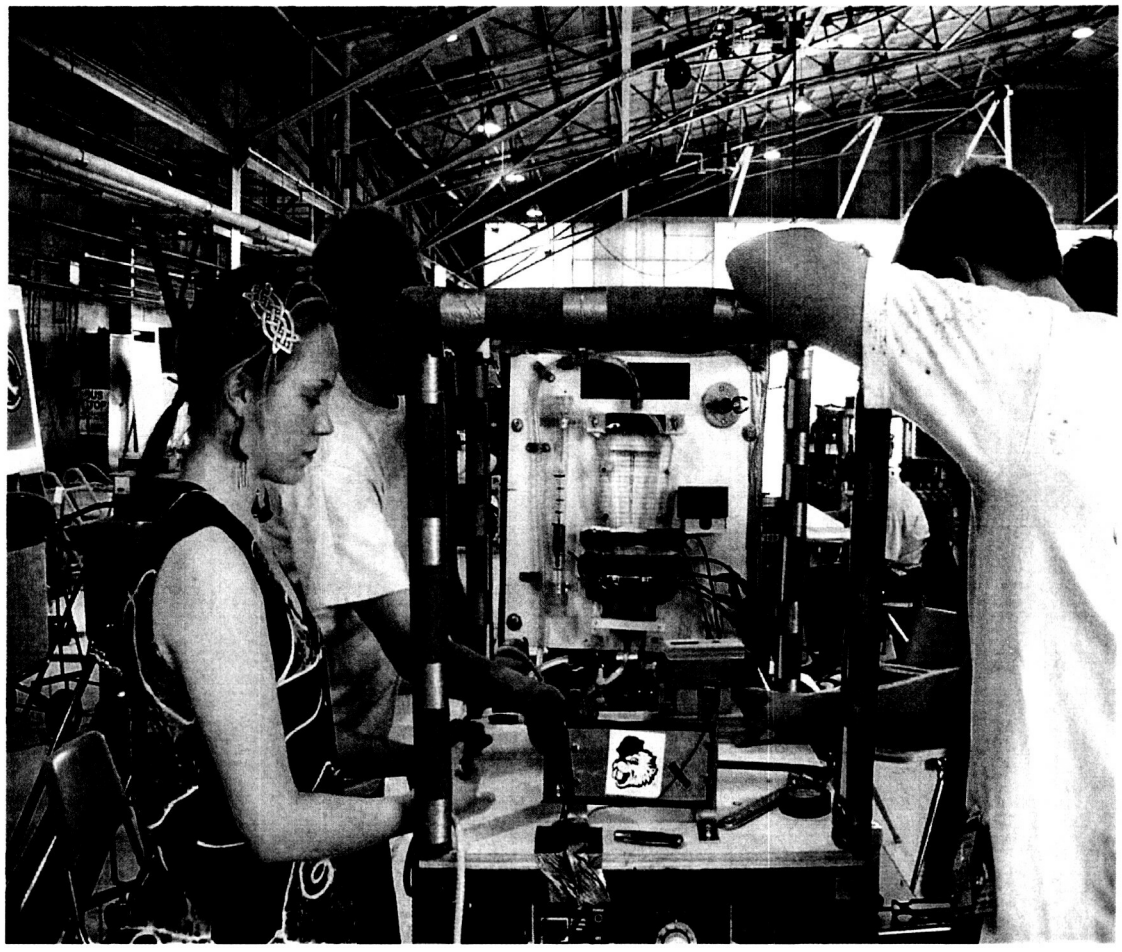

Figure 6.15. Microgravity Magnetically Assisted Fluidization Experimental Apparatus – Second Series of Flight Experiments.

the same material as the fluidization column, with circular holes uniformly distributed throughout the plate. The water supply system consisted of a pump driven by a 1/3 Horsepower, 2600/3000-rpm motor. The pump discharge was connected to a flow meter and directed to the fluidization column. The fluid flow was regulated by a valve mounted upstream of the flow meter. The generalized layout of the complete test stand is presented in Figure 6.16.

Eleven experiments were performed on board the KC-135. These experiments were designed based on the experimental results obtained during similar flights in the previous year. Modifications were made in the construction of the bed, the design of the magnetic field, and composition of the fluidization

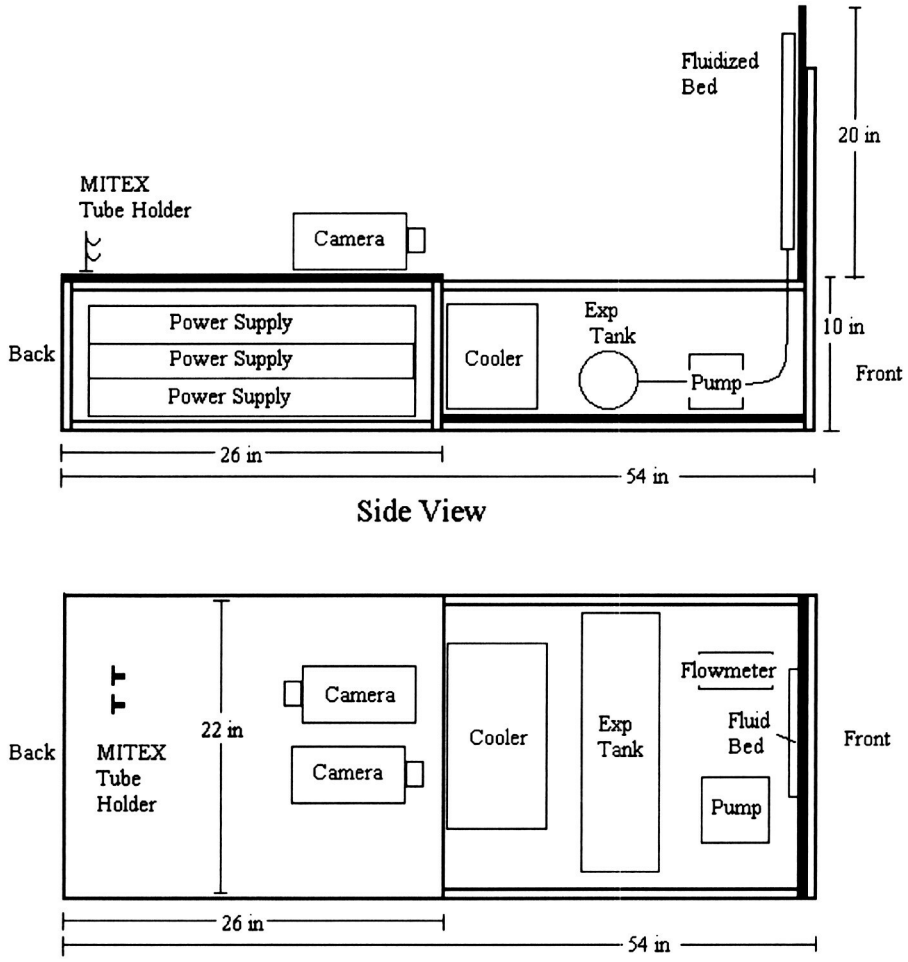

Figure 6.16. General Layout of Microgravity Flight Experimental Apparatus.

particles. Two types of ferromagnetic media, ferrite containing polymer composite particles (30% ferrite) and porous metallic cobalt spheres, were fluidized in the V-shaped quasi-two-dimensional fluidization column over a range of magnetic field intensities and liquid flow rates. These particles were superior in their performance, as compared to the particles employed during the experiments of the previous year. Three modified Helmholtz coils, designed with the aid of the Tesla-I software discussed in Section 3, were used to generate the desired magnetic fields. These were generated in such a way that the magnetic field gradient was maintained constant throughout the axial length of the fluidization column. Intensity of the magnetic field was highest at the bottom of the bed and decreased linearly toward the top of the bed. Therefore, the direction of magnetic force was oriented toward the distributor plate, opposite to the flow of water. Both, the magnetic field intensity and field gradient used in the experiments were

predetermined and tested in the laboratory before the flight experiments. The volumetric flow rate in each experiment was measured by the turbine flow rate sensor, and was displayed on the panel next to the fluidized column. The height of the bed, at any given field intensity and liquid flow rate, was simultaneously recorded on video tape. Each individual experiment consisted of presetting a specific flow rate and magnetic field intensity, and then measuring the height which the bed expanded to under microgravity. Examples of experiments with cobalt and ferrite media are shown in Figures 6.17 and 6.18, respectively. The experimental results are summarized in Table 6.1. These experiments confirmed that:

(i) without the magnetic field surrounding the fluidization column, particles are swept away immediately in the direction of the flow when zero-g acceleration is reached;

(ii) at a given magnetic field intensity, the height of the stable fluidized bed increases as the superficial fluid velocity increases;

Table 6.1. Summary of the Experimental Results for Second Series of KC-135 Microgravity Flights.

Particles	Volumetric flow rate (mL/sec)	H_z at the bottom (A/m)	Initial Bed Height (m)	Final Bed Height (m)
Ferrite	7.5	0	0.11	Expanded to the top of the bed
Ferrite	7.0	2411.2	0.11	0.180
Ferrite	7.0	4742.8	0.11	0.155
Ferrite	7.0	7034.6	0.11	0.148
Ferrite	14.0	2411.2	0.11	Expanded to the top of the bed
Ferrite	14.0	4742.8	0.11	Expanded to the top of the bed
Ferrite	14.0	7034.6	0.11	Expanded to the top of the bed
Cobalt	6.4	4742.8	0.11	0.135
Cobalt	11.5	4742.8	0.11	0.170
Cobalt	12.7	1893.9	0.11	Expanded to the top of the bed
Cobalt	46.5	0	0.11	Expanded to the top of the bed

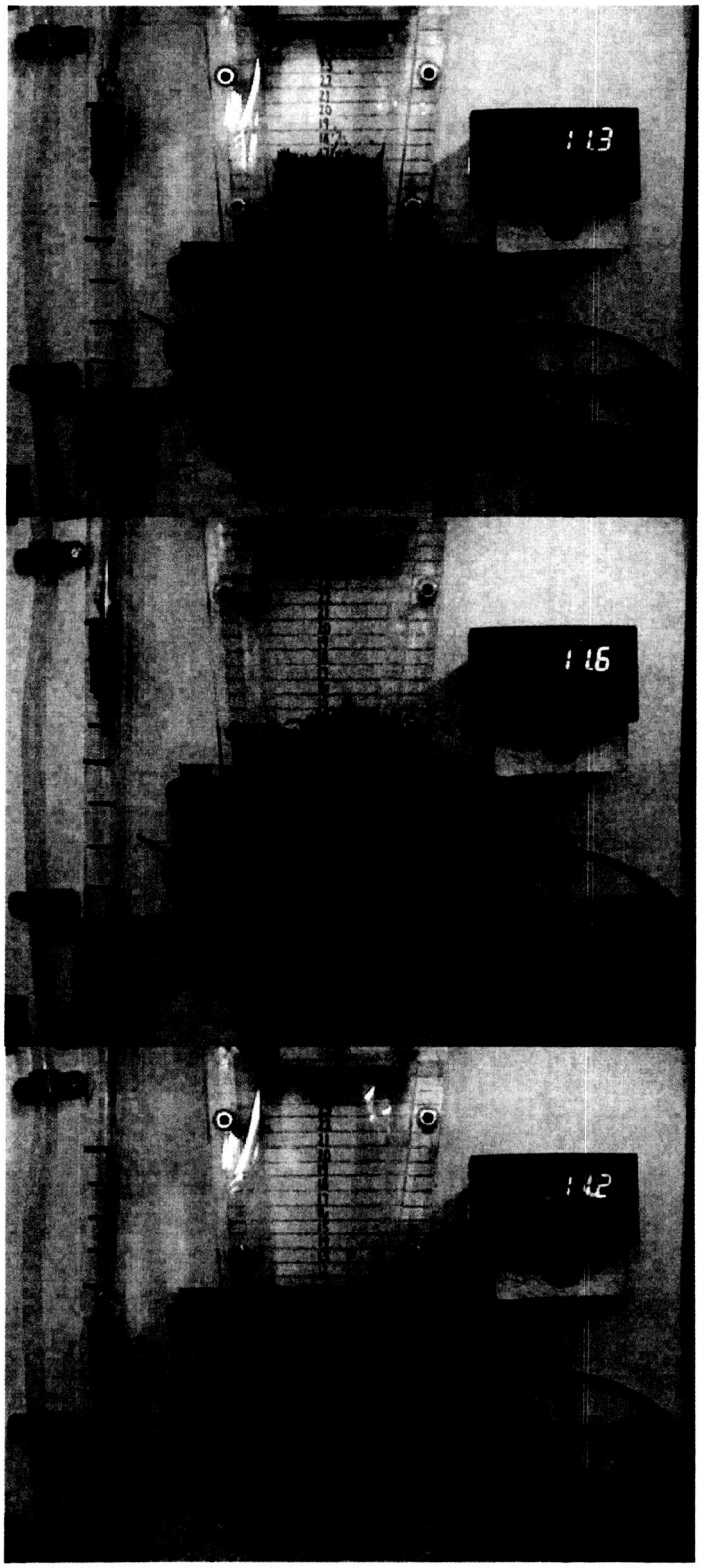

Figure 6.17. GMAFB 0g-Flight Experiment – Cobalt Media: Bottom – Bed Consolidated under 1 g, Middle - 0g Bed Begins to Expand under Liquid Flow, Top - 0g Fluidized Bed Stabilizes at Maximum Expansion Level under Magnetic Control.

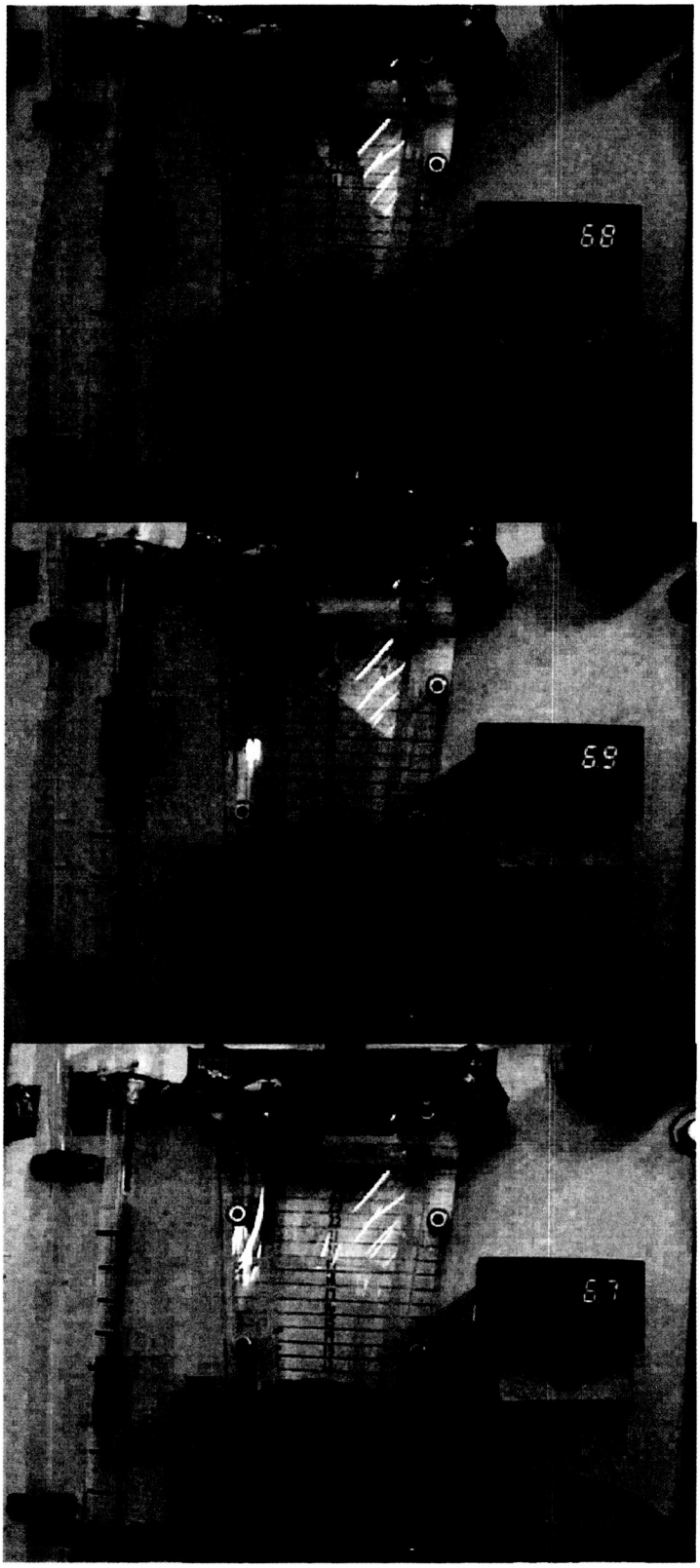

Figure 6.18. GMAFB 0g-Flight Experiment- Ferrite Media: Bottom – Bed Consolidated under 1 g, Middle - 0g Bed Begins to Expand under Liquid Flow, Top - 0g Fluidized Bed Stabilizes at Maximum Expansion Level under Magnetic Control.

(iii) at a given superficial fluid velocity, the height of the bed decreases as the magnetic field intensity increases.

While these conclusions generally follow the results obtained from the flight experiments of the previous year, the newly implemented changes in the composition of particles, bed geometry and magnetic field generation, extended significantly the range of operating conditions. Furthermore, new experimental observations showed that there are three distinct operating regions appearing in the magnetically assisted fluidized bed.

[1] The first region is the region adjacent to the distributor plate. The water coming through the distributor plate has a high velocity, and creates small jets above the distributor plate. These jets exchange momentum with the surrounding fluid and particles. As a result, the particles in this region move vigorously with visible vibrations. The length of this zone depends on the magnetic field intensity and the field gradient. This zone is longer at lower magnetic field intensities, and it can diminish or even disappear if the magnetic field intensity is substantially increased.

[2] The second fluidization region is observed when the jets no longer influence the movement of the particles. The particles form a packed bed in this region. This region is established whenever the magnetic forces are stronger than the drag forces acting on the fluidization particles.

[3] The third region is observed at the top (downstream) part of the fluidized bed where conditions for "normal/usual" fluidization exist. In this region, magnetic forces are balanced with other forces to allow particulate fluidization.

These three regimes of magnetically assisted fluidization were observed simultaneously. As a consequence, the distribution of particles can range from tightly consolidated, to loosely packed, to controlled fluidization, all depending on the magnitude of flow rates and magnetic fields used, and the position of the particles relative to the field gradients. The most important impact resulting from these experiments is our increased understanding of the fluidization regimes and the ability to adjust operating conditions so that the desired fluidization regime is maintained in microgravity.

7. SOLID WASTE GASIFICATION.

Three primary reaction schemes were considered for the destruction of solid wastes prior to the design and assembly of MAG hardware: oxidation (combustion)[8-12], pyrolysis[13-24], and steam reforming[91-110]. Gasification by combustion reactions, given sufficient oxidant, results primarily in the formation of CO_2 and water vapor, with NO_x and SO_x occurring as minor constituents. Pyrolysis on the other hand may produce a broad variety of inorganic and organic reaction by-products, depending upon the reaction conditions. Steam reformation, performed at either atmospheric or elevated pressure, involves a multiplicity of reactions, including: oxidations, isomerizations, cleavages and additions, and is known to produce a variety of relatively simple gases such as CO_2, water vapor, CH_4 and H_2. The goal of the reaction engineering effort was to identify the conditions which maximize the conversion of mixed wastes into useful gases, while minimizing the input energy and material requirements, and reducing the complexity of reactor operation. Ideally we wished to achieve 100% conversion of wastes to gases and residual inorganic material (ash). For the purposes of this investigation, reaction by-products were considered as members of five classes: ash, char, tar, water, and gases. Char is residual solid phase carbonaceous material which remains within the reactor upon completion of the gasification reactions. Tar consists of a complex mixture of hydrocarbons which are volatile at reactor temperature, but which condense at room temperature. The formation of char must be eliminated, or at the least, kept to the absolute minimum. The production of tars must also be minimized.

The solid waste gasification test stand is illustrated schematically in Figure 7.1. The apparatus is configured to conduct all three forms of gasification at elevated temperature. To primarily limit solid waste decomposition reactions to pyrolysis, nitrogen (an inert gas) was introduced into the reactor. During combustion (oxidation) operations, both oxygen and nitrogen (or air) were to be employed. For the steam reforming studies, liquid water was injected into the reactor through a section of tubing maintained at 110 °C. In addition to steam, a controlled flow of nitrogen was also injected. This apparatus was initially configured for ambient pressure steam reformation and later modified for pressurized operation.

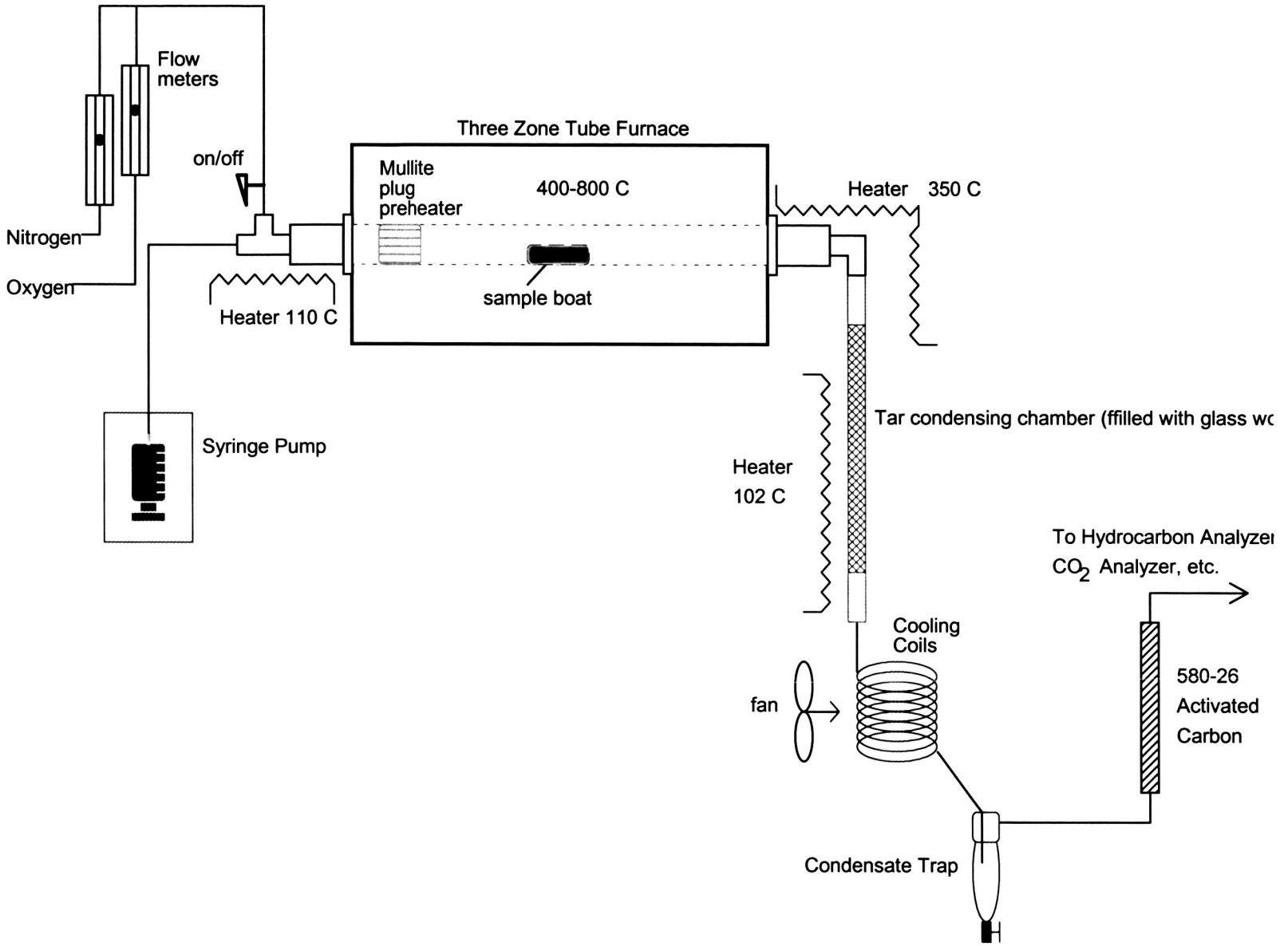

Figure 7.1. Solid Waste Gasification Test Stand.

The test stand was designed so that for each gasification process, the nitrogen flow carries product gases to desired downstream collection points. A 4 ft. (1.22 m) stainless steel tube with a 25.4 mm OD. and 21.2 mm ID. was used as the reactor vessel. This reactor was housed within a 4 ft (1.22 m). three zone tube furnace with an upper temperature limit of 1,500 °C. However, based upon safety concerns, experiments were limited to the range between 400 °C and 800 °C. In operation, gas entering the reactor was preheated by passage through a large pore diameter mullite plug, which provided intimate contact between the gas and the conductive surfaces. The solid waste sample to be gasified was contained within an alumina sample boat positioned at the center of the reactor tube. Gases produced during solid waste decomposition were swept out of the reactor into a section of tubing which was maintained at 350 °C to prevent the condensation of tars. The product gasses then entered a tar collection trap maintained at 102 °C. The first ~50 mm of this tar trap was maintained at 350 °C to ensure that all tar was collected inside the trap and none remained adsorbed onto the upstream fittings. This allowed tar production to be quantified by weight difference of the tar trap before and after each experiment. The tar trap was maintained at a temperature above 100 °C to prevent the condensation of water in this section. Immediately upon leaving the tar trap, the product gases entered a set of water condensing coils. These coils also collected the sub-fraction of tar which condenses between 102 °C and room temperature. This component represents a small fraction of the water mass collected and, as such, was not taken into account. Condensate was then captured in a separatory funnel, and the volume of liquid water was measured after each experiment. Gas production was determined from the difference between the initial weight and the summed weight of all ash, char, tar and water recovered.

Preliminary pyrolysis and steam reforming experiments were performed using both wheat straw and tissue paper samples, to facilitate design of the test stand and to identify proper means for the collection of the by-product fractions. Since pyrolysis involves the thermally induced decomposition of organic materials, initial thermogravimetric analyses (TGA) were performed under nitrogen for tissue paper and wheat straw to characterize the relationship between temperature and gasification via pyrolytic mechanisms. TGA runs were performed over a range of heating rates between 15°C/min to 90°C/min. The experimental results are shown for wheat straw and tissue paper in Figures 7.2 and 7.3, respectively. Based upon

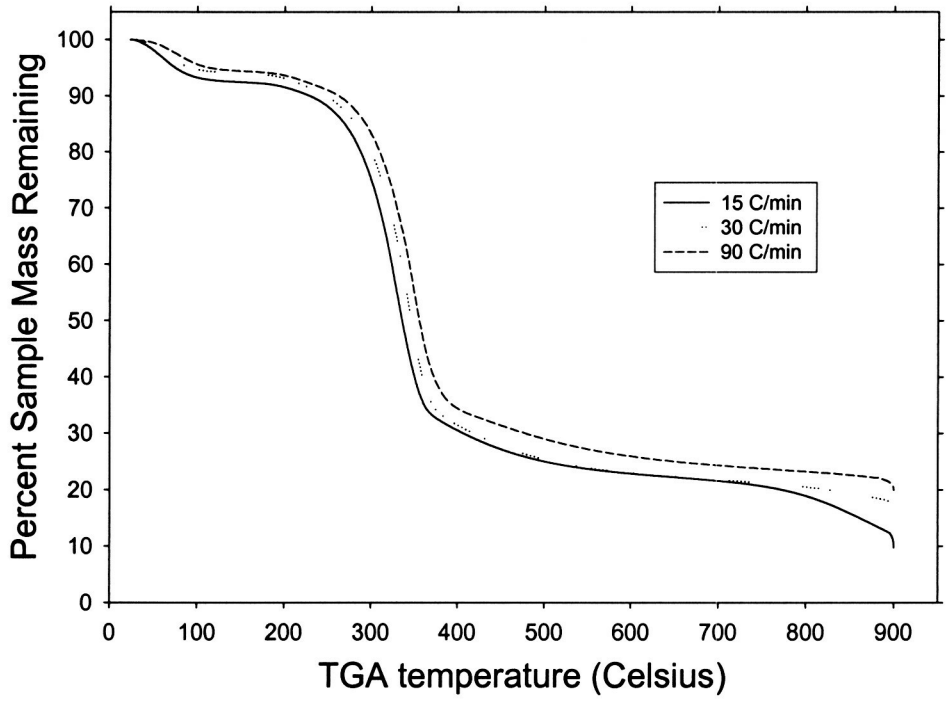

Figure 7.2. Thermogravimetric Analysis of Wheat Straw Pyrolysis.

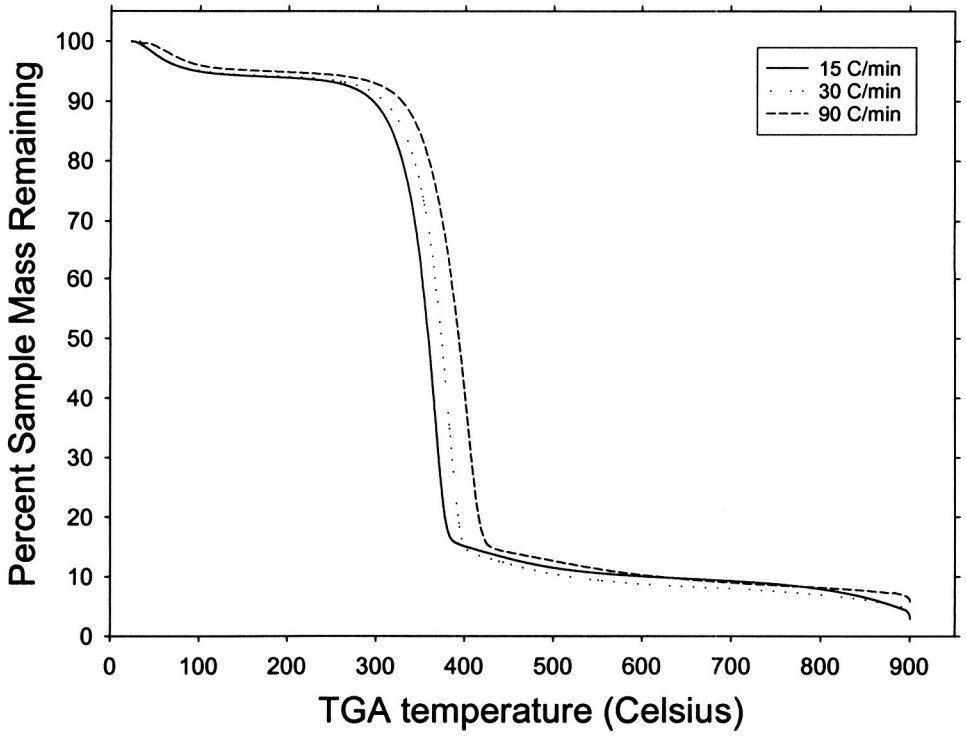

Figure 7.3. Thermogravimetric Analysis of Tissue Paper Pyrolysis.

these results, it was concluded that partial gasification via pyrolysis can be conducted over a broad range of heating rates. However, a significant char residual remains even after pyrolysis at temperatures above 800°C. While the residual char may be decomposed by prolonged treatment at high temperatures, this makes pyrolysis unattractive from both energetics and safety standpoints.

Due to time constraints driven by the need to fabricate hardware in the third year of this grant, no combustion experiments were performed. Combustion is a process which has been well studied by other research groups. It is known that complete gasification can be achieved via combustion at high temperatures. Combustion has inherent characteristics, however, that make it unattractive for consideration in the MAG process. In particular, the use of zero valent ferromagnetic metals as catalytic media is precluded because these would oxidize and result in non-magnetic reaction products.

Three solid waste materials were selected for use in our initial gasification experiments: wheat straw, tissue paper, and canine feces. Ash and moisture contents for these solid types are summarized in Table 7.1. Pyrolysis experiments were conducted using tissue paper. Following this, all three materials were separately gasified by ambient pressure steam reformation at reactor temperatures of 650, 700, and 750 °C. In addition to this set of experiments, pressurized batch steam reformation gasification runs were also conducted over a range of temperatures and pressures, using a modified test stand.

Table 7.1. Summary of Solid Waste Ash and Moisture Content.

Material	% Ash	% Moisture
Wheat Straw	5.38 +/-0.43	7.87 +/-0.43
Tissue Paper	0.324 +/-0.012	5.40 +/-0.40
Dog Feces	8.05 +/-6.45	40.37 +/-23.45

Gasification by-product distributions for tissue paper pyrolysis experiments conducted at heating rates of 30°C/min to 400°C and 800°C end point temperatures are summarized in Figure 7.4. While the ash and moisture produced are equal at the two temperatures, the 800°C pyrolysis run generated significantly more gas, while producing less char and tar. The results of ambient temperature steam reformation experiments using tissue paper samples over the temperature range between 400°C and 800°C are shown in Figures 7.5 and 7.6. Significantly, the char fraction was completely eliminated in the runs conducted at 700°C and above. A comparison of the results for pyrolysis and steam reforming at 800°C is shown in Figure 7.7. The temperature trends for the production of char, tars, and gases by ambient pressure steam reforming are illustrated in Figure 7.8. Clearly, the end-point temperature of 700°C provided the best outcome. Pressurized steam reformation experiments were less successful.

Based upon these results, ambient pressure steam reformation was selected as the primary gasification mechanism for employment in the first integrated Magnetically Assisted Gasification hardware.

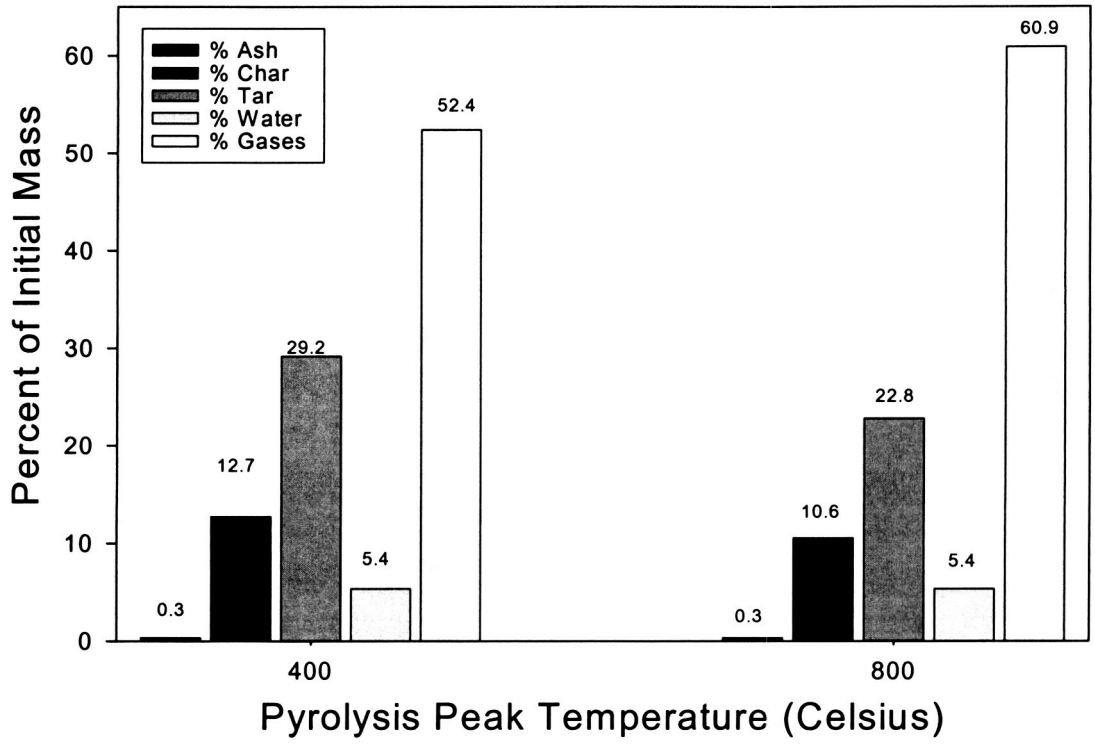

Figure 7.4. Tissue Paper Pyrolysis at End Point Temperatures of 400°C and 800°C.

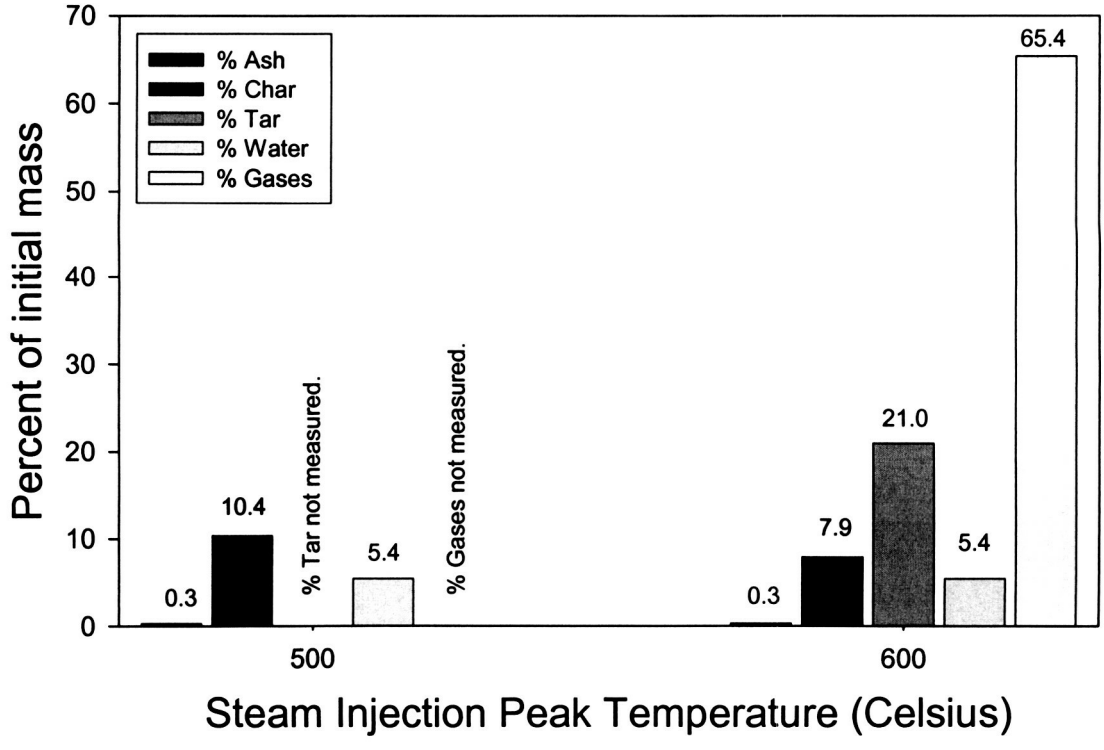

Figure 7.5. Ambient Pressure Steam Reformation of Tissue Paper at 500°C and 600°C.

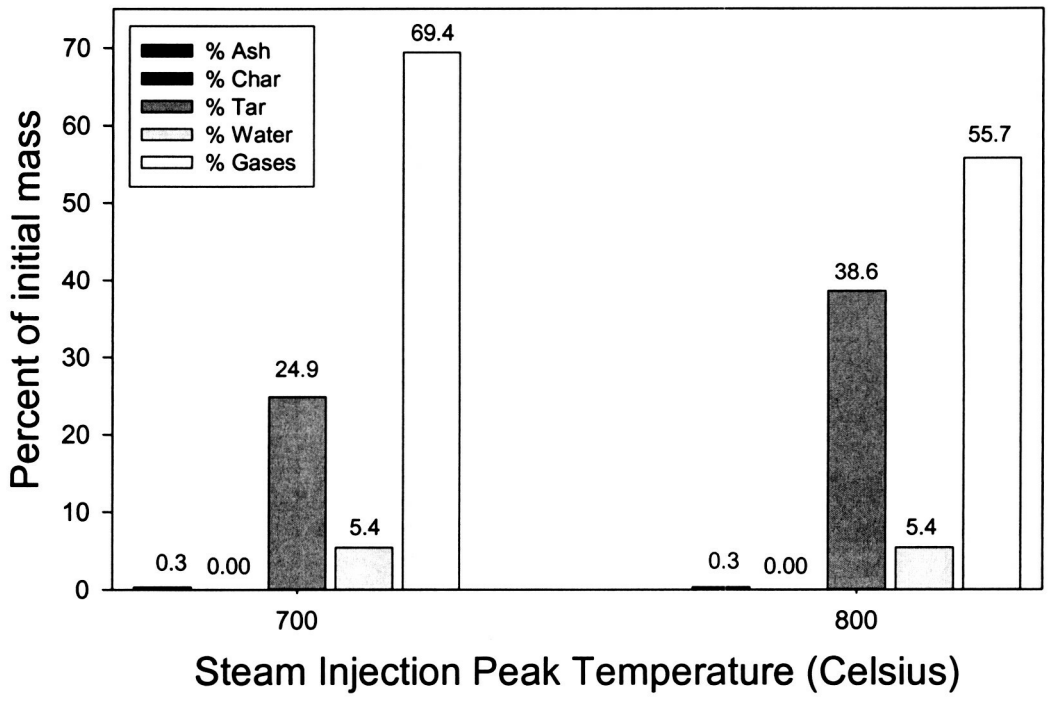

Figure 7.6. Ambient Pressure Steam Reformation of Tissue Paper at 700°C and 800°C.

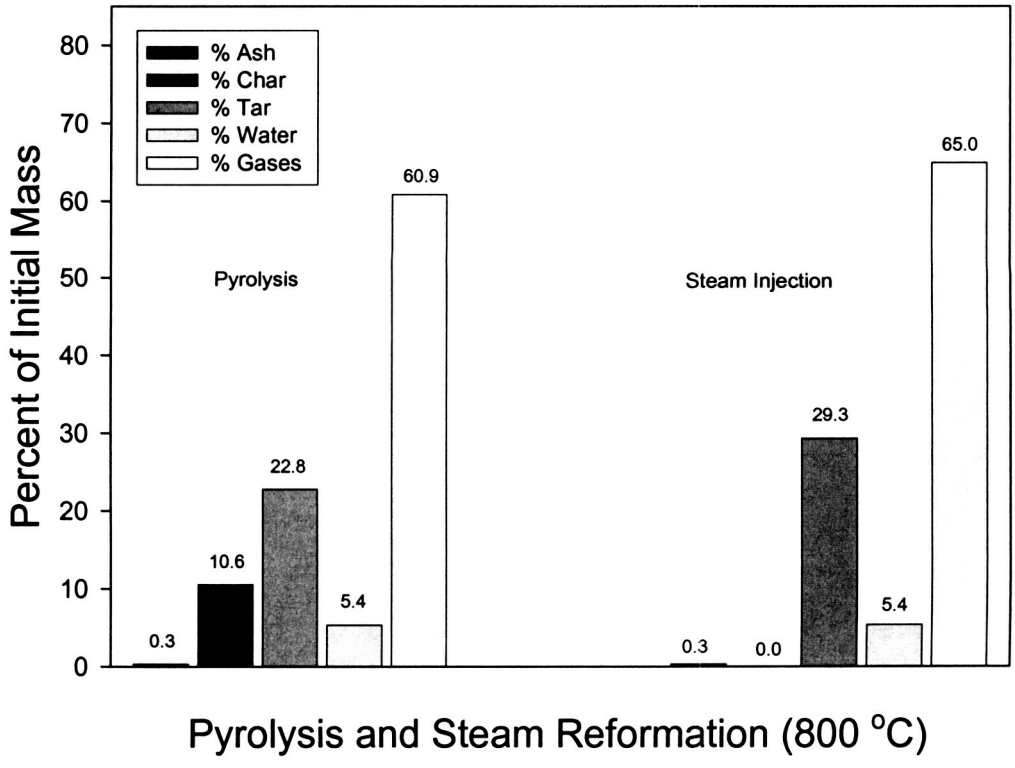

Figure 7.7. Comparison of Pyrolysis and Steam Reformation at 800 °C.

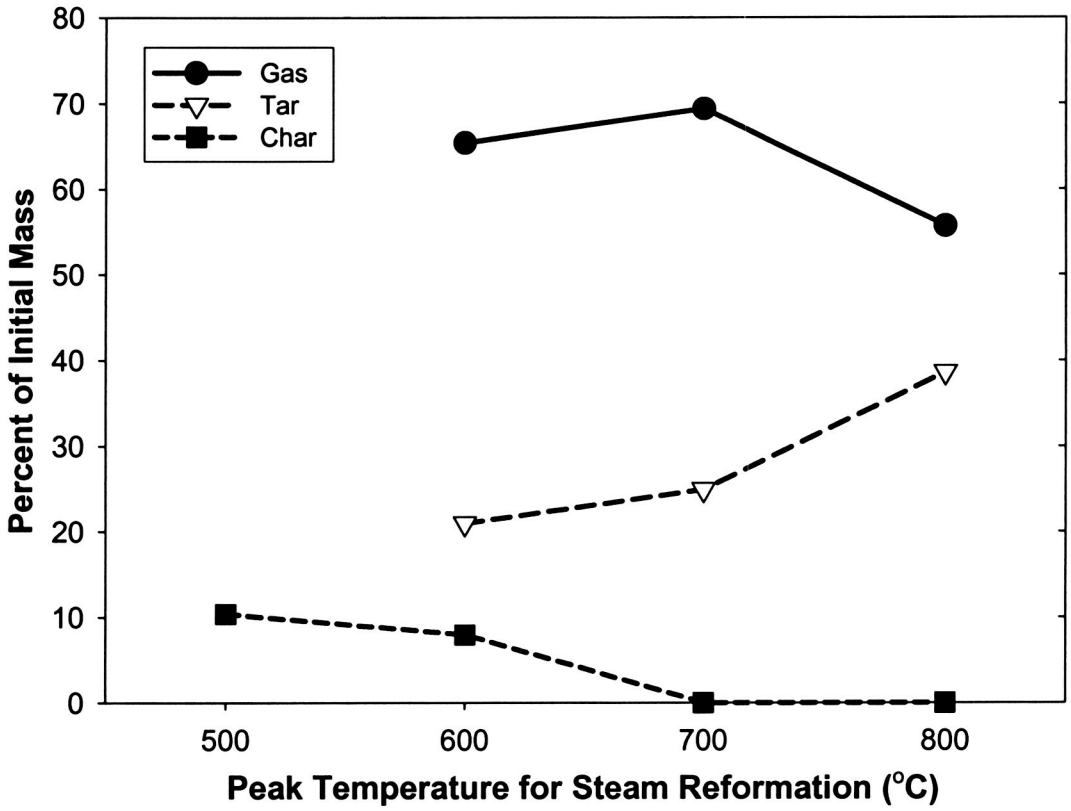

Figure 7.8. Temperature Trends for Char, Tar, and Gas Production via Ambient Pressure Steam Reformation.

8. HARDWARE DESIGN, ASSEMBLY AND COMMISSIONING.

The integrated Magnetically Assisted Gasification (MAG) test apparatus was designed as an intermediate scale system for the demonstration and refinement of basic processes and for the continuing investigation of magnetic control and solid waste destruction methods. The overall design of the MAG apparatus reflects the original three-step gasification and resource recovery concept in which solid wastes are separated and concentrated from a recirculating aqueous suspension by magnetically assisted filtration, the organics within the solids are decomposed to produce low molecular weight gases such as CO_2, H_2O, H_2, and CH_4 by thermocatalytic means, and the inorganic residue (ash) is removed by fluidization and collected by filtration. Because this apparatus is to serve as a test-bed with which to advance the technology to higher states of readiness, the system was designed with two columns, rather than the single column configuration originally conceived. Fluidization and gasification reactions are performed in the 'hot column' which is high temperature capable and hence shrouded in steel and insulation. The 'cold column' is composed of transparent plastic, a feature which allows visual observation of magnetically assisted fluidization and filtration phenomena. Solids are captured from a recirculating aqueous stream by filtration within the 'cold column'. Once the filter is fully loaded, the ferromagnetic media are fluidized, thus releasing a concentrated stream of solids which are transferred to the hot system were gasification reactions take place. The MAG system was designed to implement gasification via ambient pressure steam reformation, however, the fluidized bed reactor is also compatible with operation in pyrolysis or incineration modes. Finally ash is removed during gas-solid fluidization within the hot column, and collected by filtration.

8.1 Magnetically Assisted Gasification Hardware Design and Assembly. As shown in the photograph presented in Figure 8.1, the Magnetically Assisted Gasification (MAG) apparatus consists of two fluidization columns housed within a welded frame which is constructed from 3.81 cm (1.5 inch) steel strut. The powder coated frame measures 121.92 cm (48 inches) in width, 194.31 cm (76.5 inches) in height, and 71.12 cm (28 inches) in depth. Located in the center of the frame are the hot and cold columns. The hot column or gasification reactor is located on the left and the cold column for filtration and fluidization is located on the right.

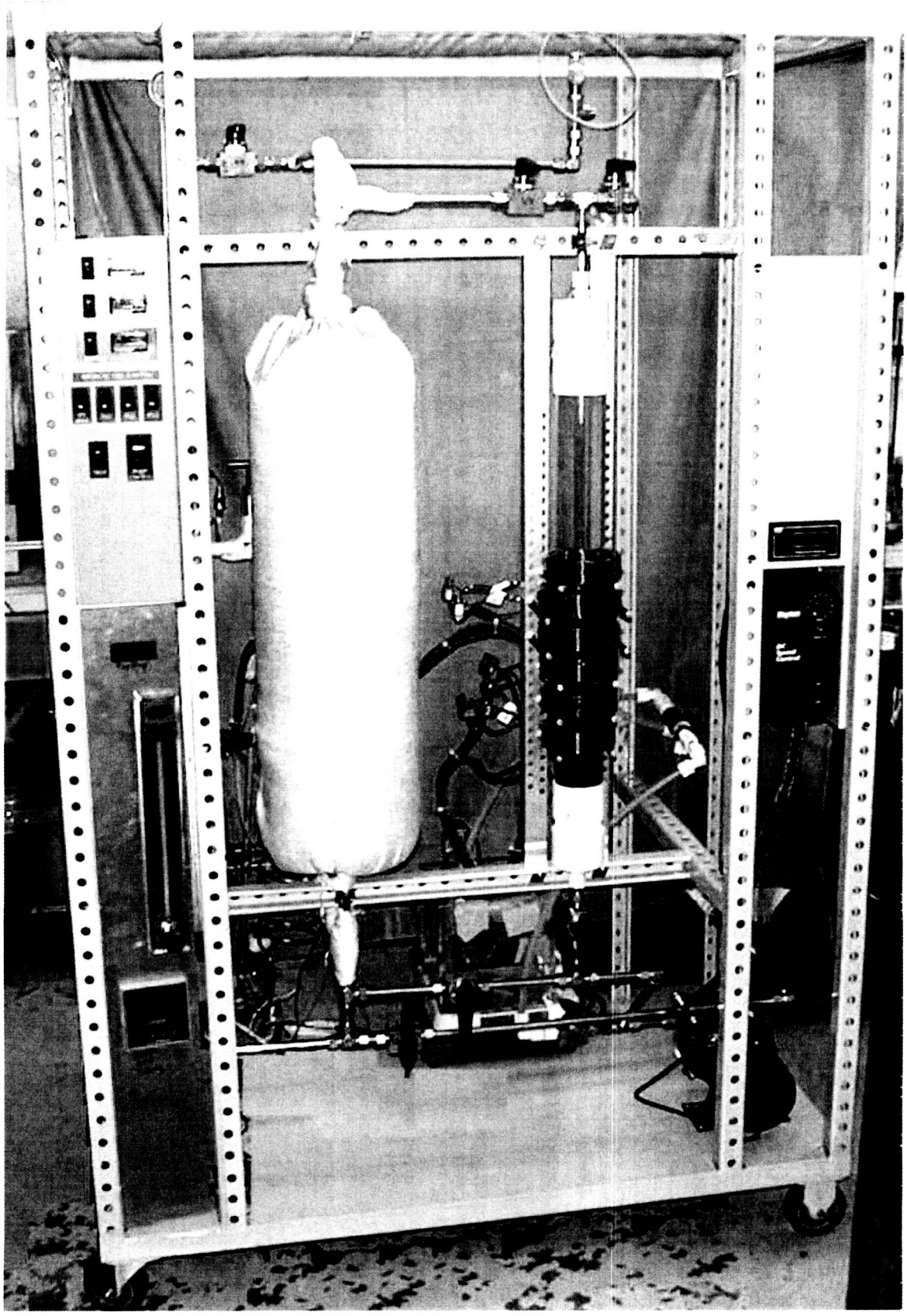

Figure 8.1. MAG Apparatus (front view).

The gasification reactor consists of a 304-stainless steel tube, 7.30 cm (2.875 inches) in diameter, 76.20 cm (30 inches) long, and with a wall thickness of 0.71 cm (0.28 inch). The reactor tube is encased in a set of four radiant heaters. Covering the heaters are several layers of high temperature mineral fiber insulation. The outer covering of the reactor tube is a high temperature fiberglass shroud, which aids in insulating the reactor while also containing the mineral fibers. The reactor heaters are arranged in two sets of two, forming the upper and lower heating sections in the reactor. Each of these sections is individually controlled and capable of producing 900 watts of power at 120 volts.

The cold fluidization/filtration column is fabricated from acrylic tubing, and has the same dimensions as for the gasification reactor. Six sets of Helmholtz coils surround the cold column, which, when energized with DC power, provide a time invariant magnetic field and magnetic field gradient directed downward toward the distributor plate. A set of perforated aluminum tubes, on each side of the column, allows the positions of the magnetic coils to be adjusted. The electromagnets consist of Helmholtz coils ranging between 60 and 96 turns of 10 gauge imide-amide insulated copper wire. The six magnetic coils were designed to be used in pairs. The three corresponding power supplies are contained within the main electrical control box.

The pump used to circulate suspended solid wastes is located below and slightly to the right of the cold column. This pump is a single armature, variable speed DC motor rated at 1/3 horsepower. The speed of the pump is controlled by a dial setting on the pump controller, located on the front of the frame, and is displayed on the tachometer located above the pump controller on the right hand side of the frame, between the front support members. The tachometer displays the rotational rate of the pump in RPM. The tachometer can also be configured to provide process flow rates, in liters per minute. Below the tachometer is the pump controller, which allows for operation of the pump over the range of 400 to 1600 RPM, and provides a power switch and indicator lamp.

The solid waste/fluid reservoir is positioned behind the cold column, on the base plate of the frame. The reservoir consists of an 18.9 L (5 gallon) polyethylene tank. The tank is mounted on top of a magnetic stirrer. All liquid effluent streams from the filtration column and gasification reactor return to the

reservoir, allowing the unit to be run in a closed loop configuration. The magnetic stirrer ensures that the solids which are to be processed remain in homogenous suspension.

A steam generator is located to the left of the waste reservoir, and behind the gasification reactor. The steam generator is mounted against the rear support strut just above the base of the frame. This critical component was fabricated from a 60.96 cm (24 inch) long, 10.16 cm (4 inch) diameter 304 stainless steel tube. The lower portion of the tube is surrounded by three band heaters. The entire length of the tube (including heaters) is wrapped with several layers of mineral fiber insulation and then encased in a high temperature fiberglass shroud, in the same manner as for the gasification reactor. Each of the band heaters is capable of delivering 650 watts of power at 120 volts. The temperature of the steam generator is regulated by a PID controller located in the main electrical control box. A heat exchanger, consisting of a coil of 0.64 cm (0.25 inch) inner diameter stainless steel tubing, is located within the steam generator. When connected to the reactor effluent, the heat exchanger is used to recover waste heat from the reactor during the gasification phase of MAG operation.

In addition to the steam flux, a small flow of nitrogen is also introduced to provide a positive gas flow at all times through the reactor and on to the tar trap and condenser. Reaction gases exit the reactor through 1.27 cm (0.50 inch) SS tubing and then pass through a high temperature valve and on to the tar trap. This section of tubing and the high temperature valve are heated by spirally wrapped heat tape.

Control and Display. The main electrical control box, shown in Figures 8.2 and 8.3, is positioned on the left hand side of the frame. just below the center support member. The electrical control box houses all electrical fusing and distributions from the main 120 volt and 220 volt lines. The electrical control box also houses the three power supplies which are employed for magnetic field generation. These regulated AC/DC power supplies each produce up to 200 watts of power with an output of 5 volts DC. The PID controllers responsible for regulating temperature in the steam generator and reactor are also located within the control box. The PID controllers are Omega controllers, model number CN132. On the front face of the electrical control box are the displays for the PID controllers and the accompany-

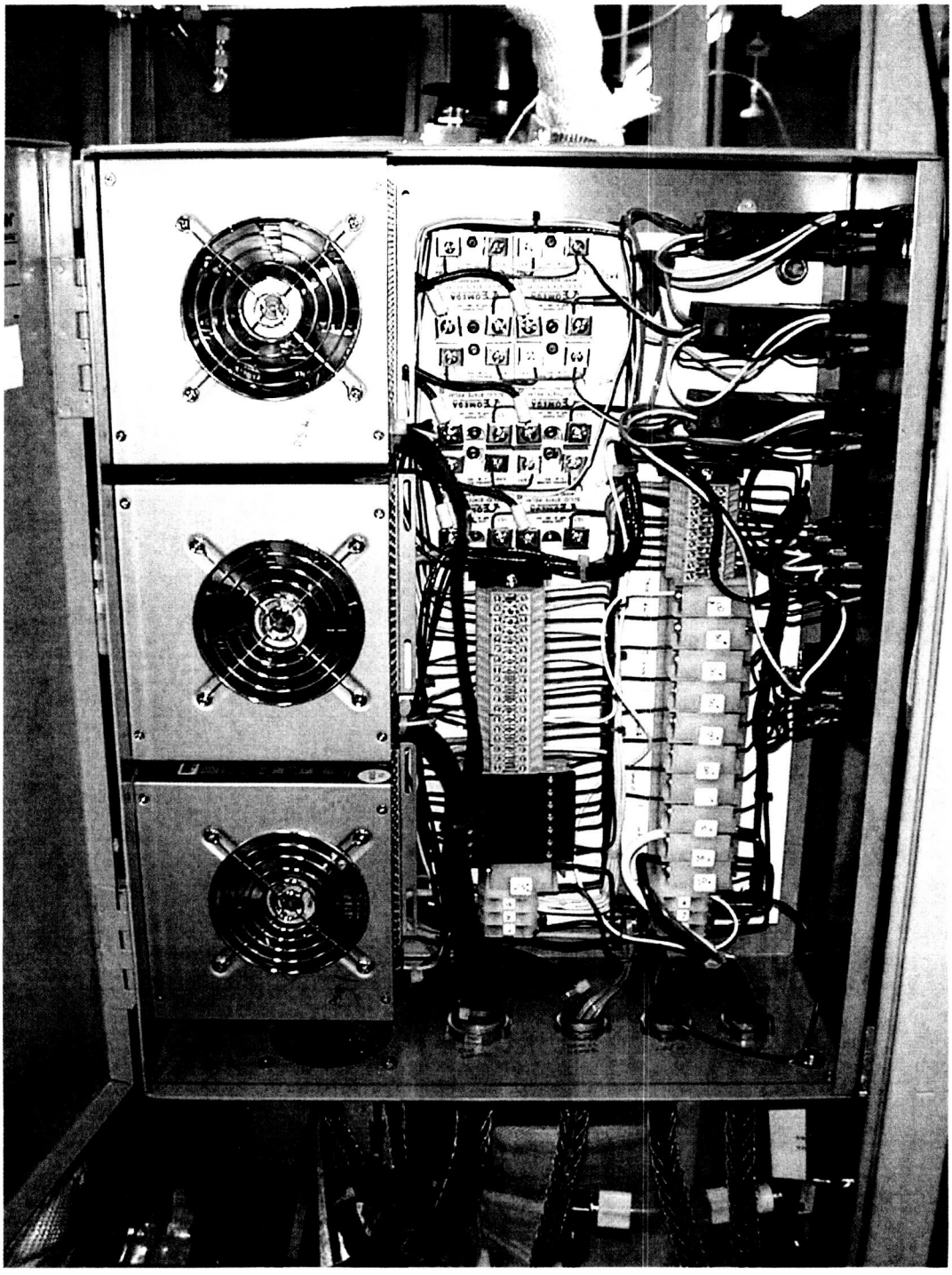

Figure 8.2. MAG Electrical Control Box (view with cover open).

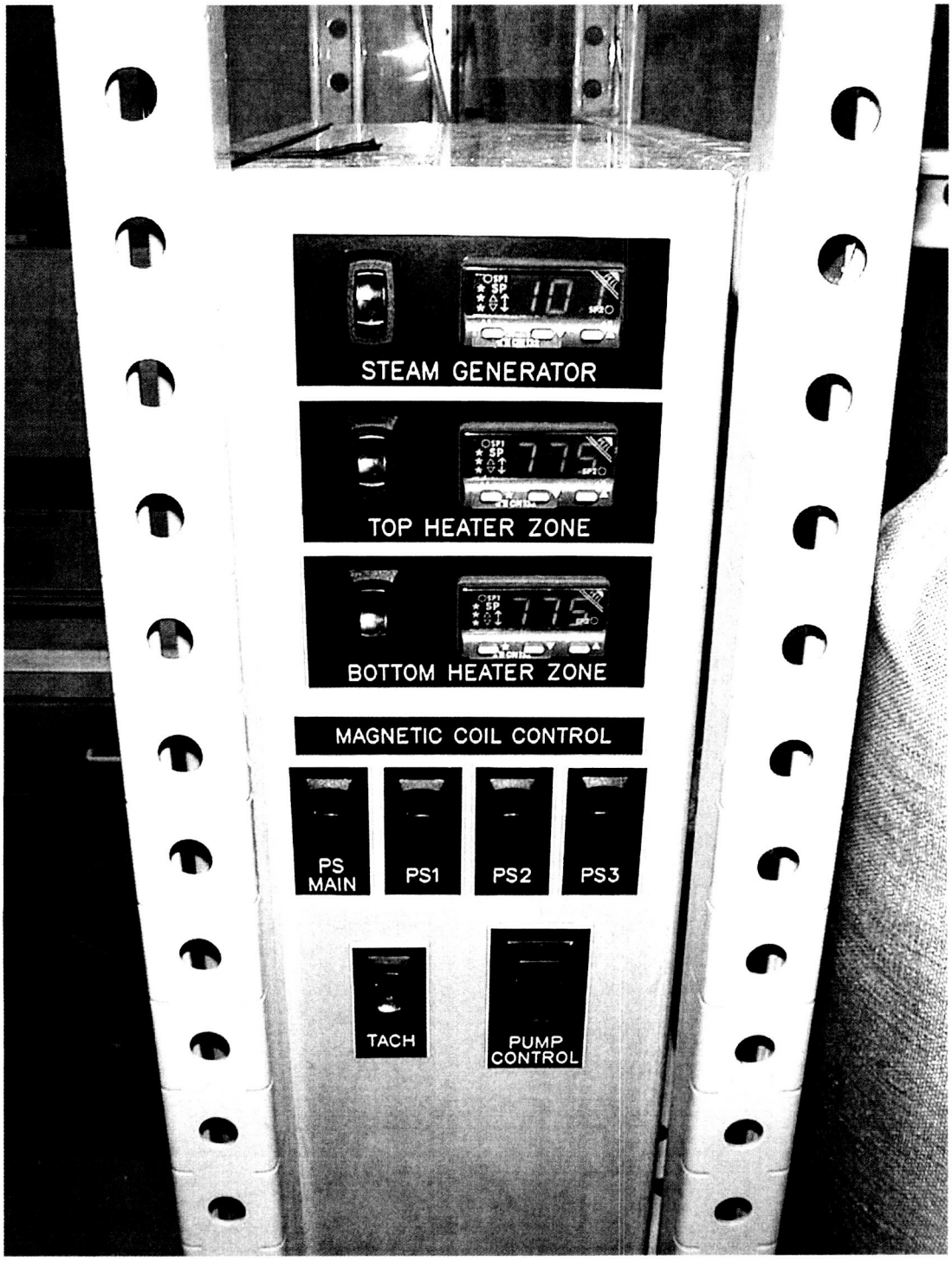

Figure 8.3. MAG Electrical Control Box (front view).

ing switches (from top to bottom: steam generator, top reactor zone, and bottom reactor zone). Below the three PID controls are the set of switches, which control the magnetic field generator. Each power supply (and the two coils it powers) can be turned on or off individually by the appropriate switch. A master switch is also present which energizes all power supplies. Tachometer power and pump controller switches are located at the bottom of the electrical control box.

Below the electrical control box is a digital display which is used to monitor the tar trap exit gas temperature, as indicated by the in-place thermocouple. Below the temperature indicator is a variable area gas flow meter / flow controller, which is used to set the desired gas flow rate during the fluidization phase of operation. An Omega CN8500 PID controller, located below the flowmeter, is used to maintain an elevated temperature for the tubing section exiting the reactor. This prevents condensation of higher molecular weight organics prior to entering the tar trap.

Process Design. A process flow diagram for the MAG apparatus is shown in Figure 8.4. Although the fundamental design concept for the MAG process calls for a single reactor column which accommodates all three processing steps (filtration, gasification, ash removal), we added a second column (column B) into the design of the MAG demonstration unit to facilitate visual demonstration. The two columns are identical in size but differ as to the functions which they perform. The hot column (column A) is equipped to perform all three steps in the thermal conversion of solid waste, as originally envisioned. To accommodate high temperature gasification, column A is fabricated from stainless steel, is well insulated, and is built to operate at temperatures in excess of 600 °C. These features, however, obviously preclude visual observation of the reactor interior during operation. However, the cold column (column B) can be used, at room temperature, to perform separation of solid wastes by magnetically assisted filtration with concurrent visual observation of the process. Additionally, the column B can be employed to investigate magnetically stabilized fluidization phenomena under ambient temperature conditions.

The MAG demonstration unit was designed to operate in a 1g environment. Demonstration of the operation of the magnetic field gradient based fluidization.

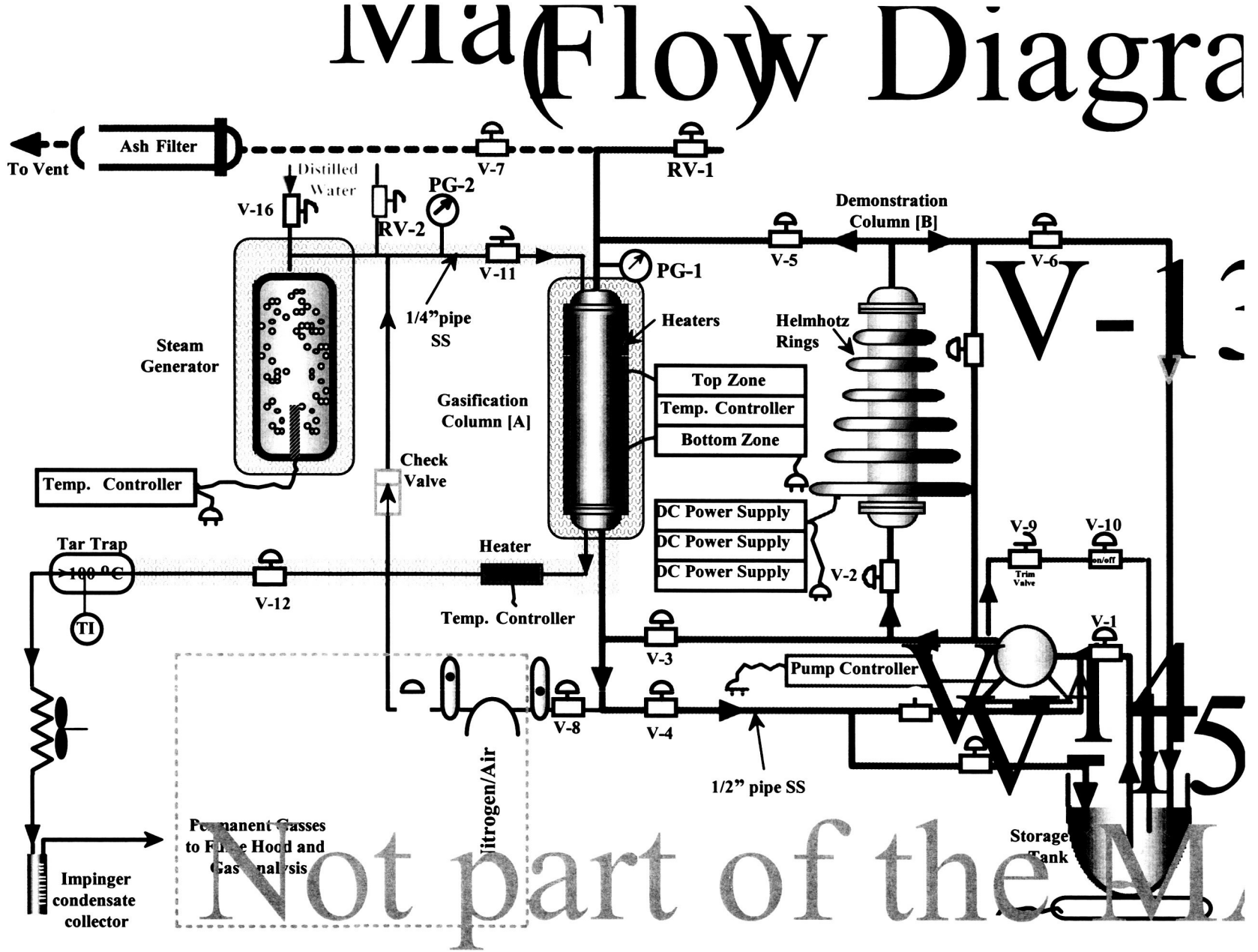

Figure 8.4. Magnetically Assisted Gasification (MAG) Flow Diagram.

and filtration control methods is greatly facilitated by visual access to the operation of the column. This is the reason why the hot column (column A) is not equipped with the magnetic field generator, but rather column B is configured with a set of six Helmholtz rings for the generation of the desired magnetic field strength and field gradient. The absence of the magnetic field generator in the construction of the hot column does not change the operation of this column in normal gravity. At lower 'g-s' or in microgravity the use of the magnetic field is necessarily needed in the hot column, and this will certainly be incorporated into the next generation of MAG hardware. For the present investigation, however, we reduced the role of the magnetic field to only the operation which is critically needed for restoration of the fluidization regime following filtration in microgravity. Operational parameters, such as fluid velocity, waste solids loading, heating rate, operating temperature, size of the fluidized bed particles, steam to carbon ratio, etc., have all been made adjustable within designed ranges. This flexibility allows for extensive modification of operating conditions which may be required in the treatment of different classes of solid waste materials and will facilitate the identification of the most favorable conditions for a given application.

The full range of operational capability for the MAG demonstration unit is represented by 11 flow loop operating modes. Each loop represents either one of the three major processing steps (filtration, gasification, ash removal) or one of the facilitating functions, such as drainage, and column flooding. These operating flow loops include:

1) Magnetically Assisted Filtration of Solid Waste in Column B (Loop FB).

2) Filtration of Solid bio-waste in Column A; bottom-to-top (Loop FA).

3) Filtration of Solid bio-waste in Column A; top-to-bottom (Loop FAr).

4) Steam Gasification of Solid bio-waste (Loop SG).

5) Pyrolysis of Carbonaceous Residue (Loop PR).

6) Combustion of Carbonaceous Residue (Loop CO).

7) Ash Removal (Loop ASh).

In addition to these basic flow loops, several combinations of flow loops are possible in the MAG demonstration unit. For example, filtration of the solid waste can be accomplished in the column B, followed by transfer of the filtrate to the column A prior to initiation of the gasification cycle. This operation is presented in the flow loop diagram FBA.

8) Transfer of Filtrate from Column B to A. (Loop FBA)

Steam gasification of the solid waste can be realized simultaneously with the filtration of the bio-waste in the column B. This operation is presented in the flow loop diagram SG/FB.

9) Simultaneous Gasification and Filtration (Loop SG/FB)

Operationally, there is a need to partially drain column A after the filtration step (or after the transfer of the filtrate from column B) before the gasification step can start. To facilitate this transient operation we designed an additional operating loop (DR) in which an air stream is used to partially remove the water phase from column A. A similar operation can be performed with column B, if necessary.

10) Assisted Column Drainage (Loop DR).

Prior to filtration in column A, which contains air after the gasification and ash removal steps, it is first filled with the liquid phase, as per operating loop FLA.

11) Flooding of Column A (Loop FLA).

In the operation of the above-mentioned flow loops, a number of valves must be properly positioned. The positions of valves for each operating loop are summarized in Table 8.1. A key is also provided for use in conjunction with the instrumentation diagram presented in Figure 8.5. Each of these process flow loops is discussed in greater detail below.

Table 8.1. MAG Apparatus Process Loop Valve Positions and Key to Instrumentation Diagram.

Valve Positions

	V-1	V-2	V-3	V-4	V-5	V-6	V-7	V-8	V-9	V-10	V-11	V-12	V-13	V-14	V-15
Loop - FB	O	O	C	C	C	O	C	C	O	O	C	C	C	C	C
Loop - FLA	O	C	O	C	O	O	C	C	O	C	C	C	C	C	C
Loop - FA	O	C	O	C	O	O	C	C	O	O	C	C	C	C	C
Loop - FAr	O	C	C	O	O	C	C	C	O	O	C	C	O	C	O
Loop - FBA	C	O	C	O	O	C	C	C	O	C	C	C	C	O	C
Loop - DR	C	C	C	O	C	C	C	C	O	C	O	C	C	C	O
Loop - SG	C	C	C	C	C	C	C	C	O	C	O	O	C	C	C
Loop - PR	C	C	C	C	C	C	C	C	O	C	O	O	C	C	C
Loop - CO	C	C	C	C	C	C	C	C	O	C	O	O	C	C	C
Loop - ASh	C	C	C	C	C	C	O	O	O	C	C	C	C	C	C
Loop - SG/FB	O	O	C	C	C	O	C	C	O	O	O	O	C	C	C

C = Closed valve
O = Open valve

Instrumentation Key

Temperature Indicator	**Pressure Indicator**	**Temperature Controller**	**Voltage Indicator**
Level Indicator	**Flow Controller**	**Pressure Controller**	**Level Indicator**
Analysis gas/solid	**Concentration Indicator**	**Voltage Controller**	**Current Controller**

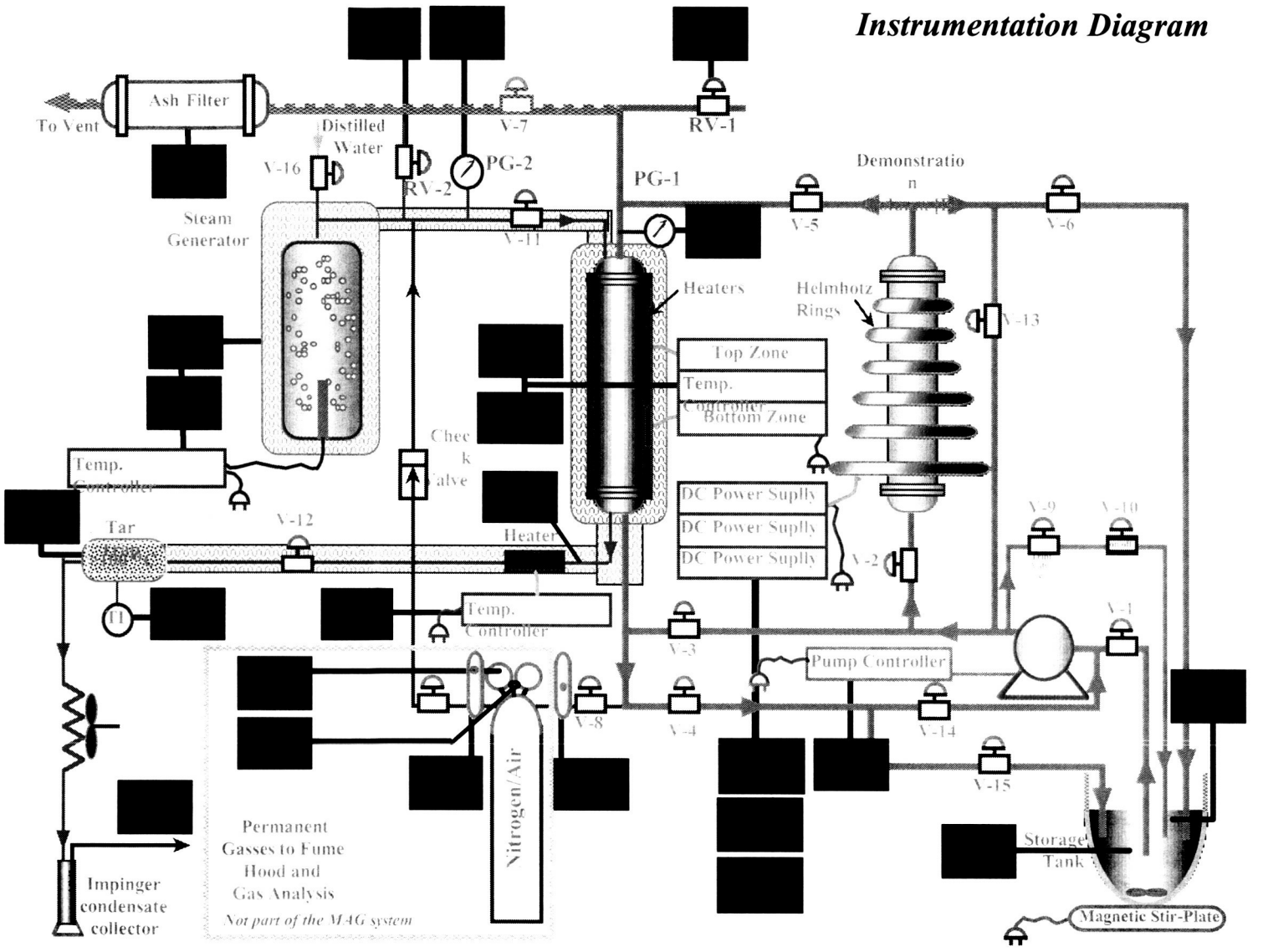

Figure 8.5. Instrumentation Diagram for Magnetically Assisted Gasification Test-Bed.

Magnetically Assisted Filtration of Suspended Solid Wastes in Column B (Loop FB). This process loop, illustrated schematically in Figure 8.6, is used to segregate and concentrated solid waste materials from a recirculating aqueous suspension using the Plexiglas column B. Operation of the filtration column is initiated by energizing the Helmholtz rings which create the desired magnetic field gradient and magnetic force which acts in the direction opposite to that of fluid flow. All valves are positioned as indicated in Table 8.1 and the variable speed control of the pump is slowly raised to the desired flow rate. In 1g experiments, the flow rate should not exceed the minimum fluidization velocity. For operations in microgravity, the minimum fluidization velocity is strictly determined by the magnitude of the magnetic force acting on the ferromagnetic media, and therefore, the flow of the aqueous solid waste suspension must correspond to the magnetic force.

As the solid waste slurry flows through the consolidated bed of ferromagnetic filtration media, particulate matter is trapped within the intergranular spaces. Aqueous flow continuous to recirculate between the stirred solid waste holding tank and the filtration bed. In 1g operations, a point is eventually reached in which the accumulated solid waste trapped within the filtration media generates additional resistance to flow such that the whole bed may be lifted and fluidized. This situation can be prevented by further increasing the magnetic field strength or by terminating this phase of the operation. Once the column is saturated with filtered solids, the waste particles are then transferred to the high temperature reactor (column A) for gasification. The magnetic field is lowered and the bed is partially fluidized, thereby allowing trapped solids to be carried away with flow into column A. Details related to this operation are given in the description of Loop FBA.

The magnetically assisted filtration step hinges on the capacity of the magnetic field to maintain the ferromagnetic media in the packed bed regime and to constantly resist the increasing drag force which results from the increasing resistance to flow through the bed as intergranular spaces are filled with entrapped particles. One possible improvement of this operation may be realized by reversing the direction of the flow of the liquid phase, such that both, the drag force and magnetic force are acting in the same direction. In this operating mode

Filtration of Solid Bio-Waste in MAG System
(Loop FB)

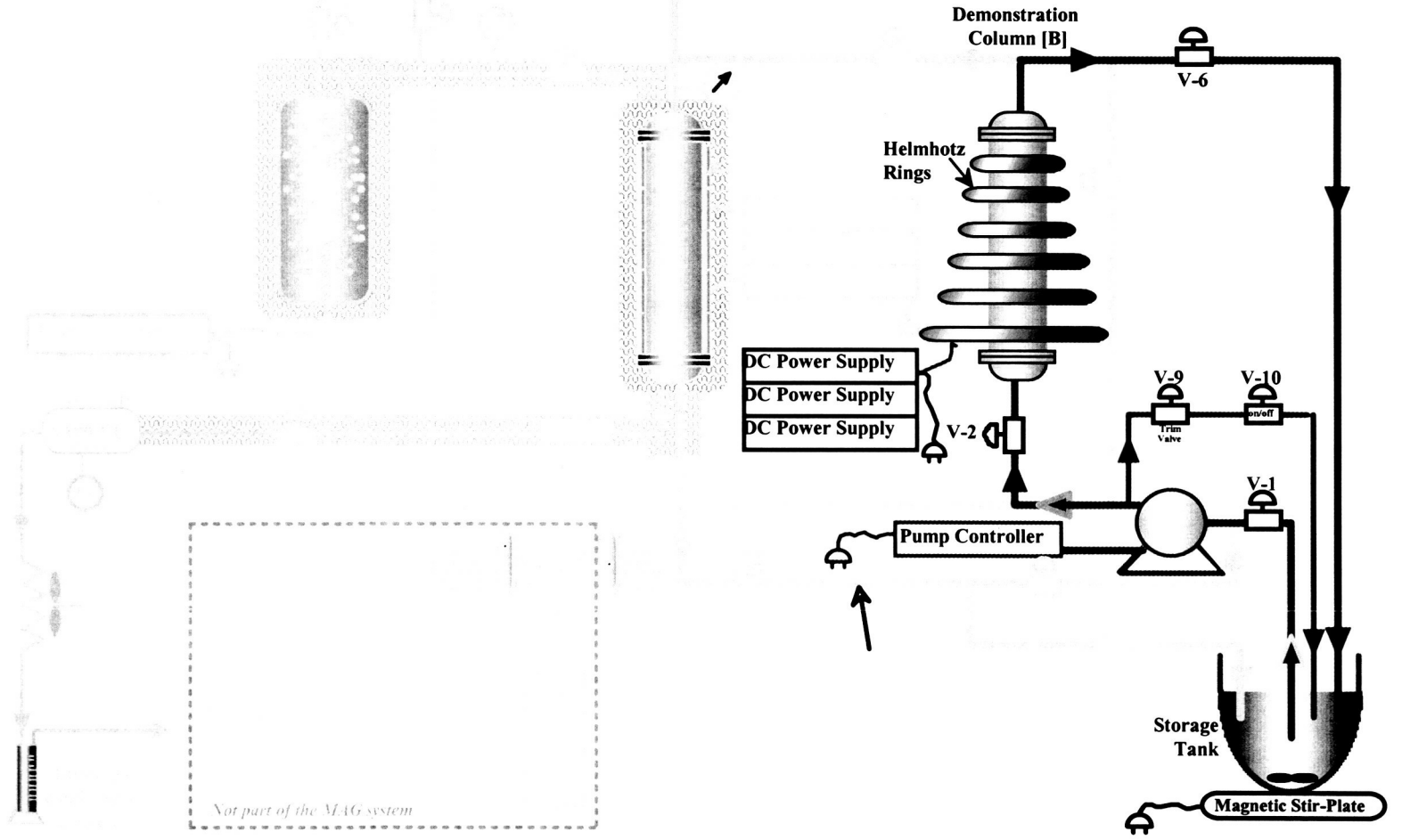

Figure 8.6. Loop FB - Magnetically Assisted Filtration.

the ferromagnetic media will be kept in the packed bed fixed against the distributor plate at the exit end of the column. Furthermore, the magnetic field could be turned off because it is not needed to support the structure of the packed bed, (drag force is sufficient) thus energy consumption for the field maintenance (300 W maximum) may be reduced. This regime for the filtration process is realized in column A and is explained in the description of the operation of the loop **FAr.** While this regime of operation reduces the energy load, the magnetic field cannot be completely eliminated. It is still needed for the maintenance of the fluidization regimes and for the restoration of the packed bed after the fluidization of ferromagnetic media. This need is inherent and unavoidable for microgravity and variable gravity operations at various points in transient functions and basic unit operations of the MAG process.

Gasification Reactor Flooding (Loop FLA). Once the filtration bed is fully loaded, the accumulated solids must be transferred to the heated reactor (column A) for gasification. Prior to the transfer, however, column A is first filled with water (see Figure 8.7). To accomplish this, water is pumped directly from the tank into the bottom of column A. Air is allowed to exit column A and pass on to the reservoir tank through valving at the top of the test stand. Water entering the bottom of the tank uniformly pushes air out the top of the column until all air is replaced by water except for a few trapped bubbles. We recognize that this operation is not microgvravity compatible. In microgravity, surface, interfacial, and hydrodynamic forces will predominate, thereby creating conditions under which liquid phase bypass and channeling phenomena may occur. However, we believe that this problem can be overcome in subsequent generations of the MAG hardware.

Transfer of Solids to the Gasification Reactor (Loop FBA). Once column B is flooded, transfer of the solid wastes is initiated as indicated in Figure 8.8. To accomplish this, the flow is diverted directly through the pump so that the storage tank is bypassed. The magnetic field intensity is then lowered (or removed in 1g operation) and the flow rate is increased. The resulting increase in drag force partially fluidizes the filtration media and allows particulate matter which has been trapped within the intergranular spaces to be carried away with the flow into the top of the gasification reactor, where it is trapped by the catalytic media.

Flooding of Gasification Column
(Loop FLA)

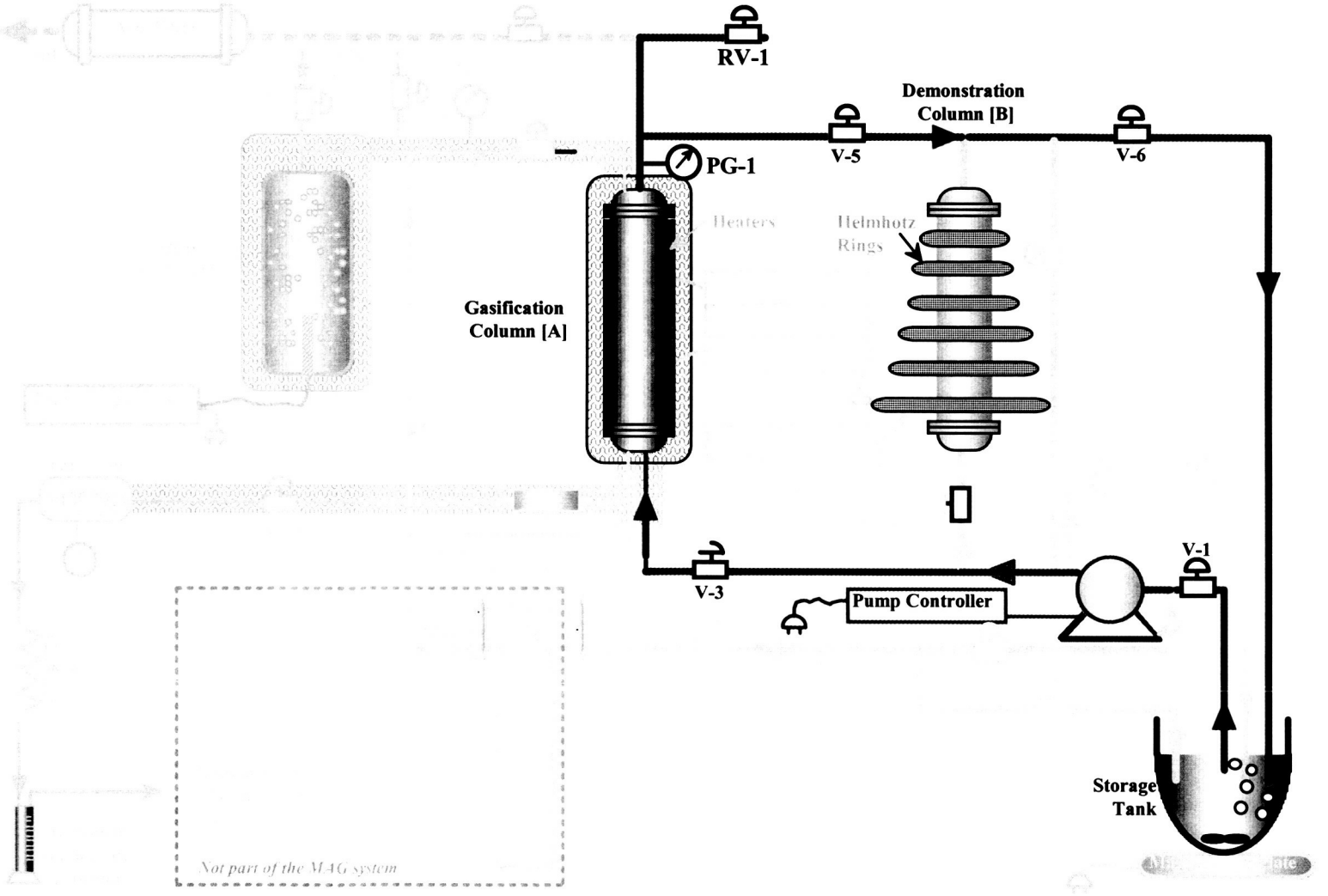

Figure 8.7. Gasification Reactor Flooding - Loop FLA.

Transfer of Filtrate from Column B to Column A (Loop FBA)

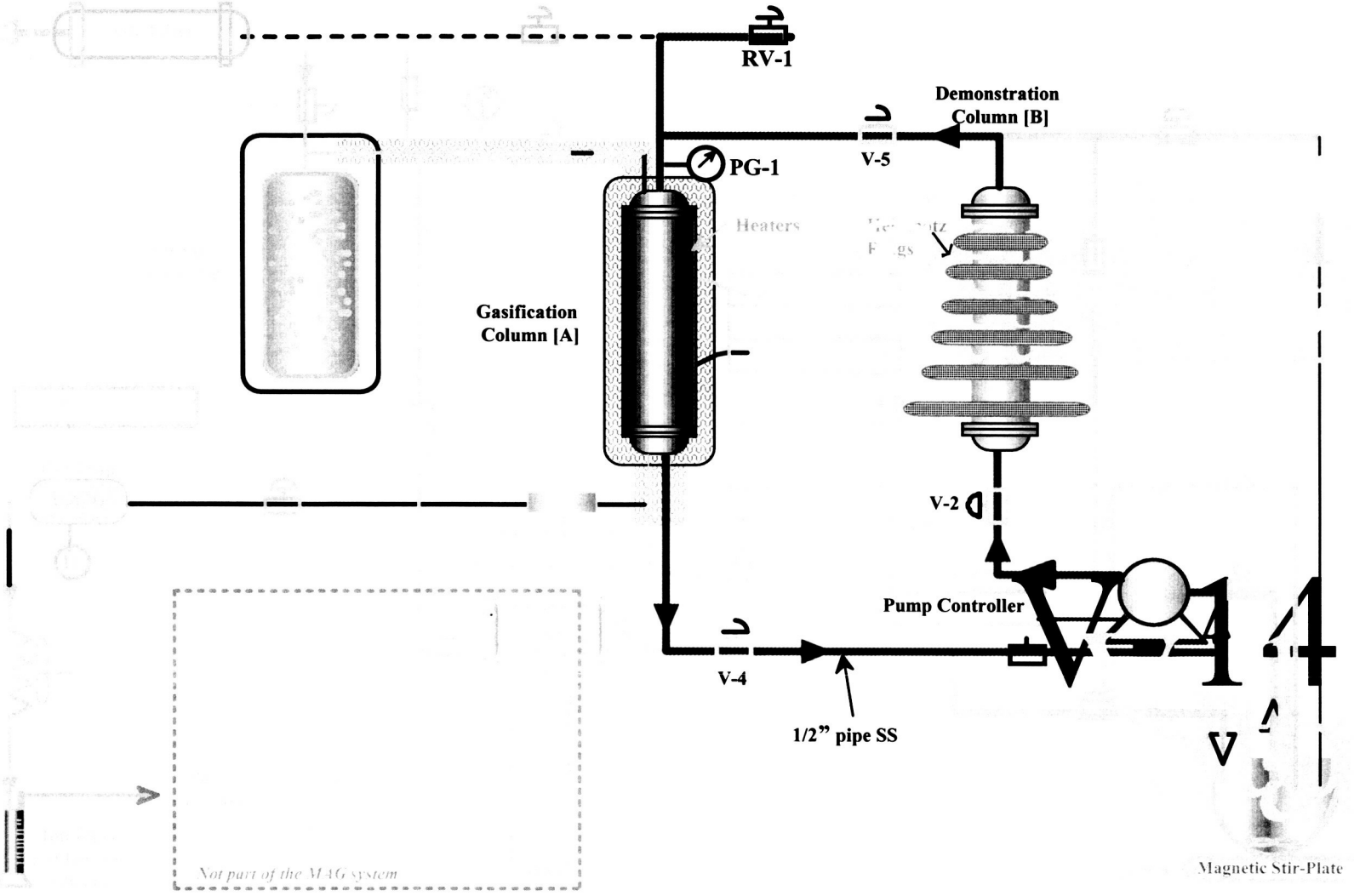

Figure 8.8. Transfer of Solids from Filter Bed (Column B) - Loop FBA.

Filtration of Solid Waste in Column A; Bottom-to-Top. (Loop FA). Alternatively, the filtration operation may be conducted within the packed catalyst bed inside the gasification reactor as shown in Figure 8.9 (flow loop FA). This operation is conducted in a similar manner to the filtration step performed in column B, with the exception that no magnetic forces are employed. The original conceptual design of the MAG system included only this mode of filtration (with magnetic fields present). However, since all processes within the hot column are obscured from visual observation, the cold column was added to facilitate further investigations. Beyond the materials of construction, the primary difference between column A and column B is in the type of ferromagnetic materials employed as fluidization media. Column A contains catalytic fluidization particles consisting of porous metallic cobalt beads which have a much higher density than the ferrite impregnated polymeric fluidization media which is employed in Column B. Due to the substantially more dense media in column A, employment of a magnetic field is not necessary to maintain a consolidated filter bed under normal gravity. The weight of the cobalt beads is sufficient to resists the pressure drop created by drag forces during the filtration of solid waste particles. Obviously this would not be the case in a microgravity environment where the density of fluidization media is irrelevant.

Filtration of Solid Waste in Column A; Top-to-Bottom (Loop FAr). It is also possible to conduct the filtration operation within column A, in the reverse flow mode in which solids enter the top of the bed and water is drained from the bottom (Figure 8.10). This mode of operation is favorable for the reduction of energy usage during filtration because the fluidization media are pushed against the distributor plate on the opposite side of the column, thus minimizing the need for additional magnetic forces to support the structure of the packed depth filter. It is anticipated that this mode of operation will be employed in future MAG systems because it is more efficient and can be employed in all gravitational environments.

Assisted Column Drainage (Loop DR). After the filtration step, or after the transfer of the filtrate from column B, excess water is removed from the system before the gasification reactions commence. To facilitate this transient operation we included an additional operating loop DR, in which an air stream is used to force most of the liquid phase water. This process loop is illustrated schematically in Figure 8.11.

Filtration of Solid Bio-Waste in MAG System
(Loop FA)

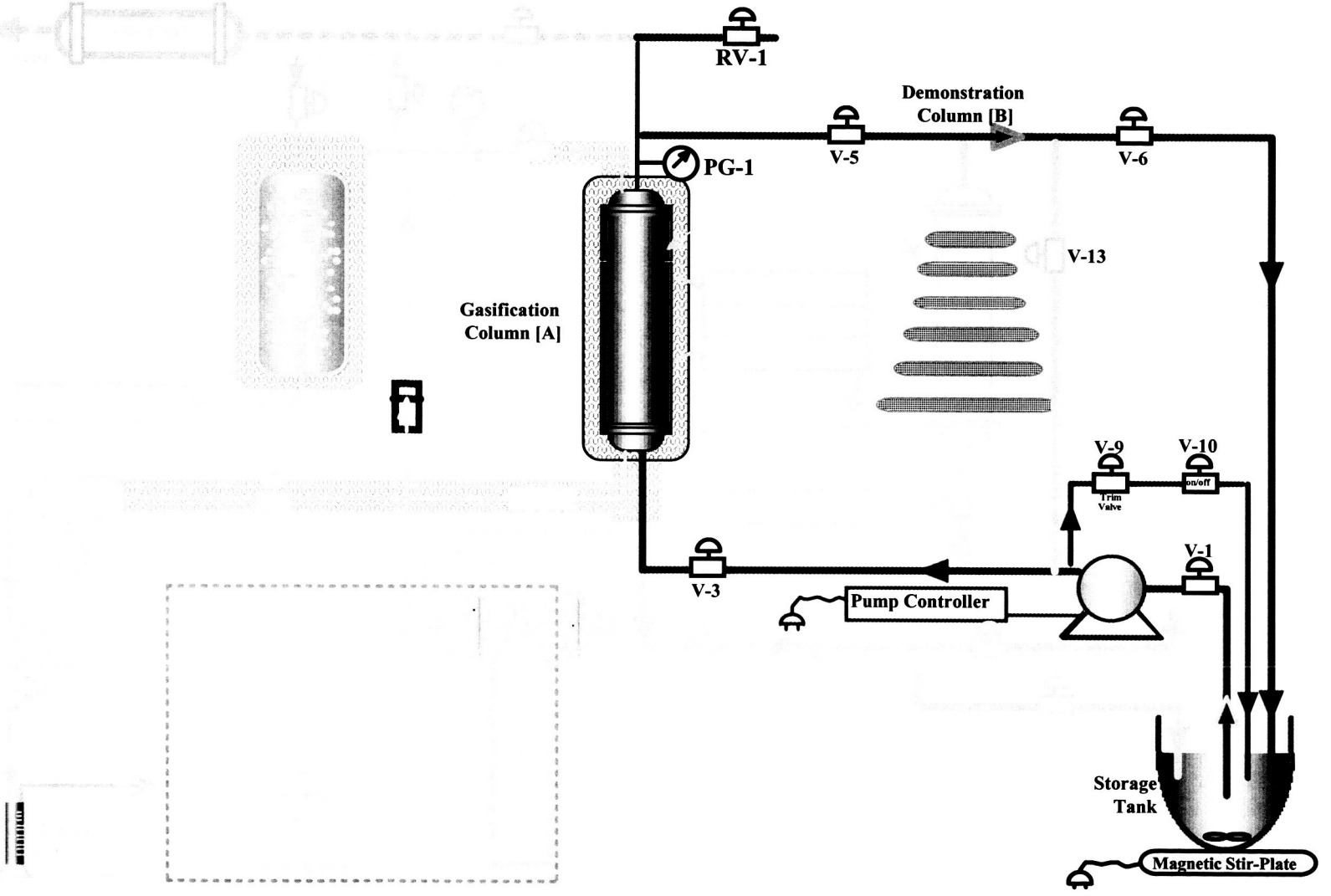

Figure 8.9. Filtration in the Gasification Reactor - Loop FA.

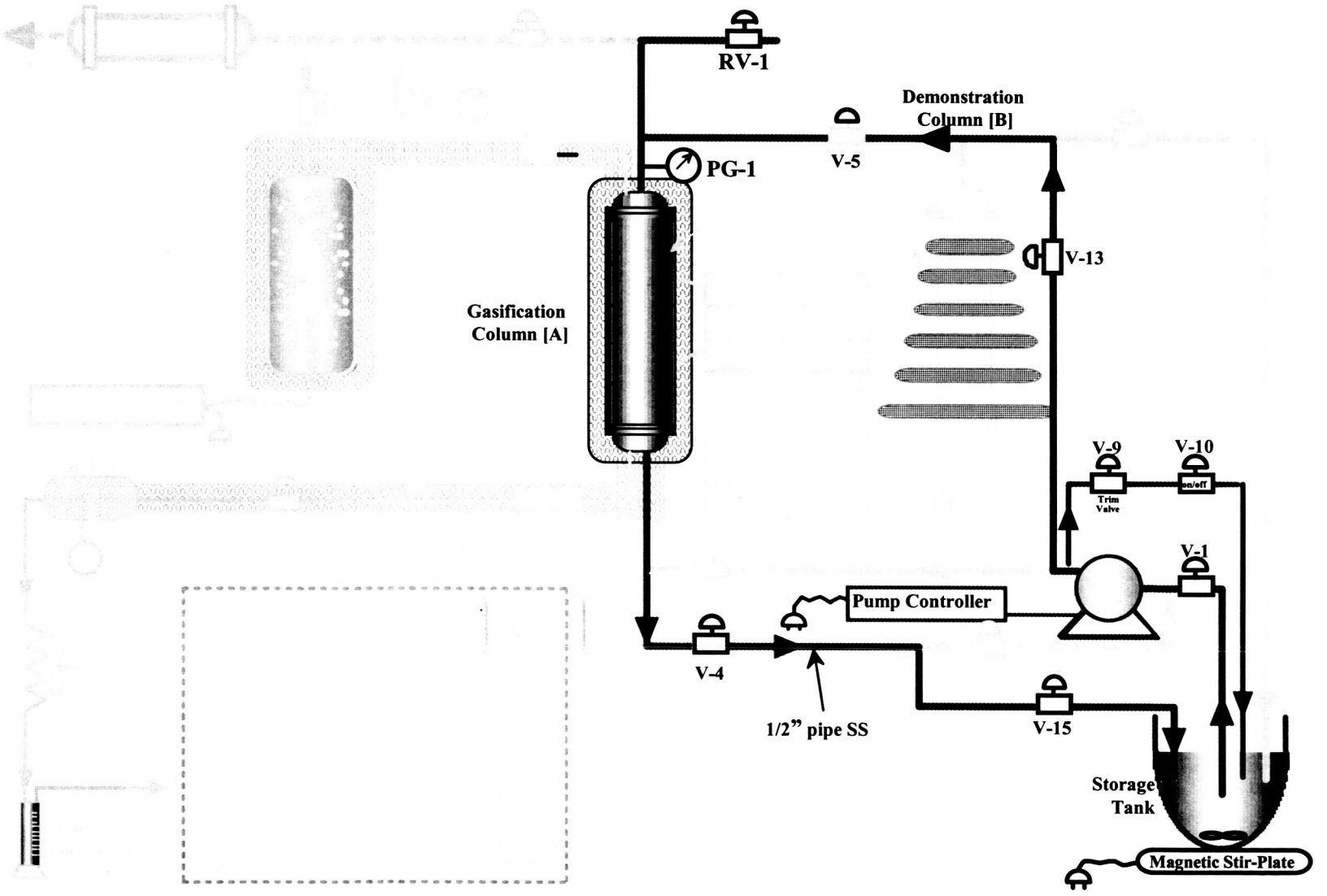

Figure 8.10. Reverse Flow Filtration in Gasification Reactor - Loop FAr.

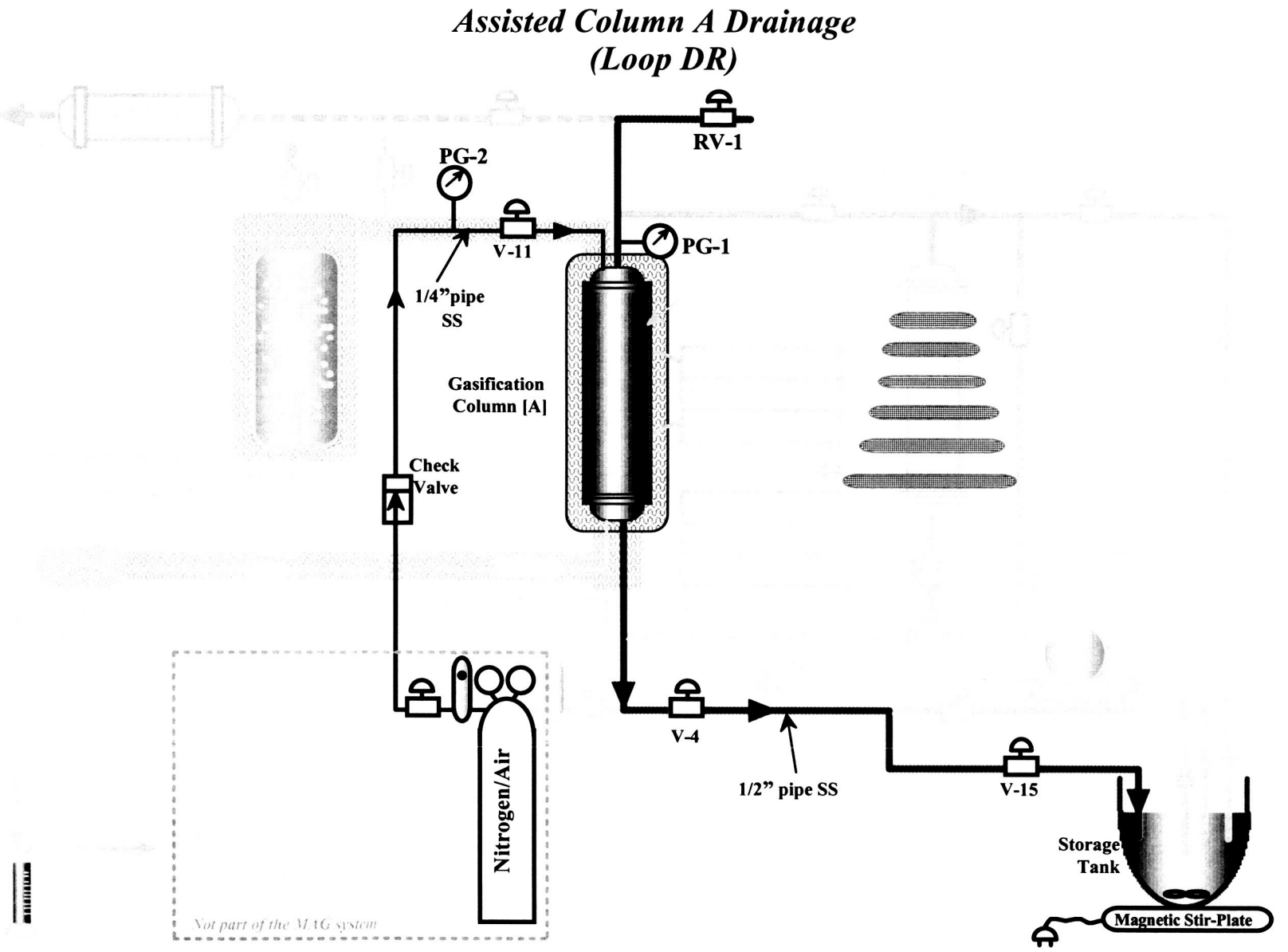

Figure 8.11. Water Removal from Gasification Reactor - Loop DR.

In normal gravity, this step is simply achieved by opening the valves at the bottom of column A which lead to the fluid reservoir and then either providing a positive pressure at the top of the column (with nitrogen or air) or merely allowing the column to gravity drain with the top of the column open to atmosphere through the appropriate plumbing. In microgravity, of course, the latter technique will not be appropriate. This step may not be necessary if the gasification reactions are limited to steam reformation. Nevertheless, the system was designed to provide this capability.

Solid Waste Gasification (Loops SG, PR and CO). Decomposition of the organic content of solid waste materials transferred to Column A may be achieved by any combination of three separate chemical processes: steam gasification, pyrolysis, and combustion. Process flow diagrams for these three gasification methods are shown in Figures 8.12 - 8.14, respectively. These processes may be employed separately, or in sequential or concurrent combinations. The major challenge in the gasification step is to discover an exact set of the operating conditions (duration, temperature, steam flow rate, air flow rate etc.) that provides an overall maximum capacity for waste conversion and resource recovery, with a corresponding minimum equivalent system mass.

The system was designed to implement steam reformation as the primary gasification mechanism, with the option for char reduction by pyrolytic and combustion methods. To date, only steam reformation experiments have been conducted using this apparatus, and therefore only this operation is described. To initiate ambient pressure steam reformation, steam generator heat-up is commenced while the temperature of column A is slowly raised using the two column-A-heaters to evaporate entrapped moisture. For successful steam gasification, it is desirable to employ the maximum possible heating rate of the column. Currently the achievable heating rates are in the range of 30-35°C/min. The nominal steady state operating temperature of the column is 750 °C. Column A is maintained at this temperature for a period of up to 80 minutes. (This may change as the result of further work.)

Steam is supplied to the gasification reactor at approximately 100 °C from the steam generator. The system is designed to provide enough steam to

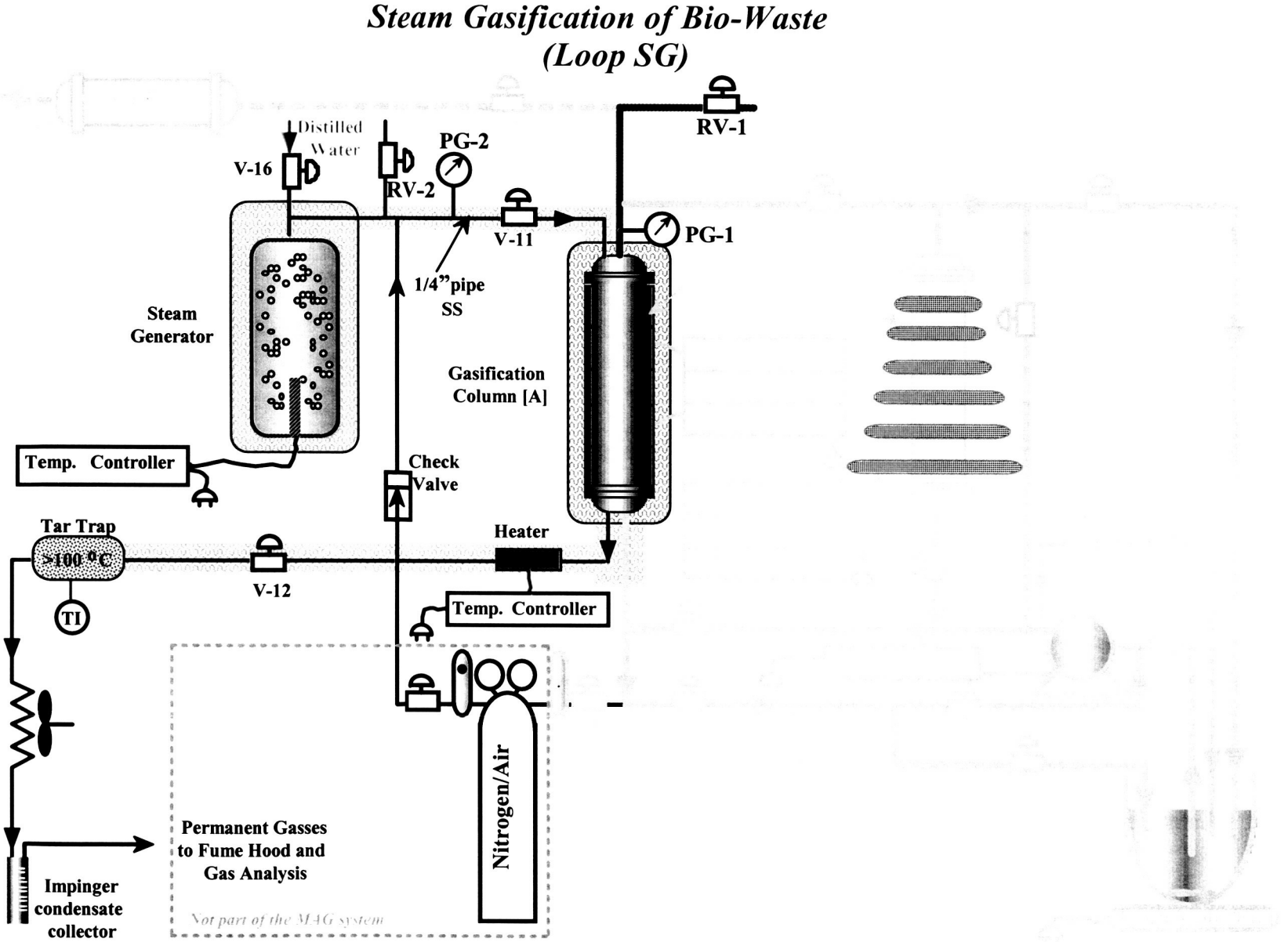

Figure 8.12. Magnetically Assisted Gasification by Steam Reformation - Loop SG.

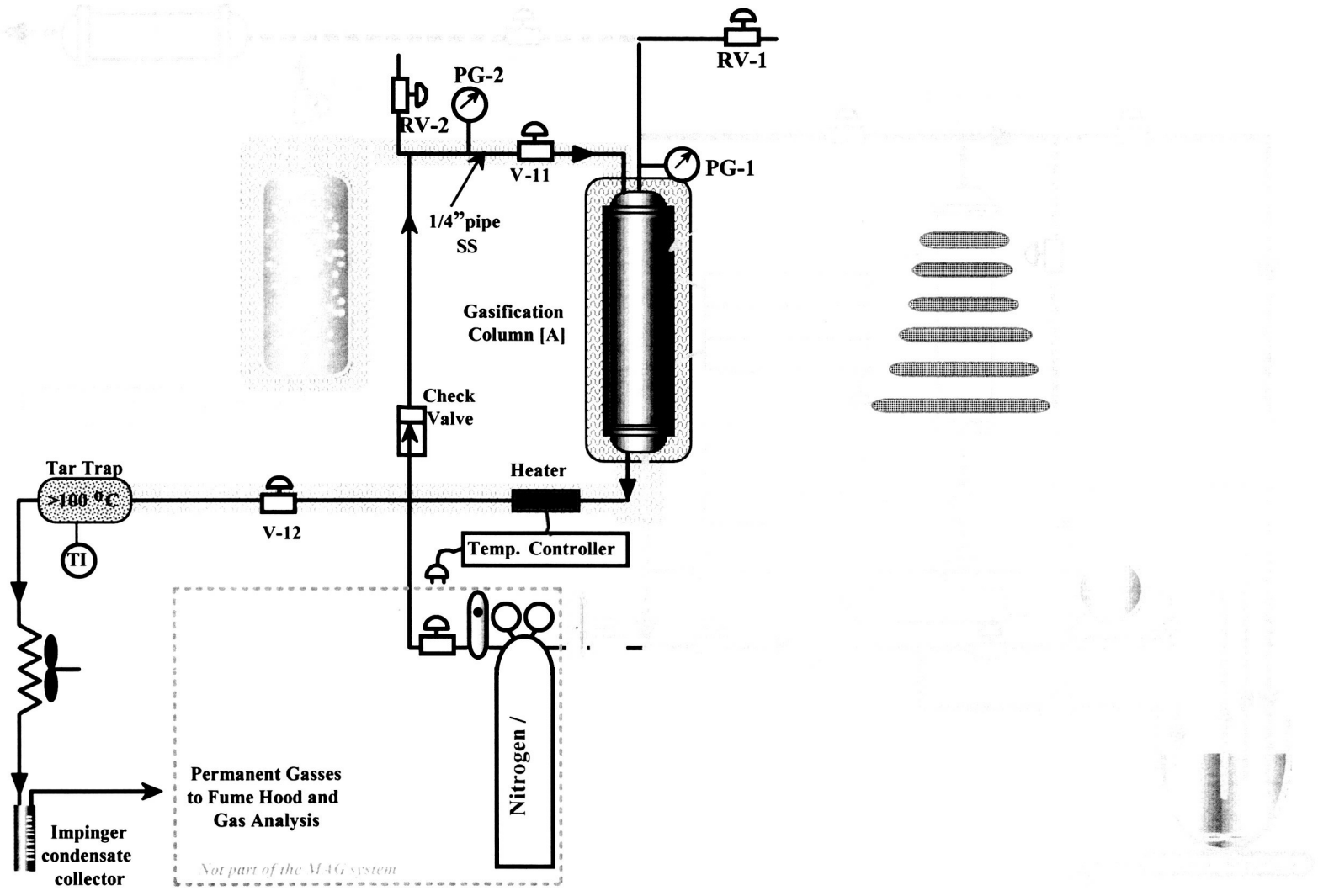

Figure 8.13. Pyrolysis of Char in Gasification Reactor - Loop PR.

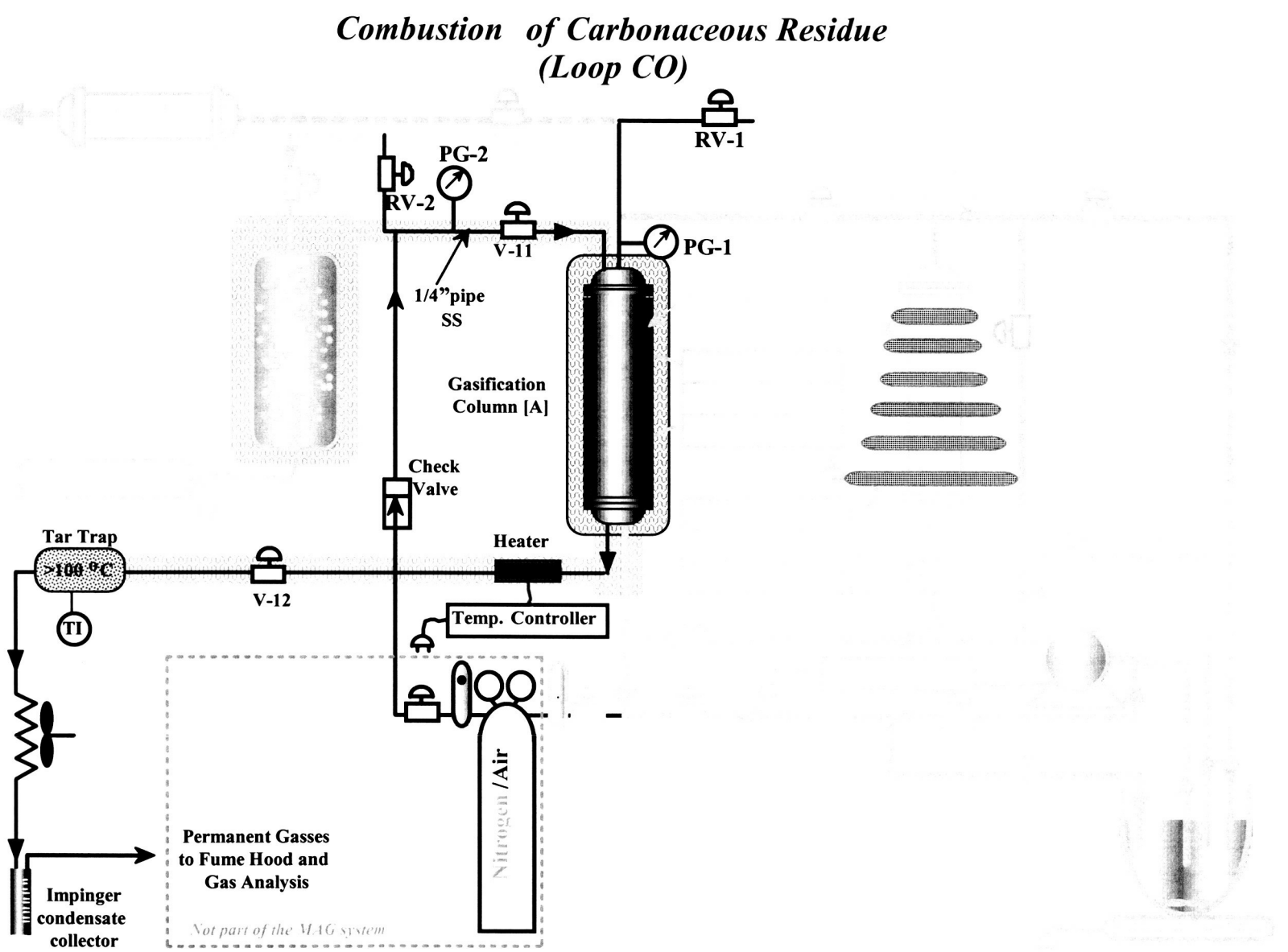

Figure 8.14. Char Combustion in Gasification Reactor - Loop CO.

maintain 20:1 steam to carbon ratio during the entire steam reforming operation. Future studies will explore the effect of substantially lower steam to carbon ratios, which can potentially reduce power requirements. During the steam gasification step, N_2 is also introduced with the steam to assure a positive gas flow through the system at all times and to prevent any premature combustion reactions.

Pyrolysis and combustion reactions within the MAG apparatus have yet to be investigated. With respect to the latter, It should be noted that combustion is an exothermic process and therefore steps must be taken to maintain stable temperatures within the bed. If the heat of combustion is sufficient, the heaters may be de-energized, thereby allowing the reactions to proceed autothermally. If this results in reactor temperatures which are too high, the heat of combustion can be modified by control of the oxidant flow. Under conditions in which the heat of combustion is insufficient to maintain reactor temperature, the column A heaters can be operated at reduced power, and then incrementally increased as the mass of carbonaceous residue diminishes.

An unmoderated combustion step represents a risk for the Co catalyst, which can be readily oxidized under these operating conditions. As such, the use of an oxidation gasification step for the process requires careful experimental investigation. Regeneration of the catalyst during the final stage of the steam gasification operation may be possible by introducing a small stream of H_2. Alternatively, it may be desirable to introduce a small amount of oxygen into the steam feed during the steam gasification step to improve the rate of gasifcation and minimize char and tar formation, rather than to perform a separate combustion step. Preliminary analysis indicates that a thermodynamic state which is not favorable for the formation of cobalt oxide is maintained as long as carbon remains in the reactor for oxygen levels up to 2% in the steam feed and temperatures in excess of ~150 °C.

Ash Removal (Loop ASh). Assuming complete gasification of the organic constituents of the solid waste in the reactor, only inorganic non-carbonaceous residue (ash) will remain in a state of dispersal throughout the intergranular spaces within the ferromagnetic catalyst bed. An Ash Removal step (Figure 8.15) is therefore required to prevent the gradual accumulation of residue inside the reactor. Following steam gasification, the reactor is allowed to passively cool

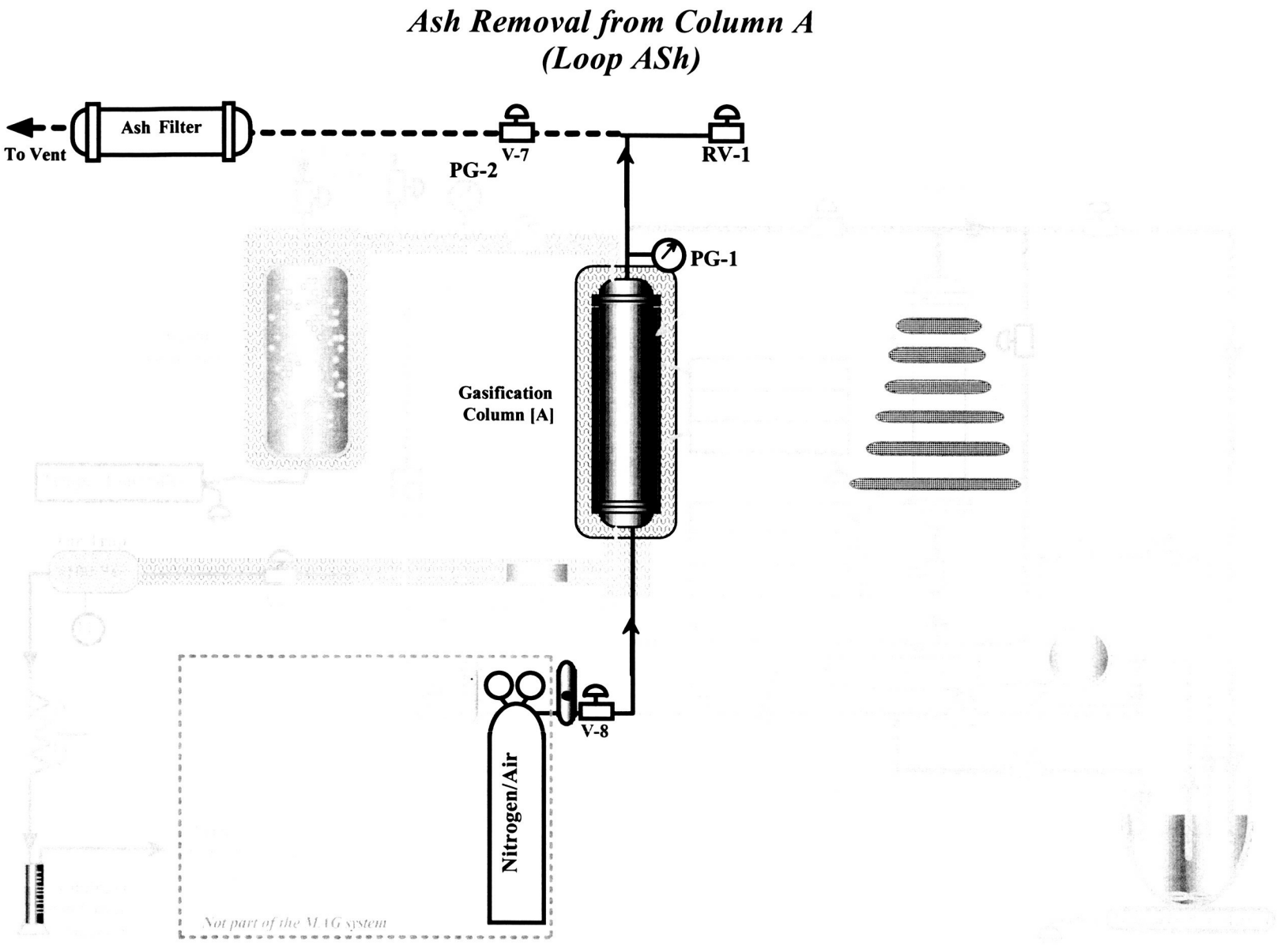

Figure 8.15. Post-Gasification Ash Removal from the Reactor - Loop ASh.

to ambient conditions. A gas flow path is then established through the reactor from bottom to top and on to the ash filter. Air or nitrogen flow is introduced through the reactor and the flow is raised to a level above the minimum fluidization velocity for the catalytic media. Due to very large difference in density and particle size between ash and the cobalt catalyst, the established flow rate is well beyond the maximum fluidization velocity for ash. Hence, drag forces induced by the gas flow transport this material out of the reactor and into the ash collection filter. In a microgravity or hypogravity application, magnetic forces acting upon the ferromagnetic catalyst oriented toward the distributor plate provide the opposing force required for fluidization of the catalytic media, while the non-magnetic ash is removed pneumatically from the reactor.

Simultaneous Gasification and Filtration (Loop SG/FB). Due to the dual column design of the MAG demonstration unit, it is possible to perform both solid waste filtration and gasification steps simultaneously. Concurrent filtration-gasification operations are illustrated in Figure 8.16. Complete isolation of the gasification operation from the filtration process is accomplished by closing valves V-3, V-4 and V-5.

Future Design Considerations. The MAG hardware described above was designed and assembled as a test-bed with which to conduct further research into magnetically assisted gasification of solid waste materials. This initial design, assembly, and commissioning exercise has helped to identify several possible design improvements which might be incorporated into future microgravity capable systems which may reduce energy use and equivalent system mass. For example, In the original conceptual design, it was envisioned that the magnetic field would be used to consolidate the magnetic media during the filtration step. While this can still be effected if desired, it is also possible to save energy by removing the field during this step and allow the filtration media to be retained as a packed bed by a retainer screen. A magnetic field would still be required in microgravity to expand and retain the media during fluidized bed gasification and ash removal steps. The dual column configuration employed in the current system may also be useful in future systems, but perhaps with two identical 'hot systems', each capable of filtration and gasification. Thus, while one column is loading (in filtration mode), the other column could be performing gasification reactions. This

Simultaneous Assisted Gasification and Filtration (Loop SG/FB)

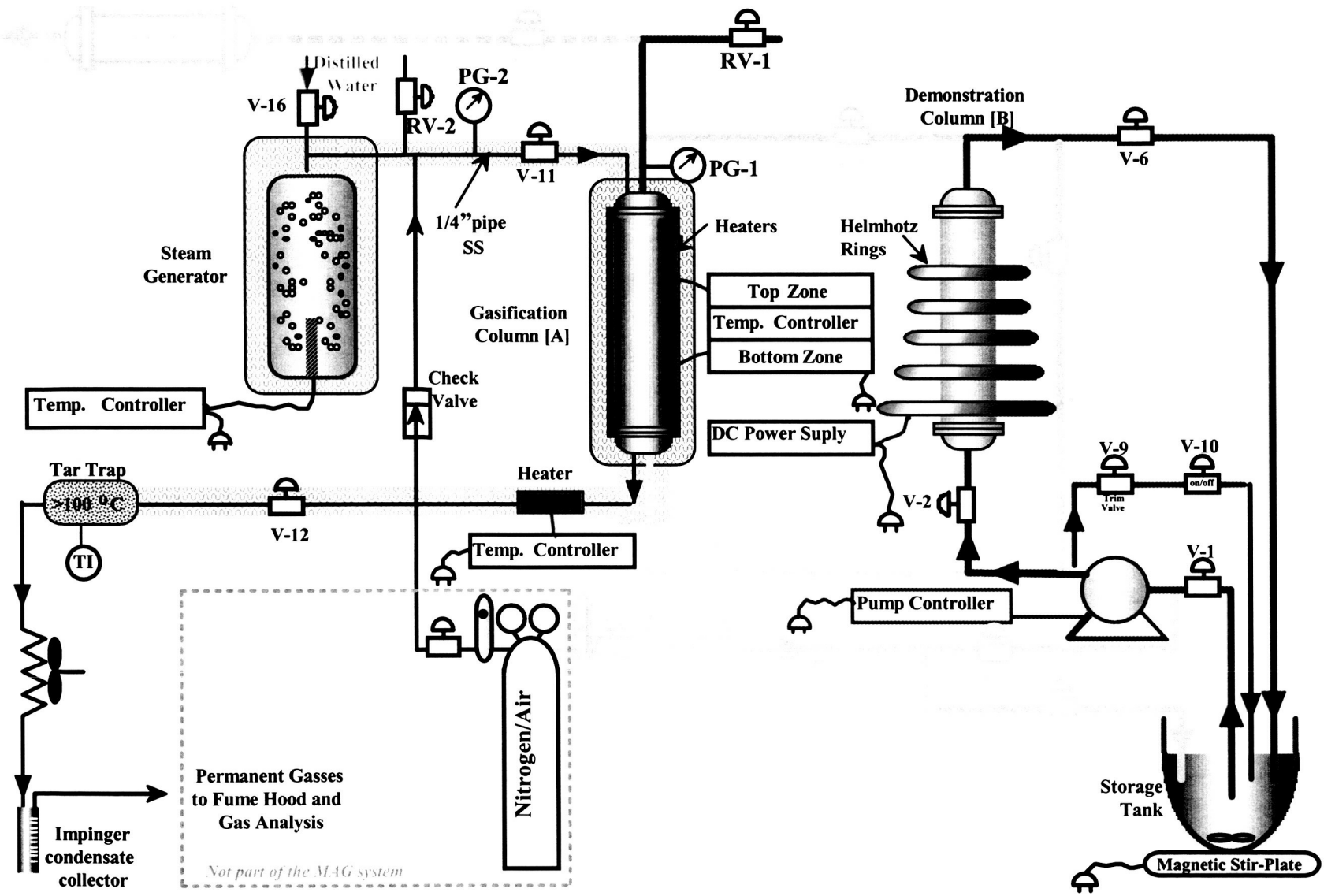

Figure 8.16. Simultaneous Filtration and Gasification - Loop SG/FB.

could provide the basis for continuous or semi-continuous operation and would eliminate the requirement for transfer of solids between columns.

8.2 Magnetically Assisted Gasification Hardware Operations. The MAG hardware described above can be operated in four primary modes: [1] filtration of solid wastes from a recirculating aqueous suspension under visual observation in the 'cold column', [2] filtration of solid wastes using the ferromagnetic catalyst bed in the 'hot column', [3] steam reformation (or alternatively pyrolysis or combustion) of solid wastes in the gasification reactor, and [4] ash removal and collection.

Filtration of solid waste using ferrite impregnated polymer beads within the clear plastic column allows for the direct visual observation of the magnetically assisted filtration process. The ability to magnetically control filter media was one of the important research objectives in this work. This can be conveniently demonstrated in the plastic column. Magnetic force, resulting from DC electric current flowing through a series of equally spaced Helmholtz coils, serves to consolidate the magnetic media into a packed filter bed, which would otherwise be in a fluidized state under the up-flow conditions imposed by the recirculating aqueous stream. The number of turns in each electromagnet, the spacing between magnets, and the applied currents were chosen to produce a nearly constant axial magnetic field gradient pointing downward in the direction of the distributor plate and spanning the height of the bed of filter media.

To conduct Magnetically Assisted Filtration, the following sequence of events occurs. With the magnetic coils de-energized, the solid waste stream flows from a well stirred holding tank into the bottom of the cold column at a rate sufficient to fluidize the filter media. By design, this rate corresponds to the maximum pump setting. Next, the Helmholtz coils are energized sequentially in pairs using three power switches. Over an ~10 second period, the initially fluidized filter media compacts into a consolidated bed. The pump flow rate is then adjusted to a lower flow rate for efficient filtration (nominally 25% of the maximum pump setting). When filtration is complete (after approximately 30 minutes) the trapped solid waste can be transferred to the gasification reactor. This is accomplished by first diverting flow to the bottom of the reactor and adjusting valve positions to allow the reactor volume to fill with water and purge through the tubing

at the top of the reactor and on to the waste tank. When the reactor is full of water, flow is again established through the filtration media. Valves are then switched to route the effluent from the filtration column toward the top of the gasification reactor. At this point, the direction of flow is from top to bottom through the catalyst bed within the reactor, with the effluent stream returning to the recirculation pump which now bypasses the solid waste holding tank.

The magnetic coils remain energized during the complete filtration event and also while the reactor is filled with water, thereby retaining the trapped solid waste within the consolidated filter media. Now, the magnetic force is removed by de-energizing the pairs of electromagnets simultaneously at the main coil power switch. Pump flow is then set to its maximum setting, allowing the ferrite impregnated media within the filtration column to fluidize and thereby release the smaller and lighter entrapped solid waste particles for transfer to the steam reformation reactor. This operation produces a concentrated slug of solids which are quickly delivered to the 'hot column' and retained within the catalyst bed. By adjusting the appropriate valves, the waste tank is bypassed during this transfer and water recirculates directly between the filtration column and the reactor. Any suspended matter which is not immediately trapped in the second column may be captured during subsequent passes through the reactor. When adequate transfer has been achieved (typically < 5 minutes), the pump is turned off and the valve at the bottom of the cold column is closed. This prevents the water retained inside the cold column from draining.

The presence of two columns is not required, however, employment of the plastic column does facilitate observation and further investigations of magnetically assisted fluidization and filtration phenomena. Filtration can occur directly within the reactor column, thus eliminating the need for solid waste transfer from the cold column to the gasification column. Solid waste collection in the 'hot column' using the ferromagnetic catalyst as filter media is configured to occur in the down-flow direction. This is accomplished by diverting flow through a bypass loop around the plastic column. Flow exiting the bottom of the reactor recirculates back to the waste tank. As for filtration in the plastic column, the pump flow rate is reduced to ~25% of its maximum setting. When filtration is complete (after ~30 minutes), the pump is turned off.

Prior to steam gasification of the solid waste, the bulk of the water remaining in the reactor is first gravity drained from the bottom of the reactor to the waste holding tank. Make-up air enters the top of the reactor through the holding tank return line, which has been repositioned above the liquid phase. This operation is typically completed within 10 minutes. (Clearly, a replacement for gravity drainage must be incorporated into future systems if full microgravity capability is to be achieved).

Following drainage, all valves to the reactor are closed, thereby isolating the gasification section from the rest of the system. The two high temperature valves are then opened to allow steam to enter the reactor and steam and gasification reaction product gases to exit. A nitrogen flow of ~100 cm^3/min is established in parallel with steam flow to assure a positive gas flow through the reactor at all times. The steam generator temperature controller is set to 120 °C as is the temperature controller for the heaters on the exit piping from the reactor. Both the top and bottom reactor heater controllers are set to a temperature in the range between 100-250 C. While the steam generator comes up to temperature, residual water trapped within the catalyst bed and the reactor plumbing is driven off. Once steady state steam generation / condensate collection conditions are established, the reactor temperature controllers are set to the desired process gasification temperature (typically >700 °C). The reactor heaters rapidly achieve the process temperature, typically both reaching the set point within 20 minutes.

Under these conditions, operation of the gasification reactor may proceed for as long as the boundaries of the particular experiment require, with the upper time limit ultimately determined by the amount of water initially present within the steam generator and the rate at which it is injected. Starting with a full steam generator (at room temperature), and operating at a 10-13 % power setting, such that condensate is collected at a nominal rate of 9 g/min, the steam generator can maintain this rate for ~2 hours. Following completion of the gasification process, the reactor heaters are turned off. After ~60 minutes the steam generator is also turned off (i.e., when the reactor has cooled to below 500 °C).

The final step in the integrated MAG process operation is the air-fluidized bed removal of ash from within the gasification reactor. This is accomplished after the reactor has cooled to room temperature. The nitrogen flow is discontinued and

the high temperature valves are closed. The compressed air valve is then opened to the bottom of the reactor and the exit valve at the top of the reactor is opened which directs air flow to the ash filter. A compressed air flow of > 6 L per minute is established through a flow regulator. This flow rate is sufficient to fluidize the media in the reactor. Entrained ash is carried out of the reactor volume and collected in the ash trap. After ~10 minutes of fluidization, the ash is sufficiently removed. The reactor is now ready to be used for the next gasification experiment.

Due to the two-column configuration of the first generation MAG hardware, it is possible to filter solid waste via the 'cold column' concurrently with gasification reactions in the 'hot column'. This results from our desire to observe and visually demonstrate magnetic control methods as they apply to both filtration and fluidization. However, based upon our limited experience to date, it may be desirable to incorporate separate filtration and gasification systems into future generations of MAG hardware. Indeed, since the gasification step requires substantially more time than is required for filtration, it is possible that a single 'cold' filtration column could support several reactors. This, however, would be highly dependent upon mission specific solid waste processing requirements.

8.3 MAG Hardware Commissioning Tests.

Due to the lengthy process of development of the necessary enabling technologies and the design and assembly of the first generation MAG hardware, only a limited number of preliminary gasification experiments were conducted prior to the end of the grant performance period. These initial commissioning or shake-down tests were conducted for the purposes of familiarization with the operational characteristics of the apparatus and for system de-bugging. However, continuation funding has been awarded through a second grant and it is anticipated that substantial progress will be made over the next three years.

Following assembly, the MAG apparatus was sequenced through the full range of Magnetically Assisted Gasification processes, including: magnetically assisted filtration of solid waste from a recirculating aqueous suspension, fluidization and transfer of solids to the gasification reactor; gasification of the solid

waste via high temperature steam reformation, and removal and collection of ash via gas-solid fluidization following reactor cool-down. For convenience, metallic cobalt supported on porous silica beads was employed as the ferromagnetic media within the gasification reactor. As expected, these initial commissioning runs indicated the necessity of minor design changes and also clarified operational constraints. This lead to the addition of valves and minor re-plumbing, clarification of the correct sequencing of valve states required to perform each of the process tasks; the redesign and assembly of the end-caps on the filtration column; and the replacement of a faulty reactor heater fuse.

In this first series of shake-down runs, steam reformations of wheat straw, canned dog food, and dog feces were performed in separate tests. Magnetically Assisted Filtration within the 'cold column' and transfer of the solids to the gasification reactor was achieved without difficulty. Gasification reactions were conducted at 700 °C for 30 minutes, with the Steam Generator (SG) set at 101 °C. Following reactor cool-down, ash removal and collection by fluidization and down-stream filtration was also performed efficiently.

In these commissioning tests, the primary indication of reactor performance was gauged in terms of the residue which remained within the reactor following the gasification runs. These consist of carbonaceous residue (char) and non-carbonaceous inorganic substances (ash). The dark color and carbonaceous nature of a substantial fraction of the solids collected during ash removal suggested that the initial reaction conditions were inadequate. This was confirmed following disassembly of the gasification reactor following steam reforming runs for each of the solid waste types. Large amounts of consolidated char pieces were observed in place on top of the catalyst bed. Photographs of these are presented in Figures 8.17 and 8.18. While, minimization of char production is an essential goal for efficient gasification, these results indicate that the combination of pyrolytic and steam reforming reactions which occur under these operating conditions may be employed to produce carbon-based materials which might be used as sorbents in air and water purification. Since many of the most effective carbon-based sorbents are 'steam activated', this is not an unreasonable stretch of the imagination. Thus, if resource recovery is the over-riding aim, reactor operations may be optimized for the production of these materials.

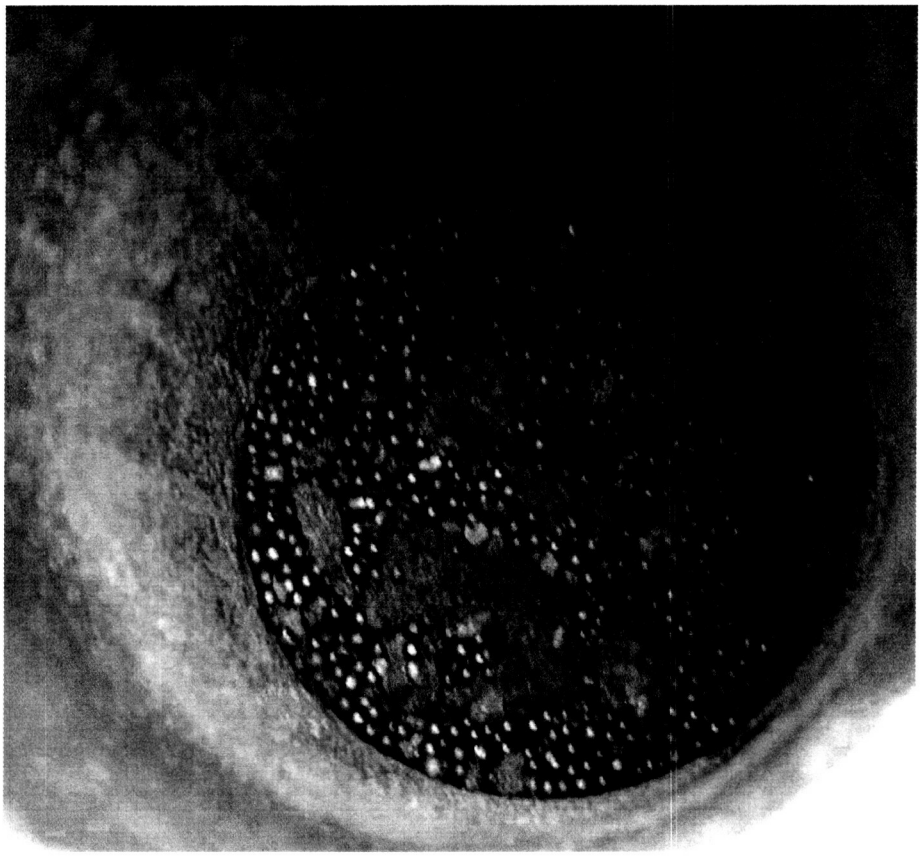

Figure 8.17. Top View Inside Gasification Reactor after Disassembly.

Figure 8.18. Consolidated Char Pieces Recovered from Gasification Reactor.

The photo in Figure 8.17 also indicates the onset of corrosion of the interior stainless steel surfaces of the reactor. Clearly, even stainless steels are vulnerable when exposed to steam at temperatures of ~ 700 °C. With regard to future experiments, it is highly likely that the gasification reactor housing will have a limited lifetime. Since operation of the system occurs at ambient pressure, however, the safety concerns regarding reactor failure are relatively minor. Improved resistance to corrosion may be achieved by coating the stainless steel interior, or replacement by a ceramic material with good thermal conductivity.

The catalytic media were removed from the reactor and dried in air at 110 °C. These are shown in Figure 8.19. A small sample of the media was thermally processed to quantify the extent of char coating on the catalytic surfaces. The sample was heated in air to a final temperature of 500 °C and held there for 30 minutes to burn off the char. Unavoidably, the cobalt metal catalyst located on the was also oxidized during this step, thus necessitating a subsequent reduction to regain the metallic state. To achieve this, the catalyst was exposed to hydrogen in a tube furnace with a heating rate of 10 °C/min up to an end-point temperature of

Figure 8.19. Beakers Filled with Used Ferromagnetic Catalyst after Drying at 110 °C. Foreground: Sample of Media in Vial Collected Prior to Gasification, and Post-Gasification Sample within Ceramic Boat.

900 °C, and held there for180 minutes. An estimate was then made of the amount of char coating on the beads based upon weight loss during combustion, corresponding to ~15.2 g of carbon present on the ~1.9 L of Catalyst. In this calculation, the amount of cobalt in the catalyst was assumed to be essentially unchanged from that of the original media. This assumption is supported by a thermodynamic analysis of the carbon/water/cobalt system, which indicates that oxidation of cobalt should not occur at reactor temperatures above ~200 °C, so long as carbon is present. This analysis also emphasizes the importance of timing the gasification runs such that the catalyst is not unnecessarily exposed to high temperature steam once the organic components of the solid waste, and any chars which have formed during processing are gasified.

A second series of shake-down magnetically assisted gasification runs were performed using wheat straw. As in the previous tests, filtration and ash collection steps were achieved without incident. The gasification reactor was operated at the somewhat higher temperature of 775 °C. This is significantly above the recommended temperature range for the 304 stainless steel housing (600-650 °C). It can therefore be expected that the useful life for the reactor may be significantly shortened while operating at higher temperatures. The degradation appears to be confirmed by the presence of corrosion on the inside walls of the reactor just above the catalyst bed. This location corresponds to the position of the upper heating element, the region which experiences the greatest internal temperature. Two experiments were performed at this temperature, each for a period of 30 minutes, with the SG set at 101 °C, as in the previous reactor runs. Again, dark char powder was observed in the ash trap following gasification.

Based upon these results, subsequent reactor runs would be conducted using higher steam injection rates, and longer reaction times. However, before further experiments were performed, the system was modified to attain a more precise degree of control over the steam injection rate. Up to this point, the steam generation (SG) system had employed a Proportional Integral and Derivative (PID) controller operating in the PI mode. By design, the thermocouple for the SG was sandwiched between the external wall of the SG vessel and the heater, with a layer of metal sheeting separating the thermocouple from direct contact with the heating elements. By controlling the temperature of the SG at this point, it was hoped that, at steady state, the steam output of the well-insulated SG would be

adequate for the gasification process. However, from the relatively small amount of condensate which was collected, and the variable rate of collection that was observed, it became apparent that this type of control was inadequate.

Analysis of this problem indicated that, if the steam generator could be heated at a fixed power input level, since it is well insulated, a direct relationship between the amount of water boiling at 100 °C (at 1 atm pressure), and the power level input to the SG would result. One approach considered to effect this type of control was to eliminate the PID controller and to heat the SG directly though a pair of variacs (one for each leg of the 240 VAC power input). By manually adjusting the variac settings, the SG heating power level could be set exactly. This approach, however, held the potential for a dangerous run-away state if the SG should ever inadvertently run dry. In order to retain the level of safety afforded by feedback control, while at the same time effecting exact power input, the PID control parameters were altered to force the controller to provide a constant percent power level.

To maintain a given percent power level, the controller uses time proportional control, where the power stays on for a set percentage of a given time interval. By keeping the temperature set point within an intentionally narrow proportional band setting which is well above the actual SG temperature, whilst setting the maximum percent power parameter at the desired heating level, regulation of a constant percent power level was achieved. As long as the bottom of the proportional band for the set-point temperature was above the actual steady state SG temperature for the percent power level setting, the controller would continue to output this constant percent power level. Following these modifications, the operation of the SG was characterized at steady state for three separate percent power levels, each of which would produce a significantly higher steam injection rate than for all previous testing.

Using the improved control capability, a char gasification run was performed at 775 °C for 80 minutes using a steam injection rate of ~ 4 g/min. This experiment was performed without filtering any further solid waste, with the intent of removing the ~15.2 g of char remaining on the surface of the catalytic media. Following gasification, the ash removal process produced no indication of char carry-over during this step.

Based upon previous work, it was estimated that a specific steam injection rate of 0.7 g/min per gram of dry wheat straw was required to completely gasify the solids, given sufficient time and temperature. To test this estimate, a solid waste stream containing 10 g of wheat straw was fed directly into the bottom of the reactor. Steam reformation was conducted at a steam injection rate of ~ 8 g/min, twice that of the previous run and in slight excess of the estimated requirement. The product removed during the ash removal step, however, was again black, indicating substantial char formation. It was hypothesized that while feeding the solid waste directly to the reactor from the bottom, most of the solid waste was trapped in a region that was not well heated during gasification. To prevent this, a bypass loop was added which allowed the solids containing process stream to feed directly into the top of the reactor. Following reconfiguration, a final test was performed. In this run, 10 g of wheat straw was filtered directly by the consolidated catalyst bed, with inflow into the top of the reactor. Gasification reactions were performed at 775 °C for 60 minutes, with a steam injection rate of ~ 9 g/min. As in the previous experiment, the dark coloration of solids removed from the gasification reactor during the ash removal step indicated significant char formation.

The reactor was then disassembled for the second time. A photograph of the reactor contents is shown Figure 8.20. As before, relatively large consolidated pieces of carbonaceous matter can be seen resting at the top of the catalyst bed. However, when removed from the reactor, these pieces crumbled to a fine powder before they could be separated from the ferromagnetic catalyst beads. This is in contrast to the carbonaceous solids collected during the first disassembly, which were much more robust. While char production under these reaction conditions is still evident, a significant difference between this and reactions conducted previously is the absence of a char coating on the surfaces of the ferromagnetic catalyst beads.

Because the preliminary gasification runs described above are essentially commissioning and familiarization experiments, it would be premature to begin drawing conclusions regarding efficacy of the first generation magnetically assisted gasification hardware. Much additional work will be required to identify the most efficacious operating conditions for resource recovery and gasification of

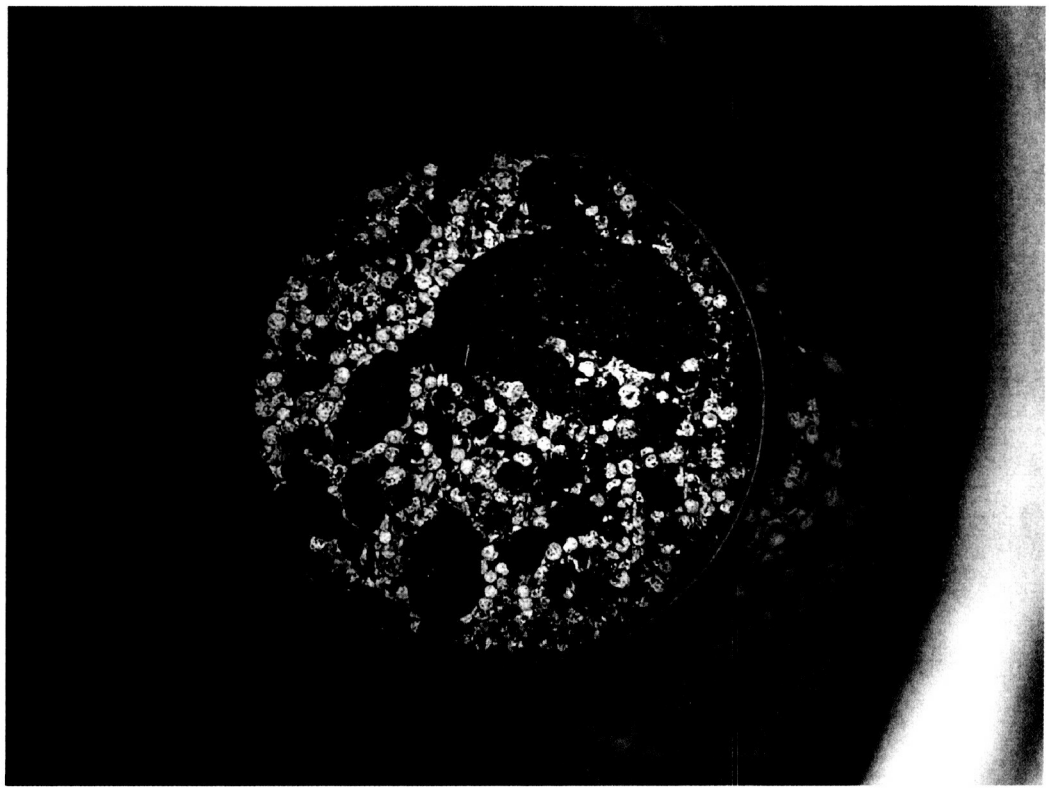

Figure 8.20. View inside top of reactor after second disassembly.

solid waste materials. Detailed parametric investigations must be conducted in which the effects of catalyst composition, reaction temperature, reaction time, steam temperature, steam injection rates, and solid waste composition are carefully documented. These experiments must compare the relative distributions of ash, char, tar, and gases produced under each set of conditions. It is probable that optimal reaction conditions will vary significantly, depending upon the mission specific solid waste treatment and resource recovery objectives which the MAG hardware is intended to implement. One set of conditions may be most favorable for the quantitative conversion of organics to CO_2 and H_2O, while another set of conditions may be employed to produce additional gases such as H_2 and CH_4, for use as propellants, or as reactants in the production of water from carbon dioxide, etc., and yet another set of operational parameters may result in the production of carbonaceous materials for employment as sorbents in air purification and water purification systems.

9. CONCLUSIONS.

During this three year effort, substantial progress has been made, particularly with respect to the development of magnetic materials, equipment, and methods to control fluidization and consolidation of granular ferromagnetic media for employment in microgravity and hypogravity environments. Novel high temperature capable ferromagnetic materials have been developed as catalytic fluidization media. Fortran coded electromagnet design software has been developed and employed in the construction of constant magnetic field gradient fluidization columns in both cylindrical and rectangular geometries. Magnetically controlled fluidization and filtration have been investigated in the laboratory. Two-dimensional computational fluid dynamics and related mathematical models have been developed which describe these phenomena. In two series of flight experiments, fluidization has been demonstrated in the microgravity environment using the magnetic field gradient based techniques developed under this program.

Comparative studies were conducted which examined the relative merits of pyrolysis and steam reformation for the gasification of solid waste materials. In these studies, solid waste decomposition byproducts were characterized as: inorganic residue (ash), carbonaceous residue (char), volatilized high molecular weight organics (tar), water, and simple gases (CO, CO_2, CH_4, N_2, etc.). Pyrolysis and steam reformation runs were conducted over a range of temperatures and other reaction conditions using solid waste materials that included paper, inedible plant biomass, and feces. The objective of this reaction engineering component of the project was to identify conditions under which all inorganic residue remained within the fluidized bed as ash, the production of char and tar was minimized, and the production of water and potentially useful gases was maximized. Based upon these criteria, ambient pressure steam reformation was selected for further study.

Fully integrated magnetically assisted gasification hardware was designed and assembled to facilitate further investigation of the novel solid waste destruction methodology. The system was designed to operate under ambient pressure conditions at temperatures up to 800 °C. Primary components of the system include an onboard steam generator, high temperature fluidization column and reactor, and an ambient temperature filtration column. A separate filtration

column, composed of transparent acrylic polymer, was included in the apparatus so that visual observation of the filtration process was possible. This column can also be utilized to visually demonstrate gradient magnetically assisted fluidization under ambient temperature conditions. During commissioning of the apparatus, minor problems were identified and corrected. Initial ambient temperature steam reformation reactor runs were performed over a range of temperatures and other reaction conditions. While the feasibility of magnetically assisted solid waste gasification was clearly demonstrated, experimental results also indicated that a great deal of additional work will be required. Because of the relative immaturity of this technology, equivalent system mass calculations were not performed. However, a second three-year grant has been awarded. This will facilitate the advancement of the magnetically assisted gasification technology to a much higher state of readiness.

REFERENCES

1. Swallow, K.C., Killilea, W.R., Hong, G.T., and Lee, H.-W., Behavior of Metal Compounds in the Supercritical Water Oxidation Process, SAE Technical Paper Series No. 901314, presenated 20th Intersociety Conference on Environmental Systems, Williamsburg, VA, July 9-12, 1990.
2. Webley, P.A., Holgate, H.R., Stevenson, D.M., and Tester, J.W., Oxidation Kinetics of Model Compounds of Metabolic Waste in Supercritical Water, SAE Technical Paper Series No. 901333, presenated 20th Intersociety Conference on Environmental Systems, Williamsburg, VA, July 9-12, 1990.
3. Hall, J.B., Jr., and Brewer, D.A., Supercritical Water Oxidation: Concept Analysis for Evolutionary Space Station Application, SAE Technical Paper Series No. 860993, presented 16th Intersociety Conference on Environmental Systems, San Diego, CA, July 14-16, 1986.
4. Armellini, F.J., and Tester, J.W., Salt Separation During Supercritical Water Oxidation of Human Metabolic Waste: Fundamental Studies of Salt Nucleation and Growth, SAE Technical Paper Series No. 901313, presented 20th Intersociety Conference on Environmental Systems, Williamsburg, VA, July 9-12, 1990.
5. Fisher, J.W. and Abraham, M.A., Particle Size Effect on Supercritical Water Oxidation of Polystyrene Beads. SAE Technical Paper Series No. 941399, presented at 24th International Conference on Environmental Systems, Friedrichshafen, Germany, June 1994
6. Fisher, J.W., Pisharody, S.A., and Abraham, M.A., Particle Size Effect on Supercritical Water Oxidation - Wheat Straw Particles, SAE Technical Paper Series No. 951739, presented at 25th International Conference on Environmental Systems, San Diego, CA, July 10-13, 1995.
7. Hong, G.T., Borchers, B., Pisharody, S., and Fisher, J., A Supercritical Water Oxidation Unit for Treating Waste Biomass, SAE Technical Paper Series No. 961560, presented at 26th International Conference on Environmental Systems, Monterey, CA, July 8-11, 1996.
8. Lighty, J. S., Burton, B., Sirdeshpande, A., and Inkley, D., Waste Incineration for Resource Recovery in a Bioregenerative Life Support System, SAE Technical Paper Series No. 972429, presented at 27th International Conference on Environmental Systems, Lake Tahoe, NV, July 1997.

9. Fisher, J.W., Pisharody, S., Wignarajah, K., Lighty, J.S., Burton, B., Edeen, M., and Davis, K.A., Waste Incineration for Resource Recovery in a Bioregenerative Life Support System, SAE Technical Paper Series No. 981758, presented at 28th International Conference on Environmental Systems, MA, July 1998.
10. Pisharody, S., Fisher, J.W., Moran, M, and Tliemat, M., Incineration of Inedible Biomass in a Regenerative Life Support System - Development Efforts at NASA Ames Research Center, SAE Technical Paper Series No. 2000-01-2282, presented 30th International Conference on Environmental Systems, Toulouse, France, 2000.
11. Fisher, J.W., Pisharody, S., Moran, M.J., and Tliemat, M., Incineration of Inedible Biomass in a Regenerative Life Support System - Update of Development Activities at ARC, SAE Technical Paper Series No. 2001-010-2344, presented 31st International Conference on Environmental Systems, Orlando, FL, 2001.
12. Lee, C. M., Davis, K.A., Seeley, R., Sarofim, A.F., Burton, W., Overacker, D.W., Eddings, E.G., and Lighty, J.S., Catalytic Reduction and Oxidation of Biomass Combustor Effluent, SAE Technical Paper Series No. 1999-01-2185, presented at 29th International Conference on Environmental Systems, CO, July 1999.
13. Serio, M.A., An Improved Pyrolyzer for Solid Waste Resource Recovery in Space, SAE Paper 2002-01-2402, presented at 32nd International Conference on Environmental Systems, San Antonio, July 2002.
14. Serio, M.A., Kroo, E., Bassilakis, R., Wojtowicz, M.A., and Suuberg, E.M., A Prototype Pyrolyzer for Solid Waste Resource Recovery in Space, SAE Paper 2001-01-2349, presented at 31st International Conference on Environmental Systems, Orlando, July 2001.
15. Serio, M.A., Chen, Y., and Wojtowicz, M.A., Pyrolysis Processing for Solid Waste Resource Recovery in Space, SAE Paper 2000-01-2286, presented at 3oth International Conference on Environmental Systems, Tolouse, France, July 2000.
16. Encinar, J.M., Gonzalez, J.F., and Gonzalez, J., Fixed-Bed Pyrolysis of *Cynara cardunculus L.* Product Yields and Compositions, *Fuel Process. Technol.* 68, 209-222, 2000.
17. Minkova, V., Razvigorova, M., Bjornbom, E., Zanzi, R., Budinova, T., and Petrov, N., Effect of Water Vapor and Biomass Nature on the Yield and

Quality of Pyrolysis Products from Biomass, *Fuel Process. Technol.* 70, 53-61, 2001.

18. Encinar, J.M., Beltran, F.J., Ramiro, A., and Gonzalez, J.F., Pyrolysis/Gasification of Agricultural Residues by Carbon Dioxide in the Presence of Different Additives: Influence of Variables, *Fuel Process. Technol.* 55, 219-233, 1998.
19. Banyasz, J.L., Li, S., Lyons-Hart, J.L., and Shafer, K.H., Gas Evolution and the Mechanism of Cellulose Pyrolysis, *Fuel* 80, 1757-1763, 2001.
20. Davidsson, K., *Biofuel Pyrolysis and On-Line Alkali Measurements*, Thesis, Goteborg University, Goteborg, Sweden, 2002.
21. Brown, A.L., Dayton, D.C., and Daily, J.W., A Study of Cellulose Pyrolysis Chemistry and Global Kinetics and High Heating Rates, *Energy & Fuels* 15, 1286-1294, 2001.
22. Ma, S., Lu, J., and Gao, J., Study of the Low Temperature Pyrolysis of PVC, *Energy & Fuels* 16, 338-342, 2002.
23. Liou, T.-H., Chang, F.-W., and Lo, J.-J., Pyrolysis Kinetics of Acid-Leached Rice Husk. *Ind. Eng. Chem. Res.* 36, 568-573, 1997.
24. Lanzetta, M., Di Blasi, C., and Buonanna, F., An Experimental Investigation of Heat-Transfer Limitations in the Flash Pyrolysis of Cellulose. *Ind. Eng. Chem. Res.* 36, 542-552, 1997.
25. Kang, S., Optimization of Feedstock Composition and Pre-Processing for Composting in Advanced Life Support Systems, SAE Technical Paper 2001-01-2297, presented at 31st International Conference on Environmental Systems, Orlando, July 2001.
26. Yorio, N.C., Alazraki, M.P., Garland, J.L., and Ruffe, L.M., The Utilization of Recovered Nutrients From Composted Inedible Wheat Biomass to Support Plant Growth for BLSS, SAE Technical Paper 1999-01-2062, presented at 29th International Conference on Environmental Systems, Denver, July 1999.
27. Finger, B.W., and Strayer, R.F., Development of an Intermediate-Scale Aerobic Bioreactor to Regenerate Nutrients from Inedible Crop Residues, SAE Technical Paper Series No. 941501, presented at 24th International Conference on Environmental Systems, Germany, 1994.
28. Finger, B.W., and Alazraki, M.P., Development and Integration of a Breadboard-Scale Aerobic Bioreactor to Regenerate Nutrients from Inedible Crop Residues, SAE Technical Paper Series No. 951498, presented at 25th

International Conference on Environmental Systems, San Diego, CA, July 10-13, 1995.

29. Mackowiak, C.L., Garland, J.L., Strayer, R.F., Finger, B.W., and Wheeler, R.M., Comparison of Aerobically-Treated and Untreated Crop Residues as a Source of Nutrients in a Recirculating Hydroponic System, *Adv. Space Res.*, 18, 281-287, 1996.
30. Manukovsky, N.S., Kovalev, V.S., Zolotukhin, I.G., and Rygalov, V.Y., Biotransformation of Plant Biomass in Closed Cycle, SAE Technical Paper Series No. 961417, presented at 26th International Conference on Environmental Systems, Monterey, CA, July 8-11, 1996.
31. Strayer, R.F., Evaluation of Enzymatic Hydrolysis of CELSS Wheat Residue Cellulose at a Scale Equivalent to NASA's KSC Breadboard Project, SAE Technical Paper Series No. 93225, presented 23rd International Conference on Environmental Systems, Colorado Springs, CO, July 1993.
32. Strayer, R.F., and Cook, K., Recycling Plant Nutrients at NASA's KSC-CELSS Breadboard Project: Biological Performance of the Breadboard-Scale Aerobic Bioreactor During Two Runs, SAE Technical Paper Series No. 951708, presented at 25th International Conference on Environmental Systems, San Diego, CA, July 10-13, 1995.
33. Williams, D.W., Kull, R., and Schwartzkopf, S.H., Anaerobic Treatment of Organic Wastes from Controlled Ecological Life Support Systems, SAE Technical Paper Series No. 921272, presented 22nd International Conference on Environmental Systems, Seattle, WA, July 13-16, 1992.
34. Kunii, D.; and Levenspiel, O., *Fluidization Engineering*; Butterworth-Heinemann: Boston, 1991.
35. Atwater, J.E., Akse, J.R., Jovanovic, G.N., Wheeler, R.R., Jr., and Sornchamni, T., Porous Cobalt Spheres for High Temperature Gradient Magnetically Assisted Fluidized Beds, *Mater. Res. Bull.*, 38, 395-407, 2003.
36. Atwater, J.E., Akse, J.R., Jovanovic, G.N., and Sornchamni, T., Preparation of Metallic Cobalt and Cobalt-Barium Titanate Spheres as High Temperature Media for Magnetically Stabilized Fluidized Bed Reactors, *J. Mater. Sci. Lett.*, 20, 487-488, 2001.
37. Jovanovic, G.N., Sornchamni, T., Atwater, J.E., Akse, J.R., and Wheeler, R.R., Jr., Magnetically Assisted Liquid-Solid Fluidization in Normal and Microgravity Conditions: Experiment and Theory, submitted to *Powder Technol.*, April 2003.

38. Jovanovic, G.N., Pinto-Espinoza, J., Sornchamni, T., Reed, B., Wheeler, R.R., Jr., Atwater, J.E., and Akse, J.R., Development of Enabling Technologies for Magnetically Assisted Gasification of Solid Wastes, SAE Technical Paper 2003-01-2374, presented 33rd International Conference on Environmental Systems, Vancouver, BC, July 7-10, 2003.
39. Atwater, J.E., Akse, J.R., DeHart, J., Jovanovic, G.N., Sornchamni, T., Yoo, S., and Fisher, J.W., Magnetically Assisted Gasification of Solid Waste, SAE Technical Paper Series No. 1999-01-2183, presented 29th International Converence on Environmental Systems, Denver, July 12-15, 1999.
40. Jovanovic, G.N., Sornchamni, T., Espinosa, J.P., Atwater, J.E., and Akse, J.R., The Study of Magnetically Assisted Fluidization in Microgravity and Variable Gravity: Simulation and Experiment, presented 4th International Life Support and Biosphere Science Conference, Baltimore, August 6 - 9, 2000. (Abstract.)
41. Atwater, J.E., Jovanovic, G.N., Akse, J.R., Wheeler, R.R., Jr., Sornchamni, T., and Espinoza, J.P., Methods and Materials for the Control of Granular Media in Microgravity and Hypogravity for Magnetically Assisted Gasification (MAG) and Other Advanced Life Support Applications, presented Bioastronautics Investigators' Workshop, Galveston, TX, January 17-19, 2001. (Abstract.)
42. Pinto-Espinoza, J., Cruz-Fiero, C.F., and Jovanovic, G.N., Influence of Magnetic Forces in a Magnetically Assisted Fluidized Bed (MAFB): CFD-DPM Simulation, Experiment, and Theory, 7th International Conference on Circulating Fluidized Beds, Niagara Falls, Ontario, May 5-8, 2002. (Abstract.)
43. Sornchamni, T., Jovanovic, G., Atwater, J., Akse, J., and Wheeler, R., The Operation of Magnetically Assisted Fluidized Bed in Microgravity and Variable Gravity: Experiment and Theory, presented at the World Space Congress, October 10-19, Houston, Texas 2002.
44. Jovanovic, G.N., Sornchamni, T., Atwater, J.E., and Wheeler, R.R., Jr., Gradient Magnetically Assisted Liquid-Solid Fluidization in Normal and Microgravity Conditions, Paper No. 138g, presented AIChE Annual Meeting, Indianapolis, IN, November 3-8, 2002.
45. Jovanovic, G.N., Sornchamni, T., Atwater, J.E., and Akse, J.R., Mathematical Modeling of Micron-Size Particle Collection in a Gradient Magnetically Assisted Fluidized Bed, Paper No, 147d, presented AIChE Annual Meeting, Indianapolis, IN, November 3-8, 2002.

46. Sornchamni, T., *The Prediction of Voidage Distribution in a Non-uniform Magnetically Assisted Fluidized Bed: Theory and Experiment.* M.S. Thesis, Oregon State University, Corvallis, Oregon, 2000.
47. Espinoza, J.P., Dynamic Behavior of Ferromagnetic Particles in a Liquid-Solid Magnetically Assisted Fluidized Bed (MAFB): Theory, Experiment, and CFD-DPM Simulation, Doctoral Dissertation, Oregon State University, Corvallis, Oregon 2002.
48. Lee, C. M., Davis, K.A., Seeley, R., Sarofim, A.F., Burton, W., Overacker, D.W., Eddings, E.G., and Lighty, J.S., Catalytic Reduction and Oxidation of Biomass Combustor Effluent, SAE Technical Paper Series No. 1999-01-2185, presented at 29th International Conference on Environmental Systems, CO, July 1999.
49. Sirdeshpande, A. and Lighty, J.S., Kinetics of the Selective Catalytic Reduction of NO with NH_3 over CuO/γ-Al_2O_3, *Ind. Eng. Chem. Res.* 39, 1781-1787, 2000.
50. Anderson, T.B.and Jackson, R., A Fluid Mechanical Description of Fluidized Beds. Equations of Motion, *Ind. Eng. Chem. Fund.* 6, 527-539, 1967.
51. Jackson, R., *The Dynamics of Fluidized Particles*, Cambridge University Press, New York, 2000.
52. Anderson, T.B., and Jackson, R., *Computational Fluid Dynamics: The Basics with Applications*, McGraw-Hill, New York, 1995.
53. Levenspiel, O., *Chemical Reaction Engineering*; Wiley, New York, 1972.
54. Rosensweig, R.E., Fluidization: Hydrodynamic Stabilization with a Magnetic Field, *Science* 204, 57-60, 1979.
55. Rosensweig, R.E., Magnetic Stabilization of the State of Uniform Fluidization, *Ind. Eng. Chem. Fundam.* 18, 260-269, 1979.
56. Rosensweig, R.E.; Siegell, J.H.; Lee, W.K.; Mikus, T., Magnetically Stabilized Fluidized Solids, *AIChE Symposium Series* 77, 8-16, 1981.
57. Rosensweig, R.E., *Ferrohydrodynamics*; Cambridge University Press: New York, 1985.
58. Rosensweig, R.E.; Jerauld, G.R.; Zahn, M., *Continuum Models of Discrete Systems 4*; Brulin, O.; Hsieh, R.K.T., Eds.; North-Holland: New York, pp 137-144, 1981.
59. Rosensweig, R.E.; Zahn, M.; Lee, W.K.; Hagan, P.S., *Theory of Dispersed Multiphase Flow*; Meyer, R.E., Ed.; Academic Press, New York, pp 359-384, 1983.

60. Burns, M.A., and Graves, D.J., Continuous Affinity Chromatography using a Magnetically Stabilized Fluidized Bed, *Biotechnol. Prog.* 1, 95-103, 1985.
61. Burns, M.A., and Graves, D.J., Structural Studies of A Liquid-Fluidized Magnetically Stabilized Bed, *Chem. Eng. Comm.* 67, 315, 1988.
62. Siegell, J.H., Liquid-Fluidized Magnetically Stabilized Beds, *Powder Technol.* 52, 139-148, 1989.
63. Goetz, V., and Graves, D.J., Axial Dispersion in Magnetically Stabilized Fluidized Bed Liquid Chromatography Column, *Powder Technol.* 64, 81-92, 1991.
64. Chetty, A.S., Gabis, D.H., and Burns, M.A., Overcoming Support Limitations in Magnetically Stabilized Fluidized Bed, *Powder Technol.* 64, 165-174, 1991.
65. Goto, M., Imamura, T., and Hirose, T., Axial Dispersion in Liquid Magnetically Stabilized Fluidized Beds, *J. Chromatogr. A.* 690, 1-8, 1995.
66. Fee, C.J., Stability of the Liquid-Fluidized Magnetically Stabilized Fluidized Bed, *AIChE J.* 42, 1213-19, 1996
67. Cocker, T.M., Fee, C.J., and Evans, R.A., Preparation of Magnetically Susceptible Polyacrylamide/Magnetite Beads for Use in Magnetically Stabilized Fluidized Bed Chromatography, *Biotechnol. Bioeng.* 53, 79-87, 1997.
68. Ames, T.T. and Worden, R.M., Continuous Production of Daidzein and Genistein from Soybean in a Magnetofluidized Bed Bioreactor, *Biotechnol. Prog.* 13, 336-339, 1997.
69. Saxena, S.C., and Wu, W.Y., Hydrodynamic Characteristics of Magnetically Stabilized Fluidized Admixture Beds of Iron and Copper Particles, *Can. J. Chem. Eng.* 77, 312-318, 1999.
70. Zhang, Z., O'Sullivan, D.A., and Lyddiatt, D., Magnetically Stabilized Fluidized Bed Adsorption: Practical Benefit of Uncoupling Bed Expansion from Fluid Velocities in the Purification of a Recombinant Protein from *Escherichia coli*, *J. Chem. Technol. Biotechnol.* 74, 270-274, 1999.
71. Bohm, D., and Pittermann, B., Magnetically Stabilized Fluidized Beds in Biochemical Engineering - Investigations in Hydrodynamics, *Chem. Eng. Technol.* 23, 309-312, 2000.
72. Lin, Y.-C., and Leu, L.-P., Voidage Profiles in Magnetically Stabilized Fluidized Beds, *Powder Technol.* 120, 199-215, 2001.
73. Chen, C.-M., and Leu, L.-P., Hydrodynamics and Mass Transfer in Three-Phase Magnetic Fluidized Beds, *Powder Technol.* 117, 198-206, 2001.

74. Franzreb, M., Hausmann, R., Hoffmann, C., and Holl, W.H., Liquid-Phase Mass Transfer of Magnetic Ion Exchangers in Magnetically Influenced Fluidized Beds I. DC Fields, *React. Polym.* 46, 247-257, 2001.
75. Chen, C.-M., and Leu, L.P., Flow Regimes and Radial Gas Holdup Distribution in Three-Phase Magnetic Fluidized Beds, *Ind. Eng. Chem. Res.* 41, 1877-1884, 2002.
76. Fan, M., Chen, Q., Zhao, Y., Guan, Z.L.Y., and Li, B., Magnetically Stabilized Fluidized Beds for Fine Coal Separation, *Powder Technol.* 123, 208-211, 2002.
77. Jovanovic, G.N., Sajc, L.M., Jovanovic, Z.R., Novakovic, G.V., Kundacovic, B., Obradovic, B., and Vukovic, D.V., Flow Behavior of Fluidized Beds in a Magnetic Field, *J. Serb. Chem. Soc.* 57, 345-352, 1992.
78. Jovanovic, G.N, Jovanovic, Z., A Novel Approach in Controlling Performance of Fluidized Bed: Fluidization Regimes in Magnetically controlled Fluidized Beds, paper No 28i, AIChE Annual Meeting, November 7-12, St. Louis, 1993.
79. Kool-Lee, W., *The Effect of Interparticle Forces on Fluidization Regimes; a Study of Magnetized Fluidized Beds*, M.S. Thesis, Oregon State University, Corvallis, Oregon, 1994.
80. Honerez, L., *Fluid Dynamic Characteristics of a Magnetically Stabilized Liquid-Solid Fluidized Bed*; M.S. Thesis, Oregon State University, Corvallis, Oregon, 1994.
81. Al-Mulhim, M., and Jovanovic, G. N., Fluidization Regimes, Structure and Porosity of Magnetically Stabilized Liquid-Solid Fluidized Bed, paper No: 157d, AIChE Annual Meeting, November 14-18, 1994, San Francisco, 1994.
82. Honorez, L., and Jovanovic, G. N., Liquid-Solid Mass Transfer in Magnetically Stabilized Fluidized Beds, paper No: 127g, AIChE Annual Meeting, November 12-17, 1995, Miami Beach 1995.
83. Al-Mulhim, M., *Enhancement of Mass Transfer Coefficient in a Magnetically Stabilized Liquid-Solid Fluidized Bed*; M.S. Thesis, Oregon State University, Corvallis, Oregon, 1995.
84. Rhee, B., *Mass Transfer Coefficient in a Magnetically Stabilized Liquid-Solid, and Gas-Liquid-Solid Fluidized Bed*, M.S. Thesis, Oregon State University, Corvallis, Oregon, 1996.
85. Jovanovic, G.N., Sajc, L., Jovanovic, Z.R., Bugarski, B., and Novakovic, G.V., The interfacial Stability of Magnetically Stabilized Fluidized Beds, *J. Serb. Chem. Soc.* 61, 319-329, 1996.

86. Sajc L., Jovanovic, G., Jovanovic, Z.R., Bugarski B., Novakovic, G.V., The interfacial Stability of Magnetically Stabilized Fluidized Beds, *J. Serb. Chem. Soc.* 61, 319-329, 1996.
87. Clement, L., Pinto, J., and Jovanovic, G.N., Sludge Remediation in Magnetically Stabilized Fluidized Beds, presented at Environmental Catalysis-1997, Houston, Texas, March 9-13, 1997.
88. Clement, L., and Jovanovic, G.N., Magnetically Stabilized Fluidized Bed-New Technology for Remediation of Contaminated Soils, Sludges and Liquid Wastes, presented at 97 Waste Management Symposium, Tucson, Arizona, March 2-5, 1997.
89. Graham, L.J., *Dechlorination of p-Chlorophenol on Bimetallic Pd/Fe Catalyst in a Magnetically Stabilized Fluidized Bed: Experiment and Theory*, Doctoral Dissertation, Oregon State University, Corvallis, Oregon, 1998.
90. Villers, F., *Bed Porosity in a Magnetically Stabilized Liquid-Solid Fluidized Bed,* M.S. Thesis, Oregon State University, Corvallis, Oregon, 1998.
91. Baker, E.G., Mudge, L.K., and Brown, M.D., Steam Gasification of Biomass with Nickel Secondary Catalysts, *Ind. Eng. Chem. Res.* 26, 1335-1339, 1987.
92. Rei, M.-H., Su,T.-B., and Lin, F.-S., Catalytic Gasification of Rice Hull. 3. Measurement of Reaction Efficiency in the Steam Reforming of Carbonaceous Material, *Ind. Eng. Chem. Res.* 26, 383-386, 1987.
93. Wang, D., Czernik, S., Montane, D., Mann, M., and Chornet, E., Biomass to Hydrogen via Fast Pyrolysis and Catalytic Steam Reforming of the Pyrolysis Oil or Its Fractions. *Ind. Eng. Chem. Res.* 36, 1507-1518, 1997.
94. Garcia, X.A., Alarcon, N.A., and Gordon, A.L., Steam Gasification of Tars using a CaO Catalyst, *Fuel Process. Technol.* 58, 83-102, 1999.
95. Hayashi, H., Murata, S., Tago, T., Kishida, M., and Wakabayashi, K., Methane-Steam Reforming over Ni/Al_2O_3 Catalyst Prepared using W/O Microemulsion, *Chem. Lett.* 34-35, 2001.
96. Fu, W.B., Qin, C., and Li, C.L., Experimental Study on Ignition of Pre-Mixed Gases with Steam Under Catalytic Reforming Reaction, *Fuel Process. Technol.* 72, 131-143, 2001.
97. Galloway, T., Steam-Reforming of Wastes for Life Support in Space Systems, Final Report, Contract NAS2-13976, prepared for NASA-ARC, by Synthetica Technologies, Inc., 1994.

98. Delgado, J., Aznar, M.P., and Corella, J., Biomass Gasification with Steam in Fluidized Bed: Effectiveness of CaO, MgO, and CaO-MgO for Raw Gas Cleaning. *Ind. Eng. Chem. Res.* 36, 1535-1543, 1997.

99. Minkova, V., Marinov, S.P., Zanzi, R., Bjornbom, E., Budinova, T., Stefanova, M., and Lakov, L., Thermochemical Treatment of Biomass in a Flow of Steam or in a Mixture of Steam and Carbon Dioxide, *Fuel Process. Technol.* 62, 45-52, 2000.

100. Masuda, T., Kushino, T., Matsuda, T., Mukai, S.R., Hashimoto, K., and Yoshida, S.-I., Chemical Recycling of Mixture of Waste Plastics Using a New Reactor System with Stirred Heat Medium Particles in Steam Atmosphere, *Chem. Eng. J.* 82, 173-181, 2001.

101. Schuster, G., Loffler, G., Weigl, K., and Hofbauer, H., Biomass Steam Gasification - An Extensive Parametric Modeling Study, *Bioresource Technol.* 77, 71-79, 2001.

102. Hayashi, J.-I., Takahashi, H., Iwatsuki, M., Essaki, K., Tsutsumi, A., and Chiba, T., Rapid Conversion of Tar and Char from Pyrolysis of Brown Coal by Reactions with Steam in a Drop-Tube Reactor, *Fuel* 79, 439-447, 2000.

103. Ming, Q., Healey, T., Allen, L., and Irving, P., Steam Reforming of Hydrocarbon Fuels, *Catal. Today* 77, 51-64, 2002.

104. Fu, W.B., Qin, C., and Li, C.L., Experimental Study on Ignition of Pre-Mixed Gases with Steam under Catalytic Reforming Reaction, *Fuel Process. Technol.* 72, 131-143, 2001.

105. Borowiecki, T., Giecko, G., and Panczyk, M., Effects of Small MoO_3 Additions on the Properties of Nickel Catalysts for the Steam Reforming of Hydrocarbons II, Ni-Mo/Al2O3 Catalysts in Reforming, Hydrogenolysis and Cracking of n-Butane, *Appl. Catal. A* 230, 85-97, 2002.

106. Fierro, V., Akdim, O., and Mirodatos, C., On-board Hydrogen Production in a Hybrid Electric Vehicle by Bio-ethanol Oxidative Steam Reforming over Ni and Noble Metal Based Catalysts, *Green Chem.* 5, 20-24, 2003.

107. Fatsikostas, A.N., Kondarides, D.I., and Verykios, X.E., Steam Reforming of Biomass-derrived Ethanol for the Production of Hydrogen for Fuel Cell Applications, *Chem. Commun.* 851-852, 2001.

108. Choudhary, V.R., Banerjee, S., and Rajput, A.M., Hydrogen from Step-wise Steam Reforming of Methane over Ni/ZrO_2: Factors Affecting Catalytic Methane Decomposition and Gasification by Steam of Carbon Formed on the Catalyst, *Appl. Catal. A* 234, 259-270, 2002.

109. Shishido, T., Wang, P., Kosaka, T., and Takehira, K., Steam Reforming of CH_4 over Ni/Mg-Al Catalyst Prepared by *spc*-Method from Hydrotalcite, *Chem. Lett.* 752-753, 2002.

110. Choudary, V.R., Mamman, A.S., and Uphade, B.S., Steam and Oxysteam Reforming of Methane to Syngas over $Co_xNi_{1-x}O$ Supported on MgO Precoated SA-5202, *AIChE J.* 47, 1632-1638, 2001.